Formation and Processing of Rheocast Microstructures

by

Raul A. Martinez-Ayers

S.M., Massachusetts Institute of Technology (2001)
B.S., The University of Arizona (1999)

Submitted to the Department of Materials Science and Engineering
in partial fulfillment of the requirements for the degree of

Doctor of Philosophy

at the

MASSACHUSETTS INSTITUTE OF TECHNOLOGY

September 2004

Signature of Author .....
Department of Materials Science and Engineering
18 June 2004

Certified by .....
Merton C. Flemings
Toyota Professor Emeritus of Materials Processing
Thesis Supervisor

Accepted by .....
Carl V. Thompson II
Stavros Salapatas Professor of Materials Science and Engineering
Chair, Department Committee on Graduate Students

Formation and Processing of Rheocast Microstructures

by

Raul A. Martinez-Ayers

Submitted to the Department of Materials Science and Engineering
on 18 June 2004, in partial fulfillment of the
requirements for the degree of
Doctor of Philosophy

Abstract

The importance of semi-solid metal processing derives primarily from its ability to form high integrity parts from lightweight alloys. Since the discovery of the semi-solid metal microstructure, most part production was by reheating of billets which possessed a suitable microstructure ("thixocasting"). However, it is now apparent that there are significant advantages of forming semi-solid slurry directly from liquid alloy ("rheocasting") and efficient rheocasting processes have been engineered.

In this work, experimental and analytical approaches were taken to study how non-dendritic microstructures form and evolve in Al-4.5wt%Cu alloy during the earliest stages of solidification. Experimental results showed that particles in quenched rheocast alloy were already spheroidal, and free of entrapped eutectic, after 5 seconds of solidification time. Spheroidal particles were also formed by reheating equiaxed dendrites of approximately 10 μm radius above the eutectic temperature for 5 seconds, but these spheroids contained entrapped eutectic.

In both rheocasting and reheating experiments, the average particle radius was found to increase with solidification time at a rate that closely follows the classical dendrite arm ripening curve. Particle growth models developed were compared with the average particle radius measurements, and particle solute content measurements.

The maximum cooling rate to maintain spheroidal interface stability at various solid fractions was studied experimentally. A modified stability model which considered particle interaction through solute field overlap was developed and found to be in good agreement with experimental data. A simple method for the foundry to determine the maximum cooling rate for a given slurry was proposed.

The fluidity of rheocast A357 alloy slurries was contrasted with the fluidity of superheated liquid. Rheocast slurries with 37% solid particles,were found to flow about half as far as fully liquid alloy superheated $20°C$ above the liquidus.

Thesis Supervisor: Merton C. Flemings
Title: Toyota Professor Emeritus of Materials Processing

Contents

List of Figures

Acknowledgements

Back in Bisbee, Arizona, my high school math teacher, "Doc", made us memorize a quote from Ralph Waldo Emerson: "That which we persist in doing becomes easier for us to do; not that the nature of the thing itself is changed, but that our power to do is increased." In the process of completing this thesis, it became clear to me why Dr. Drake's message is so true and important.

I am incredibly grateful to Professor Merton Flemings for being such a steady hand and sage advisor since I arrived at MIT. He has been genuinely devoted to passing on his unparalleled understanding of solidification, and also to guiding me in the process of learning how to think as an engineer. I will always admire his clarity of thought tremendously. I am also very grateful to Professor Alain Karma who has taught me a great deal and helped develop this thesis work. I would like to thank the members of my thesis committee, Professor Adam Powell IV and Professor Klaus Jensen, for their support and interest in my research.

Throughout my life, my parents have been an endless source of inspiration and encouragement. Although we've been many miles apart, my parents and sisters have taken every step of this journey at MIT with me. They have celebrated the good times and carried me through the rough ones. My accomplishment in finishing this work is theirs as well. I love you all very much. Gracias abuelitos. Los quiero mucho.

My life over the last five years has been full of happy moments thanks to Melissa Light. Her endless patience, support, and giving is special far beyond what words can describe. Melissa, I could not have completed this thesis without you, and now dedicate it to you.

My fellow labmate, Dr. Jessada Wannasin, has been a great friend throughout the years. We have worked hard side by side. I have no doubt that Jess will become a great professor in Thailand. Jess, I am very grateful for all the ways you've helped me.

Many thanks to the other members of the Solidification Research Group: to Professor Theo Kattamis for his support and teaching of coarsening; to Professor Hal Brody whose interest, patience, and teaching helped this work evolve from its early stages; and to Professor Doug Matson, Dr. Jim Yurko, Joan Yurko, Hoe-Phong Tham, and Lori Kensel for their friendship and support.

I would like to thank Mr. Fred Cote at the Edgerton Student Machine Shop for all the

instruction and support to build the equipment I used in my research. The experiments I ran were possible because of the things Fred taught me to make. Thank you, Fred.

There are many, many people whose friendship helped me finish my thesis. Polo, thank you for always being there and for the book in kindergarten. Mr. Sullivan, thank you for giving me the confidence to write. The memory of John Appelt has been an inspiration. Professor David Poirier has been a true friend and mentor over the years. I'd like to thank some special friends here at MIT for all the good times: Jeff, Bruce, Douglas, Ashley, and Dave.

I am very grateful to the Department of Materials Science and Engineering at MIT for giving me the opportunity to learn from so many intelligent, interesting people. I would also like to thank the National Science Foundation and the Gates Millennium Scholarship Program for the financial support they have provided during the course of my studies.

Chapter 1

Introduction

1.1 History of Semi-Solid Metal Processing

The semi-solid metal structure was invented in the early 1970's by Spencer and Flemings at MIT.[1] They found that by mechanically agitating a solidifying alloy in the solid-liquid temperature range, the solid phase would not be in the form of dendrites, but instead spheroidal particles. The inventors discovered that the non-dendritic nature of the solid phase gave these metal "slurries" unique rheological properties. A metal slurry with up to 50% solid phase would flow homogeneously with an "effective viscosity" orders of magnitude greater than liquid alloy. The inventors realized that if the metal slurries were formed into parts, the higher viscosity would lead to less turbulent mold filling, thereby producing high quality parts by minimizing the entrapment of air and inclusions. Two semi-solid metal processing routes were quickly demonstrated to be industrially feasible: "rheocasting" and "thixocasting". Rheocasting refers to a process in which a slurry with non-dendritic structure is created from liquid alloy, and then the slurry is formed into a part. "Thixocasting" refers to a process in which a non-dendritic structure slurry is obtained by reheating a fully solidified billet back into the solid-liquid temperature range, then forming the slurry into a part. Both rheocasting and thixocasting are now referred to as "semi-solid metal" (SSM) processes.[2]

Over the last 30 years, the dominant SSM processing route employed by industry has been thixocasting.[3] Electromagnetically stirred billet was produced by continuous casters.[4] The billet possessed what might be termed a "degenerate" dendritic structure. The thixocaster

would buy this billet, reheat it into the solid-liquid temperature range, and form it into parts. Despite industry's initial impetus towards thixocasting, in the year 2000 thixocasting was estimated to represent only 1% of the 2.5 million tons of aluminum castings in North America, Europe, and Japan.[5]

The issues which have prevented wide-spread adoption of thixocasting are operating cost and process control. With thixocasting, inhomogeneity of billet structure and composition, and liquid run-off during reheating, can compromise part quality and productivity. The thixocaster must pay a premium for the billet used. This premium is paid not only for the metal sold to the customer, but also for the metal solidified in gates and runners, scrap which cannot be recycled on site for use with the SSM forming process. These cost challenges have almost extinguished the current use of thixocasting in industry.[6]

1.2 Rheocasting

The recent trend in semi-solid metal forming is to advance the rheocasting approach. Rheocasting has immediate advantages over thixocasting: 1) liquid alloy can be formed into a non-dendritic metal slurry at the part manufacturing site, and 2) scrap can be recycled on site.

Part quality remains as the biggest factor driving current industrial interest in rheocasting. However, there also exists a potential cost benefit of rheocasting over conventional liquid casting. A metal slurry cast into a die with 50% solid phase requires significantly less heat to flow into the die before the part can be removed. As a result the die operates at a lower temperature and die life increases. Because less heat needs to leave the part, the cycle time for casting a slurry can be significantly shorter than for casting liquid. These factors contribute to a potentially significant reduction in operating cost when compared to liquid casting, especially for casting parts with thick sections.[6]

The challenge for rheocasting has been the limited knowledge about how to efficiently process liquid alloy to create non-dendritic metal slurries. It is now known that by controlling the conditions present during the initial stages of solidification (the formation of only the first few percent of solid phase) non-dendritic structures can easily be created. Martinez and Flemings showed that by combining localized rapid cooling and vigorous agitation in a melt so that the

temperature drops from just above to just below the liquidus, a non-dendritic structure can achieved in a matter of seconds.[7] Figure 1-1 shows the process used, now called the SSR® process. A cold rotating copper rod is immersed into the melt held slightly above the liquidus temperature, stirring it vigorously and cooling it just below the liquidus. The rod remains in the melt just long enough for the first few percent of solid phase to form (typically several seconds) before it is removed. The rheocast structure can then be cooled to obtain the desired fraction solid.

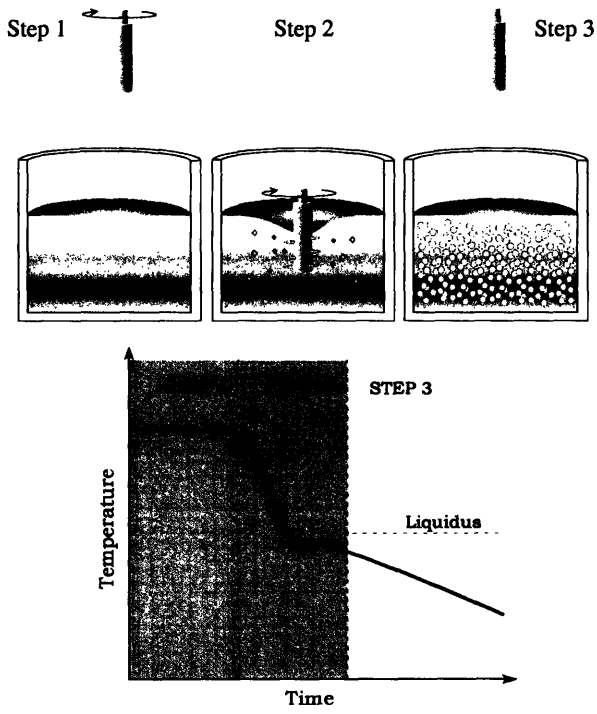

Figure 1-1: Schematic of the three basic steps in the SSR® process.

All successful rheocasting processes combine some amount of rapid cooling and agitation at the onset of solidification, just at or below the liquidus temperature.[7] It is here, and apparently only here, that the nucleation and dendrite fragmentation events which lead to a non-dendritic structure take place. For rheocasting to become a reliable, widely used metal forming technology, it is necessary to continue to improve the understanding of the initial stages of solidification. Furthermore, a better grasp of particle size evolution and particle interface stability will improve process control.

1.3 Goals and Organization of this Work

The primary goal of this work is develop an understanding of how particle morphology in rheocast alloy evolves during the earliest stages of solidification. The rate at which particles in rheocast alloy grow and the processing conditions needed to maintain spheroidal interface stability were investigated.

The available literature surrounding these three topics will be reviewed. Simple models of particle growth and stability in rheocast alloy will be presented. Results from various types of experiments will be compared to the models whenever possible. The significance of these analyses will be discussed and conclusions drawn.

Chapter 2

Literature Review

2.1 Semi-solid Metal Applications

Since the invention of the SSM processes, industry has grown increasingly aware of their potential. Today SSM research is conducted in academia and industry worldwide. There have been seven biennial international conferences on semi-solid processing.[8]–[14] The eighth will take place in Cyprus in September of 2004. Papers submitted to these conferences now include a large variety of research topics such as new ways to form non-dendritic material, rheology, mechanical properties, alloy design, heat treatment, process modeling, and forming trials.

The proliferation of SSM applications in industry is still in its early stages. Aluminum alloy automotive applications for have been the focus of industrial interest in SSM. Concern about fuel efficiency and the environment has resulted in a drive toward lighter vehicles. This in turn has lead to a continual increase in aluminum casting usage in vehicles and rekindled interest in processes like SSM which can yield high quality aluminum parts. Some of the automotive parts being considered for aluminum SSM are suspension components, air conditioning compressors, and master brake cylinders.[15],[16] Most recently Honda has turned to aluminum alloy SSM to manufacture cylinder blocks for the next line of turbo diesel engines in the Accord to be marketed in Europe.[17] Semi-solid magnesium alloy is also being considered for various automotive applications such as seat back frames and fuel rails.[18]

Aside from automotive applications, the advantages of SSM can be exploited for manufacturing hand tools, sporting equipment, and consumer electronics casings with SSM.[16],[18] In addi-

tion to light weight alloys, interest in using SSM for processing ferrous alloy is growing.[19],[20] Other novel SSM applications include using the high viscosity of semi-solid metal slurry for rapid prototyping and for brazing.[21]–[23]

2.2 Rheocasting Processes

Today there are several processes for creating non-dendritic structures from liquid alloy. The first approach used was mechanical stirring of metal in the solid-liquid temperature range. This was the original method employed by Spencer and Flemings during their discovery of the non-dendritic structure. Several patents have been granted for equipment designed to create metal slurry by mechanical stirring.[24]–[27] In the SCR process, liquid metal begins to freeze when it comes in contact with a cooling roller, which shears the alloy as it passes through a narrow gap.[25],[28] Other processes use equipment similar to a polymer injection molder, where solidifying metal is sheared between twin screws which are also used to inject the metal slurry into a die.[24] This approach has had some success for use with magnesium alloy.[18],[26] However, the lack of robust stirring materials able to withstand exposure to molten aluminum for long periods of time have limited the use of the mechanical stirring approach in industry. As new materials are engineered this limitation may disappear.

There are a number of novel approaches to making non-dendritic aluminum structures. One approach is mixing two alloy streams of specified composition and temperature to create a third alloy composition, at a temperature just below its liquidus, possessing a high density of crystal nuclei which can ripen into spheroids.[29] Another novel approach is the Osprey process, which mists liquid metal to create a metal slurry.[30] Thermal conditions cause smaller droplets in the mist to solidify and larger droplets to remain liquid. Both solid and liquid droplets are recaptured and combined to form a slurry. The solid phase will ripen into spheroidal particles.

More recent commercial rheocasting processes use a "low temperature pouring" technique. In the New Rheocasting process, liquid aluminum alloy, at a temperature just above its liquidus, is poured into a cooler steel cup.[31] As the metal is poured, solidification initiates when the flowing liquid contacts the cooler cup walls. The combination of solidification and pouring results in the formation of many solid particles. After pouring, heat extraction is controlled to

cool the volume of metal homogeneously. The SLC® process uses the same "low temperature pouring" approach. Highly grain refined liquid aluminum is poured into the shot sleeve of a vertical squeeze caster.[32] The shot sleeve acts as the cooling container. The idea of pouring slightly superheated alloy directly into the shot sleeve was patented much earlier by Hitachi.[33] Another simple rheocasting process employs pouring a slightly superheated metal on a "cooling slope". The metal begins to solidify as it flows down the slope and the slurry is collected at the bottom of the slope.[34]

Rheocasting by using a low temperature pouring technique has some disadvantages. The cooling device must extract enough heat to drop the bulk temperature of the entire volume of metal needed below the liquidus temperature during the relatively short pouring period. Therefore, it must be thermally conductive but able to withstand prolonged contact with liquid aluminum. Dendrites may stick to and grow on the cooling surfaces, making cleaning necessary for the next pour to be effective and consistent. These issues may hinder high speed production, and can create variability in slurry microstructure. A recently published study of material produced by industrial equipment using the low temperature pouring method showed that the shape factors of particles are significantly different from the shape factor for a perfect sphere.[35]

The SSR® process, shown previously in Figure 1-1, is able to efficiently rheocast alloy with spheroidal particles by immersing a cool rotating rod into a melt held above the liquidus. The immersion of the rotating rod simultaneously creates a region of high local cooling, provides vigorous convection, and drops the bulk melt temperature below the liquidus. Sizeable volumes of metal slurry have been created in tens of seconds.[36] Cleaning and cooling the rod after the short stirring period is straightforward. The SSR process can create slurry from liquid metal with large variability in superheat, making it a robust and efficient method to produce aluminum alloy slurries.

2.3 Formation of Particles During Rheocasting

2.3.1 Grain Density

In rheocast alloy, a significantly larger grain density than in conventional solidification is required for a non-dendritic structure to form. Flemings reviewed the current theory of the

evolution of a spheroidal microstructure, considering a "pre-dendrite" (a tiny equiaxed dendrite or dendrite fragment) floating in liquid phase just below the liquidus.[3] Consider the case where the initial grain density is large. For a given increase in solid fraction during cooling, each grain only needs to grow a small amount. With each grain remaining small, diffusion lengths for ripening are small and the evolution of the grain into a spheroid occurs rapidly. Now consider a much smaller number of initial grains. For a given increase in solid fraction during cooling, each grain will grow more significantly. If the grains grows to be too large, diffusion lengths are large. The grain will require more time to ripen into a "rosette" and later into a spheroid. If the dendrite has grown very large, it will ripen into a "deformed dendrite" which is unacceptable for semi-solid forming.

2.3.2 Convection

All rheocasting processes use convection to create a high density of grains (pouring, mechanical or electromagnetic stirring).[37] The grain refinement is attributed to the fact that the convection associated with the mold filling remains strong as solidification commences. Bower and Flemings performed experiments which showed that if convection is present at the onset of solidification, a structure with many smaller grains will form. Superheated liquid Al-4.5wt%Cu alloy was drawn into a thin-plate copper mold.[38] The dendritic structure on the surface of the cast plates were visible to the naked eye. If metal was drawn into the mold with a large amount of superheat, large dendrites were observed on the surface of the cast plates. If the metal was drawn with significantly less superheat, a far greater number of smaller dendrites were observed. Bower and Flemings believed that during an experiment, the tip of the metal in the channel would freeze first, stopping flow. For metal cast with a higher superheat, the metal behind the frozen flow tip would be quiescent when it began to solidify. Since convection was not present during solidification, the final grain size was large. For the case of metal cast with significantly less superheat, it was likely that the metal behind the flow tip already started to solidify before the flow tip froze, which resulted in a finer grain size throughout the casting.

Figure 2-1 shows results from an approximate reproduction of the Bower and Flemings experiments. Metal drawn into the channel with $105°C$ of superheat has much finer surface grains than the one drawn with $220°C$ of superheat. In both castings, the grain size at the top

of the sample, where it is assumed solidification began, is much smaller than at the bottom.

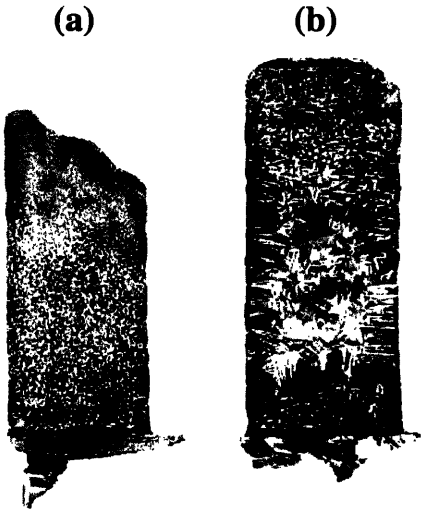

Figure 2-1: Visible dendrites of dramatically different sizes on the surface of thin-plate castings of Al-4.5wt%Cu. Metal was drawn into a copper mold with (a) $105°C$ of superheat, and (b) with $220°C$ of superheat. The samples were about 3 cm wide and 0.08 *cm* thick.

The "big bang" theory originally proposed by Jackson *et al.* is one way to explain the effect of convection on grain refinement.[39] These researchers used carbon tetrabromide with salol, a transparent analog casting system, and video equipment to show that when convection was present during solidification, many solid particles would suddenly be emitted from the mushy zone and would move into the bulk melt. The "big bang" theory explained this observation by postulating that convection caused thermal fluctuations which in turn lead to fluctuations in growth rate and remelting of dendrite arms. The detached arms were then thought to be transported by convective flows or buoyancy into the bulk melt, resulting in a structure with many smaller grains.

Cole and Bolling demonstrated the importance of convection in the transition from a columnar to an equiaxed growth mode.[40] Tin-lead alloy held in a cylindrical mold was solidified radially inwards. The position in which the growth mode changed from columnar to equiaxed growth was noted. Horizontal grids which limited natural convective flows but did not significantly change the flow of heat were then placed in an identical melt and the directional

solidification experiment was repeated. Results showed that the location of the transition from the columnar to equiaxed structure was significantly delayed with the grids in place. These findings indicated that convection played a significant role in generating and/or transporting solid particles from a columnar mushy zone into the bulk melt, and that a sufficiently high number of these particles in the bulk melt changed the solidification of the alloy from the columnar to the equiaxed growth mode.

2.4 Dendrite Fragmentation

It is generally accepted that the grain refinement which arrises from the strong presence of convection during solidification is due to the role of convection in dendrite fragmentation or "grain multiplication" mechanism. Using succinonitrile (another transparent analog casting system) and high-speed video equipment, Esaka *et al.* recorded images of particles being generated in the mushy zone of a stirred melt. The results showed that the number of particles generated, and the rate of generation, increased with increasing stirring intensity.[41] Martinez and Flemings have showed that if the combination of localized chill with vigorous convection is applied to a melt held just above its liquidus temperature, a non-dendritic structure will form in a matter of seconds.[7] They proposed that the dendrites that form in liquid adjacent to a chill may be so fine and/or fragile that when convection is present they are fragmented almost instantaneously after forming.

A variety of dendrite fragmentation theories exist. Vogel *et al.* and Doherty *et al.* suggested that liquid motion creates shear forces leading to bending of dendrite arms. It was hypothesized that the bending of the arms form high-angle grain boundaries at the roots of the arms, thereby increasing surface energy at the root. According to the theory, liquid phase could then wet the high-angle grain boundaries and detach the arms.[42],[43] Kattamis *et al.* developed a coarsening model in which dendrite arms would detach from the trunk at a rate which was strongly dependent on the dendrite arm spacing.[44] If each detached arm is swept by convection into the bulk melt and continues to grow, this coarsening mechanism is a potential form of grain multiplication.

Whether convection aids in the dendrite breakage or simply transports fragments into the

bulk liquid remains undetermined. Due to the very short times necessary to complete the dendrite fragmentation process(es), it has proven difficult to obtain definitive experimental data supporting any one fragmentation theory and eliminating others.

2.5 Structural Evolution in Rheocast Alloy

There is great practical importance in understanding the evolution of spheroids in a rheocast slurry. Particles must be sufficiently spheroidal for a slurry to flow homogeneously into a mold, and particle size can influence the effective viscosity and force required to induce flow.[35],[45]

Until recently, thixocasting has been the more industrially relevant SSM process. Therefore, most experimental studies have focused on the evolution of spheroids starting with billet containing large, degenerate dendrites.[46] Much less work was found regarding the evolution of small grains during short solidification times. However, it is clear from recent work that the most significant morphological changes occur during short times after the onset of solidification.[7]

The work of Boggelen *et al.* is further evidence that fine structures evolve rapidly in short times.[47] The work measuring the equiaxed dendritic grain size evolution of Al-Cu alloy during reheating above the eutectic temperature for various short times . The initial grain size was estimated to be approximately 50 μm, about half the size of typical grains in commercial grain-refined aluminum alloy. Grain size was reported to decrease for reheating times less than 2 seconds, and then increase for longer reheating times. Ripening was found to cause significant microstructural changes in grain size during the first 60 seconds of reheating. At longer reheating times, the grains became more spheroidal and grew in size.

An empirical rule for the average particle size in rheocast alloy is that it will change as a function of solidification time at roughly the same rate as the secondary dendrite arm spacing in dendritic alloy. Taking particle size to be half of the grain size reported, the data of Boggelen *et al.* roughly follows this general rule.[47] The experimental investigation of Kattamis *et al.* showed that the spheroidal particle diameter in grain-refined Mg-5%Zn alloy changed with solidification time similar to the evolution of secondary dendrite arm spacing in Mg-5%Zn dendritic alloy.[48]

Other factors in the solidification of an alloy can influence the evolution of spheroidal particle size in non-dendritic alloy. Glicksman *et al.* showed that the interaction among a population of particles will increase the ripening rate and alter the particle size distribution.[49] Ichkikawa *et al.* studied the rate of particle growth in rheocast (mechanically sheared) Al-4wt%Cu, Al-10wt%Cu, and Al-4wt%Cu alloys cooled at various slow rates (less than $0.1°C/s$).[50] Particle size measurements showed that for a given solidification time, the average particle radius (half of the "particle size" reported) was slightly greater the secondary dendrite arm spacing in dendritic alloy, and increased at a slightly greater rate than the secondary dendrite arm spacing. It was speculated that the increased growth rate was due to convection aiding in the ripening process.

2.6 Particle Stability

In order to ensure proper part filling when casting a metal slurry into a mold, it is vital that the spheroidal structure of the solid particles is maintained as it passes through the gates and runners. However, because the gates and runners may be significantly cooler than the metal, the slurry may be cooled relatively quickly and the spheroidal particle interface may become unstable. If this occurs, flow properties can change and prevent proper mold filling. Understanding the conditions which maintain interface stability in rheocast alloy is critical to processing.

The basic theory of linear interface stability used to analyze alloy solidification and dendrite formation was developed by Mullins and Sekerka.[51],[52] Langer later followed the treatment for a three-dimensional spheroidal interface.[53] The treatment assumes that a solid particle is growing into an infinite liquid surrounding. In rheocasting, this assumption seems reasonably applicable to early stages of solidification, when particles are so small they interact only with their liquid surrounding. At larger solid fractions, or for slurries with a high particle density, interactions of particles with each other will promote solid-liquid interface stability.[54]

2.7 Fluidity of Rheocast Alloy

Most of the published studies on semi-solid metal flow properties have focused on the characterization of the thixotropic nature of metal slurries.[55],[56] Although this subject is of

fundamental importance to the SSM industry, perhaps a more basic test of the ability of a metal slurry to flow is to measure "fluidity length". In the foundry, fluidity is defined as the length that metal will flow down a channel before being stopped by solidification. Due to the direct link between slurry flow and microstructure, a fluidity test can be a simple, macroscopic assay of a rheocast alloy microstructure.

Ragone was the first to perform a quantitative analysis of the fluidity of pure liquid metals.[57] In the experiments, the flow of the metal entering the tube was turbulent, and driven by a constant pressure difference. Bernoulli's Equation was used to predict the length the metal would flow before solidifying. The analysis accounted for frictional losses but ignored surface tension and viscosity changes. Niesse extended the work of Ragone, using the same experimental apparatus. Niesse found that adding small amounts of alloying elements dropped the observed fluidity.[58] Flemings summarized the cause of this effect: alloying elements breakdown the smooth solid-liquid interface associated with pure metal solidification, resulting in dendrites reaching into the liquid, entangling, and ceasing the flow more quickly.[59] Kwon and Lee have recently shown that the fluidity of grain refined Al-Cu alloy is much greater than non-refined alloy.[60] The smaller grain size may delay dendrite entanglement and allow the alloy to flow further until a higher solid fraction is reached. Flemings *et al.* calculated the critical solid fraction in the flow tip which causes cessation of flow to be about 35%.[61] Whether this critical solid fraction also applies to the flow of non-dendritic Al-Cu alloy remains to be determined.

Only a handful of non-dendritic alloy fluidity investigations have been performed. Pai and Jones developed an empirical equation for the fluidity of their semi-solid slurries created by mechanical stirring.[62] Sumartha studied the fluidity of a rheocast A356 alloy by mechanical stirring an alloy to form between 15% and 30% solid content, and then drawing it into glass tubes.[63] Most recently, Nafisi *et al.* performed an experimental study the fluidity of mechanically stirred semi-solid A356 alloy with initial solid fractions between 10 and 50%.[64] At temperatures above the liquidus, alloy fluidity was found to decrease with decreasing temperature. Below the liquidus temperature, the fluidity of the non-dendritic slurry continued to decrease with decreasing temperature (increasing solid content), but the rate of decrease did not change significantly after crossing the liquidus temperature.

Chapter 3

Solidification Modeling

3.1 Particle Growth

Three different models were developed to simulate growth of spheroidal particles in Al-4.5wt%Cu alloy. The models were: (1) Equilibrium, (2) Scheil, and (3) Liquid Diffusion Controlled (LDC). The three models are shown schematically in Figures 3-1 through 3-3 and described below.

In all three models, the liquidus and solidus curves in the Al-Cu phase diagram were assumed linear, and equilibrium was assumed at the solid-liquid interface. The models were used to simulate particle growth during "slow cooling" ($0.28°C/s$), "fast cooling" ($375°C/s$), and "slow followed by fast cooling" ($0.28°C/s$ for growth up 20 μm, then $375°C/s$). In all cases, it was assumed that particles could grow to a maximum radius, R_T, of 50 μm before completely impinging on their neighbors. Coarsening was not considered in any of the models, and will be discussed later.

3.1.1 Equilibrium Model

In the equilibrium solidification model, the concentrations of the liquid and solid phases change during cooling according to the liquidus and solidus curves in an alloy phase diagram, with complete diffusion in both phases. Figure 3-1 illustrates this schematically.

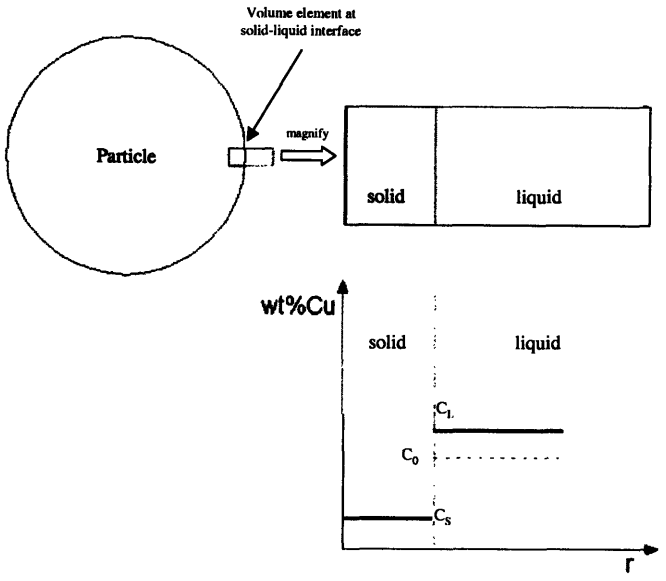

Figure 3-1: Schematic of a solidifying particle in rheocast alloy according to the equilibrium solidification model.

As a result of the assumption that the liquidus and solidus curves for the Al-4.5wt%Cu alloy are linear, the equilibrium liquid and solid concentrations can be described as a function of temperature by the equations:

$$C_L = C_0 - \frac{(T_L - T)}{m_L} \tag{3.1}$$

$$C_S = kC_0 - \frac{(T_L - T)}{m_S} \tag{3.2}$$

where C_L is the equilibrium liquid concentration at temperature T, C_S is the equilibrium solid concentration at temperature T, T_L is the liquidus temperature of the alloy, m_L is the slope of the liquidus line, m_S is the slope of the solidus line, k is the partition coefficient for the alloy, and C_0 is the bulk solute concentration in the alloy.

The temperature of the rheocast Al-4.5wt%Cu alloy being cooled at a rate $\left[\frac{dT}{dt}\right]$ is described by the expression

$$T = T_L + \left[\frac{dT}{dt}\right] t \tag{3.3}$$

For equilibrium solidification, the solid fraction, f_s, at any temperature in the solid-liquid temperature range is given by the lever rule:

$$f_s = \frac{C_L - C_0}{C_L - C_S} \tag{3.4}$$

Substituting Equations 3.1-3.3 into 3.4 gives the equilibrium relationship between solid fraction and temperature.

The solid fraction in a rheocast alloy containing perfectly spherical solid particles of radius R is also approximated by

$$f_s = \left(\frac{R}{R_T}\right)^3 \tag{3.5}$$

where R_T is the radius of a sphere that occupies the same volume as a fully solidified grain (particle) completely impinging on its neighbors. It is approximated by the final grain radius. Using Equations 3.1-3.5, the particle radius and composition were related to temperature and time.

3.1.2 Scheil Model

The Scheil analysis is a mass balance of the amount of solute rejected by a differential amount of solid formed with the resulting solute concentration increase in the surrounding liquid. The Scheil model assumes complete diffusion in the liquid and no diffusion in the solid phase. This mass balance is:

$$(C_L - C_S^*)df_s = (1 - f_s)dC_L \tag{3.6}$$

where C_L is the solute concentration in the bulk liquid, C_S^* the solute concentration of the solid at the solid-liquid interface, df_s is the small fraction of solid formed, and dC_L is the corresponding rise in the liquid composition due to the rejected solute during solidification. Figure 3-2 illustrates Scheil solidification of a spherical particle. The liquid composition is homogeneous, and diffusion of solute in the solid is assumed negligible.

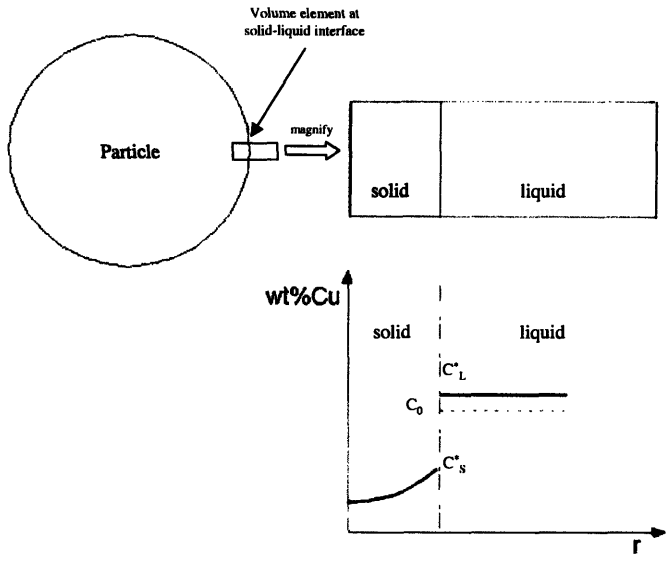

Figure 3-2: Schematic of a solidifying particle in rheocast alloy according to the Scheil solidification model.

In the Scheil model, the liquid and solid compositions are related by

$$C_S^* = kC_L \tag{3.7}$$

where k is the alloy partition coefficient, constant when the liquidus and solidus are assumed linear. Integrating Equation 3-2 with the initial condition $C_L = C_0$ when $f_s = 0$ yields

$$f_s = 1 - \left(\frac{C_L}{C_0}\right)^{-\frac{1}{(1-k)}} \tag{3.8}$$

and since the liquidus is linear

$$f_s = 1 - \left(\frac{T_P - T}{T_P - T_L}\right)^{-\frac{1}{(1-k)}} \tag{3.9}$$

where T_P is the melting point of pure aluminum, and T_L is the liquidus temperature of the alloy.

For rheocast alloy consisting of perfectly spherical particles of radius R, the solid fraction was again approximated by Equation 3.6. The temperature of an alloy being cooled down from

the liquidus temperature at a rate $\left[\frac{dT}{dt}\right]$ is again described by Equation 3.3

Using Equations 3.3, 3.5, and 3.9, the Scheil related particle radius, composition, temperature and time for rheocast Al-4.5wt%Cu alloy solidifying under various cooling conditions.

3.1.3 Liquid-Diffusion-Controlled (LDC) Model

In the LDC model, no solute diffusion in the solid phase is allowed and diffusion in the liquid phase is not complete, as shown in Figure 3-3. The solute rejected during solidification causes the formation of a solute gradient in the liquid near the solid-liquid interface.

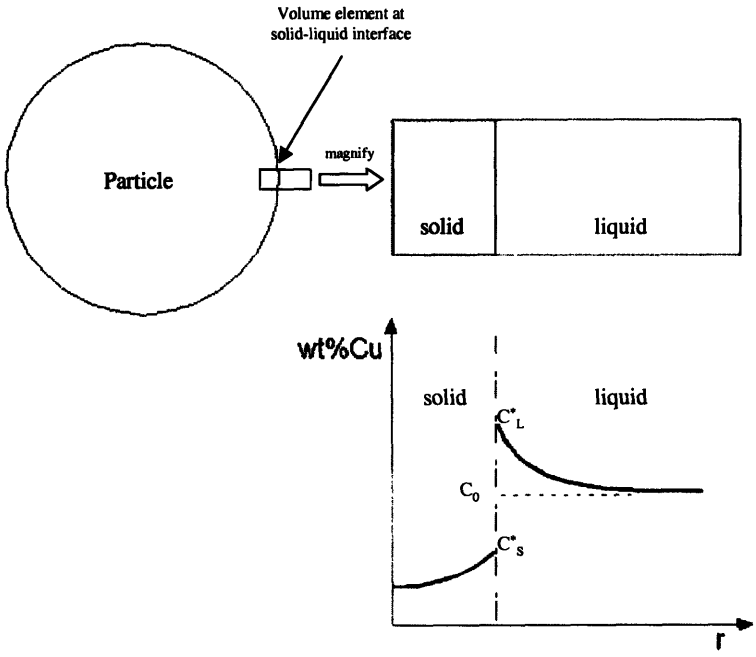

Figure 3-3: Schematic of a solidifying particle in rheocast alloy according to the liquid-diffusion-controlled (LDC) solidification model.

Professor Alain Karma (Physics Department, Northeastern University) developed a spherical particle growth model for a particle in Al-4.5wt%Cu alloy, assuming liquid diffusion as the limiting phenomena for solidification.[65] The LDC model simulates solidification within a spherical volume of radius R_T. Each simulation begins with a small "seed" particle (typically 1 μm radius) at the center of the spherical volume. The overall solute in the solid and liquid

phases contained within R_T is conserved. A rise in liquid concentration above the bulk composition C_0 at radius R_T marks the time when the solute field surrounding the particle begins to interact with neighboring particles.

The LDC model uses the following set of equations to describe the growth of a solidifying spherical particle:

$$C_0(1-k)\frac{dR}{dt} = -D_L\left(\frac{dC_L}{dr}\right)_{r=R} \tag{3.10}$$

$$\frac{dC_L}{dt} = D_L\left(\frac{1}{r}\frac{\partial C_L}{\partial r} + \frac{\partial^2 C_L}{\partial r^2}\right) \tag{3.11}$$

$$C_L^* - C_0 = -\frac{(T_L - T)}{m_L} + \frac{2\Gamma}{m_L}\frac{1}{R} \tag{3.12}$$

$$C_S^* = kC_L^* \tag{3.13}$$

where r refers to the radial direction, R is the particle radius, C_L^* is the liquid composition at the solid-liquid interface, and Γ is the Gibbs-Thompson coefficient. Equations 3.10-3.13 are solved numerically. The solution obtained from the LDC model gives the particle radius and growth velocity as a function of time, and also describes the interface solute concentration and the spatial variation of the liquid concentration over time.

3.1.4 Model Results

Case 1: Slow cooling (0.28°C/s)

Figure 3-4 shows the solid fraction as a function of temperature for the three models when cooling slowly down from the liquidus temperature at $0.28°C/s$. At any given temperature the equilibrium model gives the maximum solid fraction. The Scheil and LDC models produce equivalent curves.

Figure 3-5 shows the solute content in the liquid predicted by the LDC model as a function of radial distance at various times. For the case of slow cooling, when the particle has grown to a radius of only 10 μm the maximum difference in liquid composition is $\backsim 0.15$ $wt\%Cu$. At

larger particle sizes, the solute content at radius R_T will rise above the bulk alloy composition, marking the onset of solute field overlap. When the particle has grown to a size of 20 μm, the increasing amount of solute field overlap results in a maximum difference in liquid composition of $\backsim$ 0.05 $wt\%Cu$. Such small differences in solute concentration within the liquid makes the LDC model essentially identical to the Scheil model for the case of slow cooling.

Figure 3-6 illustrates the predicted solute within the particles as a function of particle radius. For the equilibrium model, the entire particle composition is uniform for each time shown. No diffusion is assumed in the Scheil and LDC models, and the curves for the two models are essentially identical.

Figure 3-7 plots the predicted particle size as a function of time. The equilibrium and Scheil model curves are very similar. The LDC model predicts the particle will grow to a slightly larger size in the first second of solidification, and then grow at a slightly slower rate than predicted by the other models.

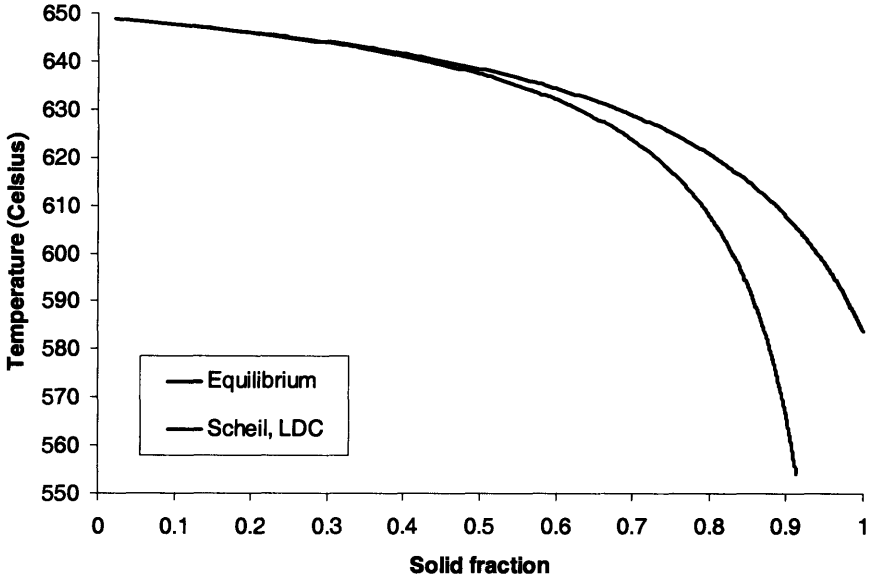

Figure 3-4: Predicted relationship between temperature and solid fraction according to the three particle growth models for the case of slow cooling down from the liquidus temperature at a rate of $0.28°C/s$ ($R_T = 50\mu m$).

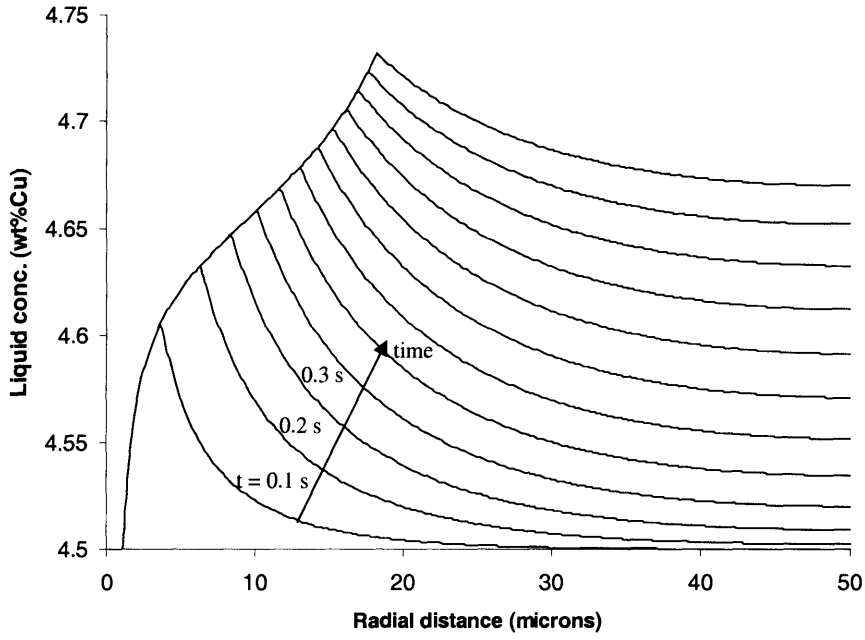

Figure 3-5: LDC model of liquid composition as a function of radial distance for the case of slow cooling down from the liquidus temperature at a rate of $0.28°C/s$ ($R_T = 50\mu m$).

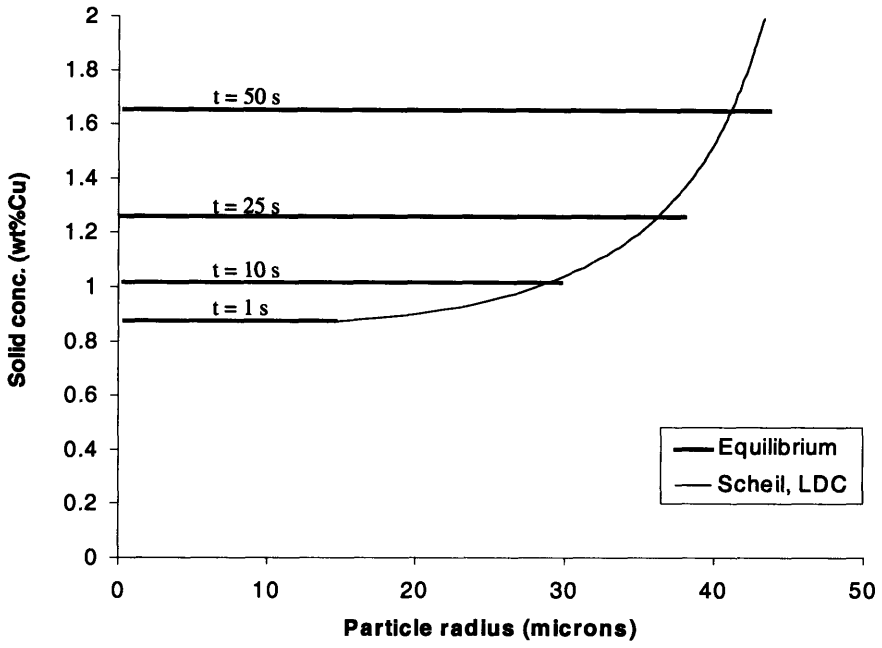

Figure 3-6: Solid particle composition as a function of particle radius according to the three models for the case of slow cooling down from the liquidus temperature at a rate of $0.28°C/s$ ($R_T = 50\mu m$).

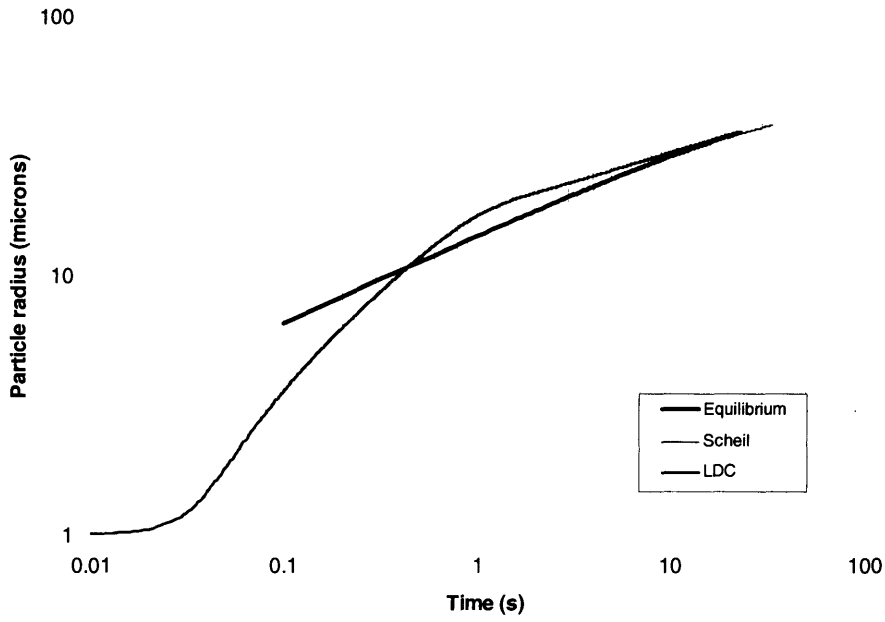

Figure 3-7: Predicted relationship between particle radius and time according to the three particle growth models for the case of slow cooling down from the liquidus temperature at a rate of $0.28°C/s$ ($R_T = 50\mu m$).

Case 2: Fast cooling (375°C/s)

Figure 3-8 plots solid fraction as a function of temperature according to each model for the case of fast cooling at $375°C/s$. The relationship for the equilibrium and Scheil solidification models is identical to that for slow cooling (Figure 3-4).

The LDC model produces a different relationship between temperature and solid fraction for the case of fast cooling. The shape of LDC temperature-solid fraction curve is a result of the build up of solute at the solid-liquid interface during rapid cooling. In the initial stages of solidification, some of the heat extracted, instead of resulting in removal of heat of fusion, results in supercooling of the liquid away from the solid-liquid interface. As the amount of solute field overlap increases during later stages of solidification, the liquid composition becomes more homogeneous. Hence, the liquid supercooling decreases and the temperature-solid fraction relationship approaches that described by the Scheil model.

Figure 3-9 shows the solute content in the liquid predicted by the LDC model as a function of radial distance and time. After only 0.1 second significant solute field overlap has occurred and the particle has grown to a radius of more than 47 μm. Equation 3.5 relates the 47 μm particle size to a solid fraction of 0.83 (using an R_T value of 50 μm). Due to the amount of solute field overlap, the LDC model predicts growth from this solid fraction onwards to be similar to the Scheil model, which is apparent in Figure 3-8.

Figure 3-10 plots the predicted solute content in the particle as a function of radial distance according to each model. The relationship between composition and particle size is identical to that of slow cooling for the equilibrium and Scheil growth models (Figure 3-6). In the LDC model the solid composition rises steeply as a result of the rejected solute buildup at the solid-liquid interface.

Figure 3-11 shows predicted particle size for all three models as a function of time for the case of rapid cooling.

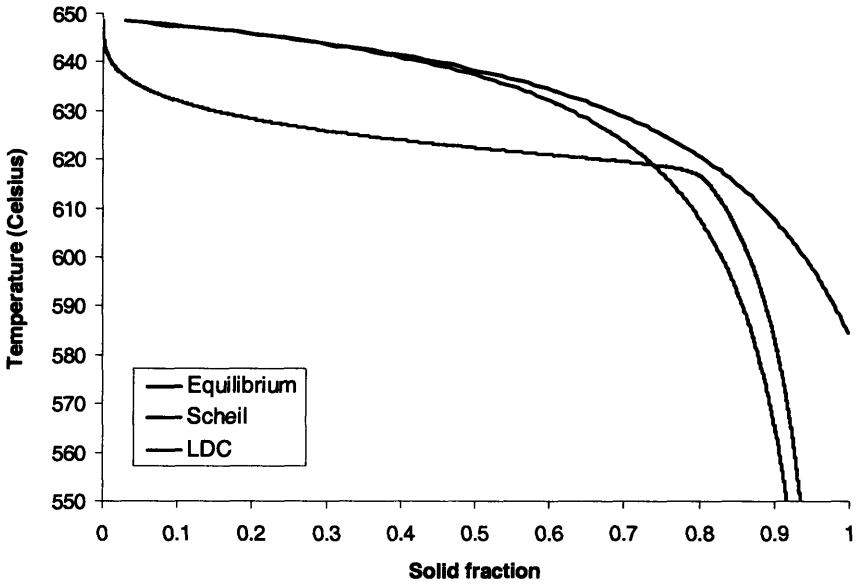

Figure 3-8: Predicted relationship between temperature and solid fraction according to the three particle growth models for the case of fast cooling down from the liquidus temperature at a rate of $375°C/s$ ($R_T = 50\mu m$).

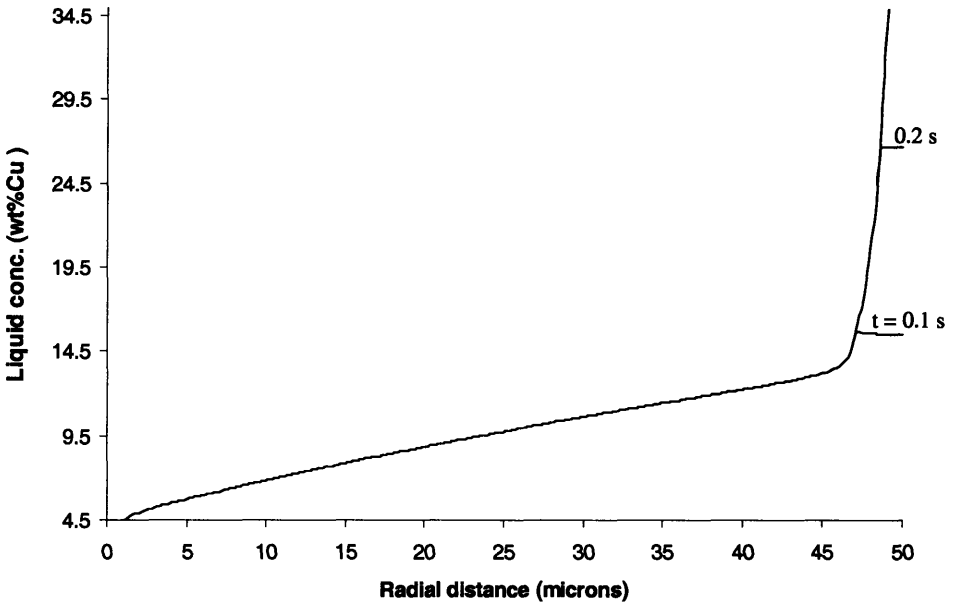

Figure 3-9: LDC model of liquid composition as a function of radial distance for the case of fast cooling down from the liquidus temperature at a rate of $375°C/s$ ($R_T = 50\mu m$).

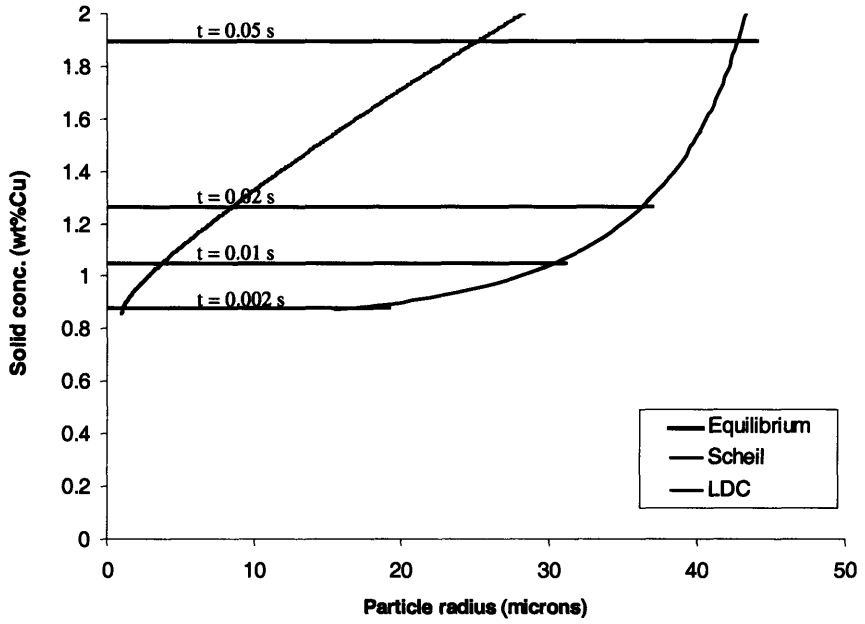

Figure 3-10: Solid particle composition as a function of radial distance according to the three models for the case of fast cooling down from the liquidus temperature at a rate of $375°C/s$ ($R_T = 50\mu m$).

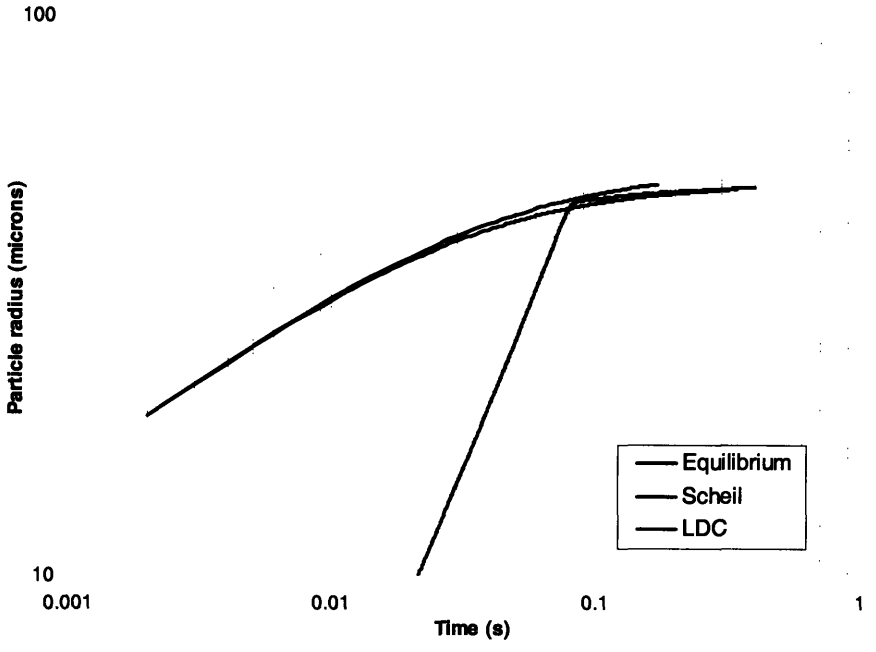

Figure 3-11: Predicted relationship between particle radius and time according to the three particle growth models for the case of fast cooling down from the liquidus temperature at a rate of $375°C/s$ ($R_T = 50\mu m$).

Case 3: Slow cooling followed by fast cooling

In the "slow cooling followed by fast cooling" simulations, rheocast Al-4.5wt%Cu alloy is cooled slowly at a rate of $0.28°C/s$ and then quenched at $375°C/s$. The cooling rate is increased to $375°C/s$ when the particle radius is 20 μm. Figure 3-12 plots solid fraction as a function of temperature as predicted by the three models employed. The sudden increase in cooling rate does not affect the relationship between solid fraction and temperature in the equilibrium and Scheil solidification models, but is apparent in the LDC model curve, as may be seen by comparing Figures 3-12 and 3-4.

Figure 3-13 shows solute content predicted by the LDC model in the liquid as a function of radial distance at various times during the slow then fast cooling simulation. For growth up to 20 μm with the slow cooling rate of $0.28°C/s$, the solute content in the liquid is relatively uniform and little changed from the initial composition of 4.5 $wt\%Cu$. The uniformity of the solute concentration in the liquid phase predicted by the LDC model implies significant solute field interaction during slow cooling. However, when the cooling rate is increased to $375°C/s$, solute fields stop interacting, and do not interact again until the particle grows to about 40 μm in radius (marked by a rise in solute concentration at radius R_T).

Figure 3-14 plots the predicted solute content in the particle as a function of particle radius. The relationship between composition and particle size is unchanged from the previous two cases for the equilibrium and Scheil growth models. In the LDC model, the solid composition rises sharply when the cooling rate is increased.

Figure 3-15 illustrates the predicted particle size as a function of time. The slope of all three curves increase abruptly when the cooling rate is increased.

Figure 3-16 shows the predicted growth velocity as a function of particle radius for the LDC model. In the fast cooling stage, growth velocity first increases to almost 500 $\mu m/s$ and then decreases abruptly. The decrease, caused by the onset of solute field interaction, occurs when the particle is roughly 40 μm. Recall that this particle radius corresponds to the particle size in Figure 3-13 when solute field overlap during fast cooling (when the liquid concentration at radius R_T began to rise).

An empirical expression describing the LDC growth velocity for a particle undergoing a sudden increase in cooling rate was obtained by Professor Alain Karma.[65] The equation was

later derived by Karma, and the derivation is given in Appendix A.[66] The equation which described the growth velocity of a particle in a slurry subjected to a sudden cooling rate increase is

$$V = A\frac{\dot{T}}{m_L C_0(k-1)}\left[D_L(\Delta t_0)\right]^{1/2} \tag{3.14}$$

where A is a pre-factor, $\dot{T}$ is the quench rate, and Δt_0 is the duration of quench (the time beginning from the start of quench).

Figure 3-17 is a plot of growth velocity versus time and shows how Equation 3.14 tracks the LDC model closely starting from the time the cooling rate is increased to $375°C/s$ (the pre-factor A was set equal to 1.28). Equation 3.14 is valid up to the maximum growth velocity when solute fields begin to overlap and cannot be used after the maximum velocity is reached. Equation 3.14 will be used in a subsequent section that will couple the LDC particle growth model with interface stability theory.

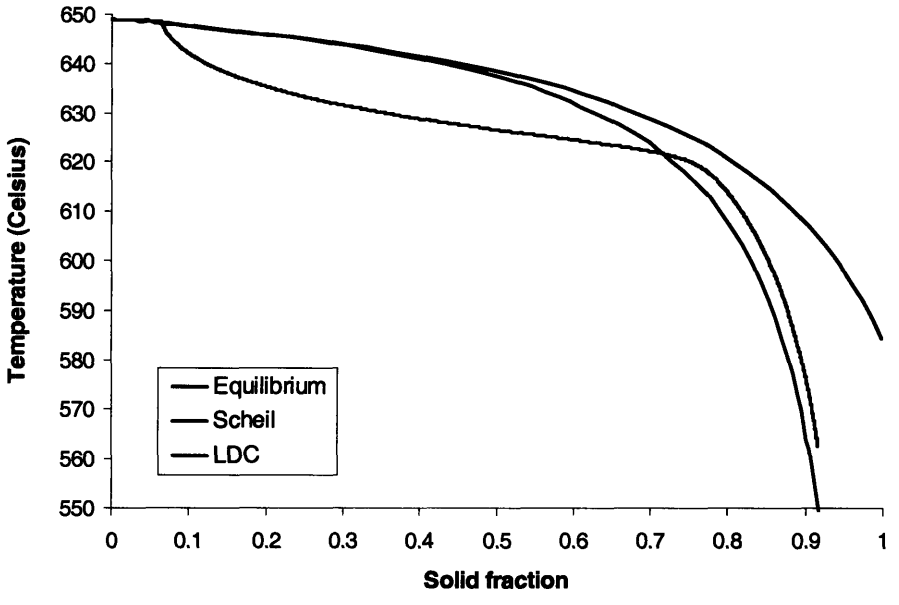

Figure 3-12: Predicted relationship between temperature and solid fraction according to the three particle growth models for the case of slow cooling for particle growth up to a $20\mu m$ radius, followed by fast cooling at $375°C/s$ ($R_T = 50\mu m$).

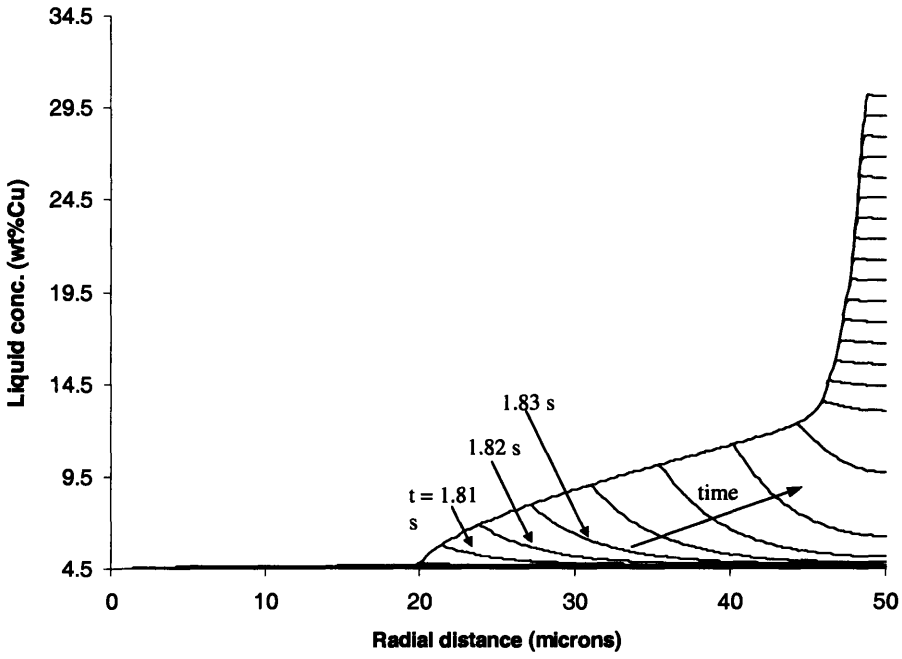

Figure 3-13: LDC model of liquid composition as a function of radial distance for the case of slow cooling during particle growth up to a $20\mu m$ radius, followed by fast cooling at $375°C/s$ ($R_T = 50\mu m$).

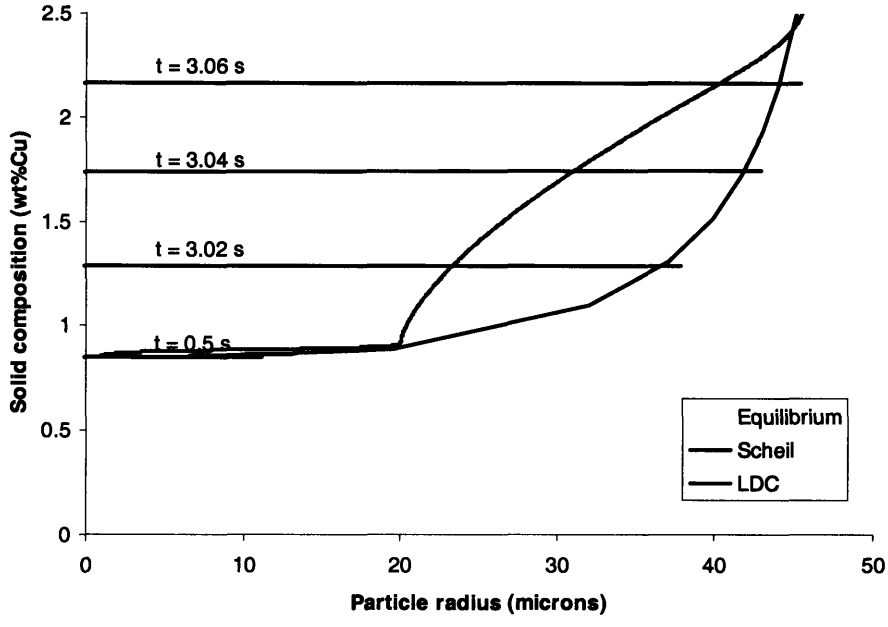

Figure 3-14: Solid particle composition as a function of radial distance according to the three models for the case of slow cooling during particle growth up to a $20\mu m$ radius, followed by fast cooling at $375°C/s$ ($R_T = 50\mu m$).

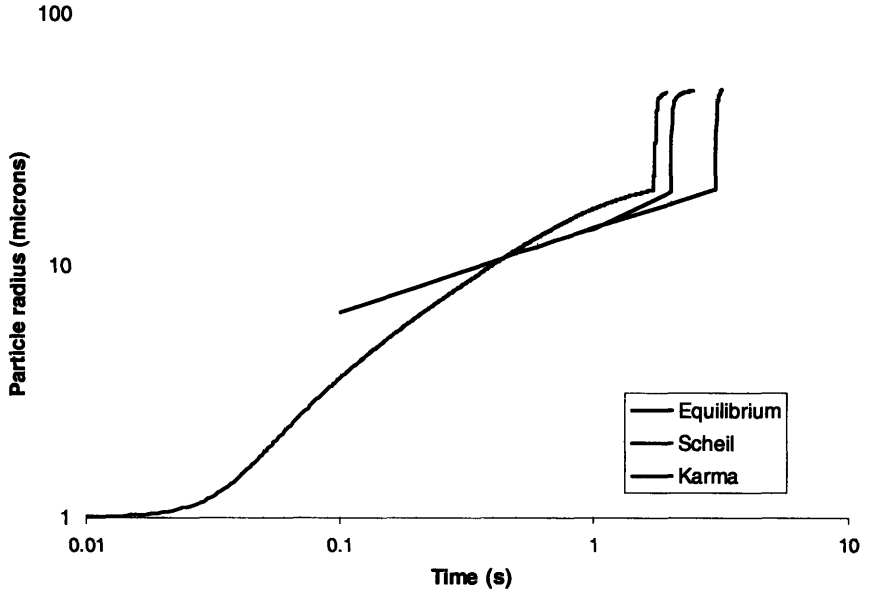

Figure 3-15: Predicted relationship between particle radius and time according to the three particle growth models for the case of slow cooling during particle growth up to a $20\mu m$ radius, followed by fast cooling at $375°C/s$ ($R_T = 50\mu m$).

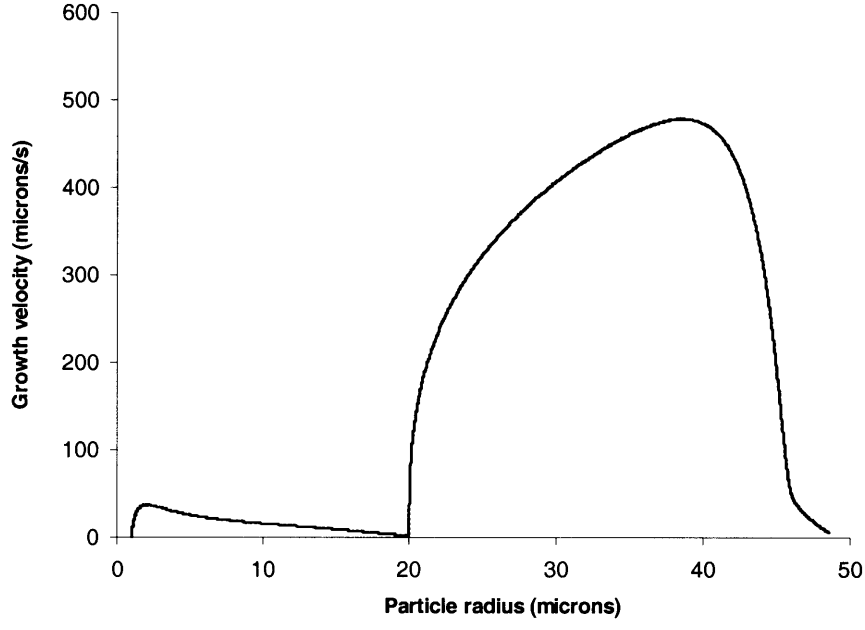

Figure 3-16: Predicted relationship between growth velocity and particle radius according to the LDC model for the case of slow cooling during particle growth up to a $20\mu m$ radius, followed by fast cooling at $375°C/s$ ($R_T = 50\mu m$).

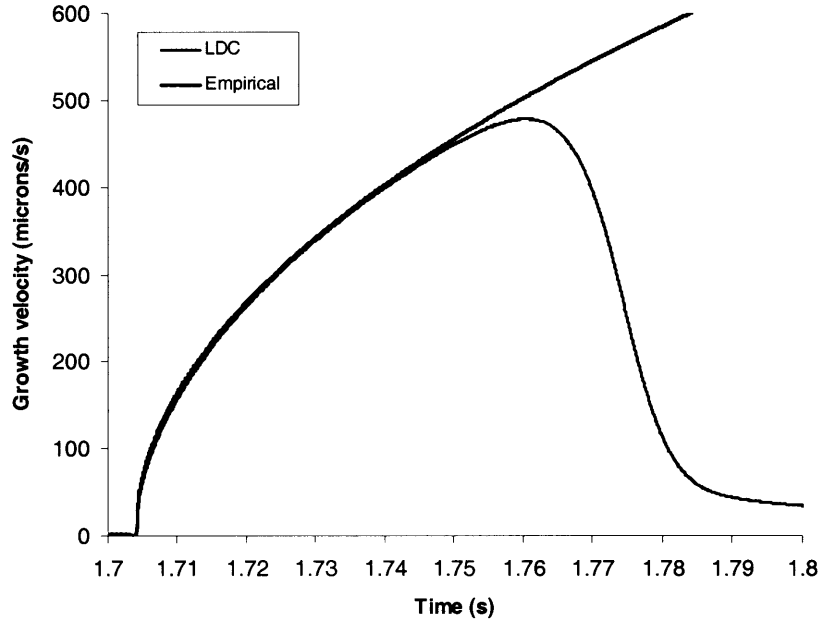

Figure 3-17: The LDC model curve for growth velocity as a function of and time for the case of slow cooling during particle growth up to a $20\mu m$ radius, followed by fast cooling at $375°C/s$ ($R_T = 50\mu m$). The curve generated with the expression given in Equation 3.14 is shown to be in good agreement with the LDC model curve over the time range from when the cooling rate was increased to $375°C/s$ to when the growth velocity reached its peak value.

3.2 Interface Stability

Each of the particle growth models presented in the previous chapter assumed spherical particle growth. The models did not consider under what conditions the interface of the spherical particle would become unstable, which would lead to the formation of cells or dendrites. The ability to maintain stable particle growth prior to forming a slurry into a part is required for semi-solid processing since the ideal spheroidal morphology of the solid phase provides optimal flow properties in the solid-liquid temperature range. This section presents analyses of the growth conditions leading to unstable particle growth. The basis of the interface stability theory employed is the work of Mullins and Sekerka.[51],[52]

3.2.1 Interface Stability of a Single Solidifying Particle

Langer's treatment assumes a single particle surrounded by an infinite amount of liquid, with spherical harmonic functions describing a slightly perturbed spherical solid-liquid interface.[53] A perturbation amplification factor, ω_j, is associated with the perturbation corresponding to the spherical harmonic function of order j:

$$\omega_j = \frac{(j-1)V}{R}\left[1 - \left(1 + \frac{1}{j} + \beta\right)\frac{D_L \Gamma j(j+2)}{m_L C_0 (k-1) V R^2}\right] \tag{3.15}$$

where V is the growth velocity of the spherical interface, R is the sphere radius, β is a parameter equal to the ratio of solute mobility in the solid to that in the liquid (assumed to be so small that β can be set to zero). A positive amplification factor means a given perturbation will grow, and a negative one represents a perturbation which will vanish. The derivation of Equation 3.15 is lengthy and therefore not included here. The reader is referred to the original Mullins and Sekerka and Langer papers.[51]-[53].

In typical alloy solidification, nascent dendrite arms (perturbations) develop and grow along the six [100] directions, which correspond to a particle perturbed by the spherical harmonic of order $j = 4$. Using this j value, setting Equation 3.15 equal to zero (representing when the dendritic perturbations can begin to grow), and rearranging leads to a relationship between the particle radius, R, and the growth velocity, V:

$$R = \left(\frac{30 D_L \Gamma}{m_L C_0 (k-1) V} \right)^{1/2} \tag{3.16}$$

Equation 3.16 is plotted in Figure 3-18 using property values for Al-4.5wt%Cu alloy (Appendix B). The region below the curve represents stable combinations of particle size and growth velocity, and the region above the curve are combinations of particle size and growth velocity which will lead to an unstable interface. Equation 3.16 only expresses when a perturbation on the particle interface will begin to grow, but does not consider the growth rate of the perturbations in relation to the advancement of the spherical interface. Hence, Figure 3-18 is plot of the *minimum* stable particle radii for each growth velocity.

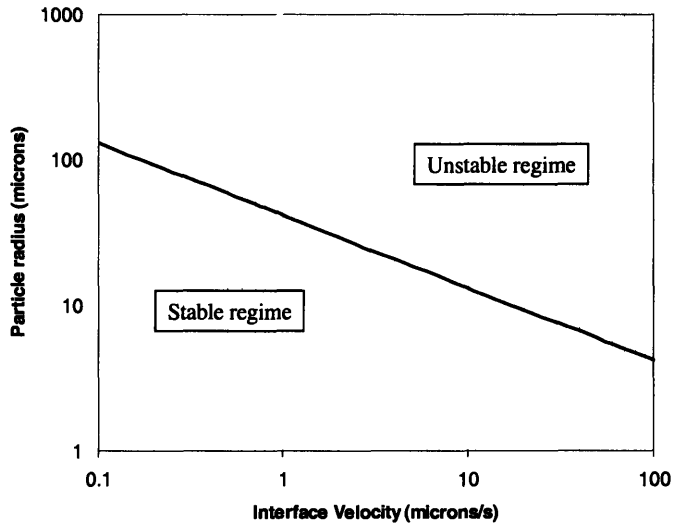

Figure 3-18: The minimum stable particle radius as a function of growth velocity obtained by applying the analysis of Langer to rheocast Al-4.5wt%Cu alloy. The curve is for a single particle surrounded by an infinite amount of liquid phase.

3.2.2 Modified Interface Stability for Rheocast Alloy

Figure 3-18 shows that for a single particle in an infinite liquid surrounding, stability is favored by lower interface velocities and smaller particle radii. This stability criterion cannot consider the effects of overlapping diffusion fields due to the presence of neighboring particles. It also does not consider the time required for a once stable interface become unstable enough to significantly alter the particle morphology. Collaboration with Professor Karma (Physics Department, Northeastern University) resulted in a simple theory which incorporates diffusion field overlap. The model was designed to predict the relationship between the solid fraction in rheocast alloy and the maximum cooling rate to maintain stable particle growth.[67] In the model, the LDC particle growth model and a standard treatment for the stability of a perturbed flat interface are combined.

The combination of Figure 3-13 and 3-16 show that the LDC model of particle growth during "slow cooling followed by fast cooling" predicts the growth velocity of a particle during the fast cooling stage will reach a maximum and begin to decrease rapidly when the solute fields surrounding neighboring particles begin to overlap (marked by a rise in solute concentration at radius R_T in Figure 3-13). The time it takes for this to happen must depend on the particle size when fast cooling begins, and on cooling rate.

To develop a stability model for rheocast slurries, it is assumed:

Condition 1 *A particle in the rheocast alloy will always be stable if the surrounding solute field begins to interact with neighboring particle fields before the interface becomes unstable.*

The variable Δt_0 will be defined as the time it takes for solute fields to interact, and Δt_u will be the time it takes for a particle interface to become unstable. Both Δt_0 and Δt_u are measured from the time that fast cooling begins. According to the condition, if $\Delta t_0 < \Delta t_u$ the particle interface will always be stable, and if $\Delta t_0 > \Delta t_u$ the particle interface will become unstable. Therefore, the maximum cooling rate that maintains stable particle growth must be when:

$$\Delta t_0 = \Delta t_u \tag{3.17}$$

Expressions for Δt_0 and Δt_u will be derived and equated to approximate the relationship between particle size, cooling rate, and interface stability for particles in rheocast alloy.

In the LDC model of a quenched alloy, the maximum growth velocity of solidifying particles is reached at time Δt_0, when solute fields begin to interact. For particles of initial radius R_i (which can grow to a maximum radius R_T), the time it takes for solute fields to interact is proportional to the square of the distance separating particles, ΔR ($\Delta R = R_T - R_i$), divided by the solute diffusivity in the liquid :

$$\Delta t_0 = a\frac{(\Delta R)^2}{D_L} \tag{3.18}$$

where a is the pre-factor of the proportionality.

Recall that Equation 3.14 accurately describes the LDC model growth velocity up to the maximum growth velocity when solute field interaction begins. The maximum growth velocity can be expressed by substituting Equation 3.18 into 3.14:

$$V_{\max} = A_1\frac{\dot{T}}{m_L C_0(k-1)}(\Delta R) \tag{3.19}$$

where A_1 is a new pre-factor combining the pre-factors a and A of Equations 3.18 and 3.14.

From interface stability theory, the amplification rate, ω, of a linear perturbation of wave-vector $K = \frac{2\pi}{\lambda}$ (where λ is the wavelength of the perturbation) is:

$$\omega = VK - \left(\frac{D_L\Gamma}{m_L C_0(k-1)}\right)K^3 \tag{3.20}$$

By differentiating Equation 3.20, setting $\frac{d\omega}{dK} = 0$ and $V = V_{\max}$, the wave-vector for the perturbation being amplified the fastest, $K_{\max}$, can be obtained:

$$K_{\max} = \left(\frac{(V_{\max})m_L C_0(k-1)}{3D_L\Gamma}\right)^{\frac{1}{2}} \tag{3.21}$$

Substituting Equation 3.21 into 3.20 gives the maximum amplification rate:

$$\omega_{\max} = \frac{2}{3}\left(\frac{(V_{\max})^3 m_L C_0(k-1)}{3D_L\Gamma}\right)^{\frac{1}{2}} \tag{3.22}$$

The time for a particle to become morphologically unstable, Δt_u, must be inversely proportional

to the maximum amplification rate:

$$\Delta t_u = B\left(\frac{D_L\Gamma}{(V_{\max})^3 m_L C_0(k-1)}\right)^{\frac{1}{2}} \tag{3.23}$$

where B is a pre-factor for the proportionality.

Substituting Equations 3.18, 3.23, and 3.19 into 3.17 and solving for ΔR yields:

$$\Delta R = C\left[\frac{(D_L)^3\left[m_L C_0(k-1)\right]^2\Gamma}{(\dot{T}_{\max})^3}\right]^{\frac{1}{7}} \tag{3.24}$$

where C is the new pre-factor and $\dot{T}_{\max}$ is the maximum cooling rate that will allow stable growth. Substituting $(R_T - R_i)$ for ΔR and solving for R_i gives the expression

$$R_i = R_T - C\left[\frac{(D_L)^3\left[m_L C_0(k-1)\right]^2\Gamma}{(\dot{T}_{\max})^3}\right]^{\frac{1}{7}} \tag{3.25}$$

Dividing by R_T gives

$$\left(\frac{R_i}{R_T}\right) = 1 - \frac{C}{R_T}\left[\frac{(D_L)^3\left[m_L C_0(k-1)\right]^2\Gamma}{(\dot{T}_{\max})^3}\right]^{\frac{1}{7}} \tag{3.26}$$

Assuming that the the solid fraction in a system of perfect spheres of radius R_i can be described as $f_s = \left(\frac{R_i}{R_T}\right)^3$, cubing both sides of Equation 3.26 gives a relationship between the solid fraction and the maximum cooling rate for interface stability:

$$f_s = \left[1 - \frac{C}{R_T}\left[\frac{(D_L)^3\left[m_L C_0(k-1)\right]^2\Gamma}{(\dot{T}_{\max})^3}\right]^{\frac{1}{7}}\right]^3 \tag{3.27}$$

The relationship between f_s and $\dot{T}_{\max}$ is a function of R_T. The parameter R_T can be converted to particle density, N, using the expression

$$N = \frac{1}{\frac{4}{3}\pi\left(R_T\right)^3} \tag{3.28}$$

which yields:

$$f_s = \left[1 - C\left(\frac{4\pi N}{3}\right)^{\frac{1}{3}}\left[\frac{(D_L)^3\left[m_L C_0(k-1)\right]^2\Gamma}{(\dot{T}_{\max})^3}\right]^{\frac{1}{7}}\right]^3 \tag{3.29}$$

Figure is a plot of solid fraction as a function of cooling rate according to Equation 3.29 for Al-4.5wt%Cu alloy. Plots for several particle densities are given. The prefactor of $C = 1.2$ was used to generate each curve. For any curve corresponding to a given particle density, the region to the left of the curve represents combinations of solid fraction and cooling rate that will lead to particle stability, and the region to the right of the curve represents unstable particle growth.

For a given solid fraction, Figure 3-19 shows that a larger particle density will allow stable particle growth at higher cooling rates than a lower particle density. All curves show that higher solid fractions maintain stable particle growth at higher cooling rates than lower solid fractions. Kattamis found this to be the case with spheroidal particles in $Mg - 5.1\ wt\%Zn$ alloy.[68] Since higher solid fractions must correspond to larger particles, and higher cooling rates induce faster growth velocities, the interface stability theory for rheocast alloy shown in Figure 3-19 predicts the opposite trend shown in the previous interface stability theory for a single solidifying particle, Figure 3-18, which indicated that smaller particles can maintain stability at higher growth velocities than larger ones. Both stability theories will be compared to experimental data in a subsequent section.

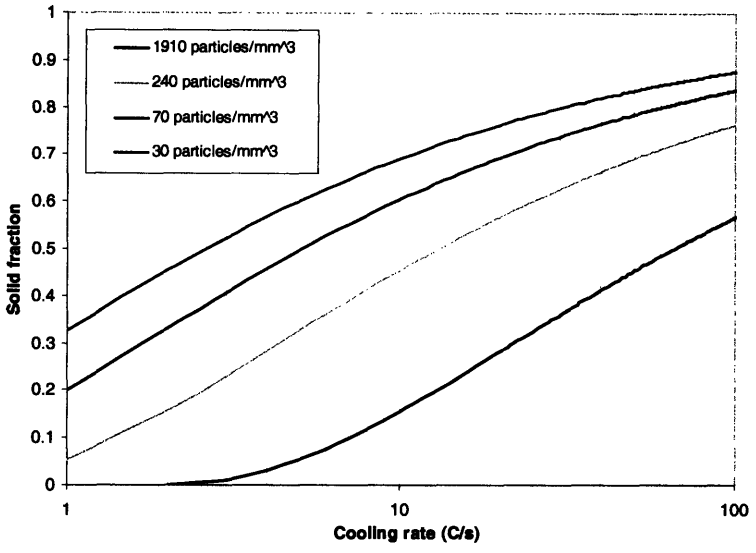

Figure 3-19: Modified particle stability model for rheocast Al-4.5wt%Cu alloy which considers solute field overlap during solidification. The stability criterion is a function of the particle density in the rheocast slurry. For a given particle density, the region to the left of the curve represents particle stability, and the region to the right of the curve represents combinations of solid fraction and cooling rate that will lead to unstable particle growth.

Chapter 4

Experimental Study of Rheocast Microstructures

4.1 Setup Description

An experimental setup was built to study the microstructure and flow behavior of rheocast aluminum alloys. Figure 4-1 is an illustration of the equipment used. The setup had three components: a melt held in a resistance furnace with a removable lid, a rotating copper rod attached to a pneumatic piston, and a copper quench mold attached to a second pneumatic piston and a vacuum reservoir. By operating the pneumatic pistons with a set of switches, both the copper rod and the quench mold could be immersed in the melt held in the furnace at various times and at various melt temperatures.

4.1.1 Melt

For the microstructural studies, Al-4.5wt%Cu alloy was used. In the fluidity experiments, *A*357 alloy was used. Relevant physical properties for both alloys can be found in Appendix B. The amount of alloy used in most experiments was 745 ± 5 *grams*. The metal was held in a thin-walled steel crucible coated in boron nitride spray (Advanced Ceramics Corporation). The bulk melt temperature was measured by at least one K-type thermocouple contained in a 0.2 *cm* ID, OD 0.3 *cm* quartz tube. Melt temperatures were recorded by an Omega® OM3000

Datalogger which acquired readings at 1 Hz. When faster acquisition was needed, temperature measurements were recorded with a SuperLogics USB-9806 data acquisition module capable of acquiring temperature measurements at over 1000 Hz.

4.1.2 Stirring rod

The copper rod used to stir the melt was 2.86 cm in diameter and 25.5 cm long, with a rounded end. The copper rod was at room temperature (between 22 and 30°C) before being immersed in the metal. Four identical and interchangeable rods were made to eliminate the need to wait for a used rod to cool to room temperature to perform another experiment. Figure 4-2(a) shows the geometry and dimensions of the crucible, melt and copper rod.

4.1.3 Quench mold

Six identical quench molds were made. The molds consisted of two 1.27 cm thick copper plates separated by 0.1 cm thick "graphite felt" spacers obtained from Alpha Aesar. The thin-channel created between the copper plates was roughly 0.08 cm thick, 3 cm wide, and 12.5 cm long. For each experiment, the quench mold used was initially at room temperature, between 22 and 30°C. The top end of the mold was connected to a vacuum reservoir which could be set to a variety of vacuum levels. The bottom end of the mold was sealed with Saran^{TM} wrap, which adequately sealed the vacuum within the mold. In the lowered position, the bottom 1 cm of the quench mold was immersed into the melt. The Saran^{TM} wrap melted almost instantly when the quench mold was lowered, and metal was drawn upwards into the evacuated channel. Figure 4-2(b) shows the geometry and dimensions of the quench molds.

In order to approximate how fast metal would flow into the quench molds, an initial test was performed in which two K-type thermocouples (sheathed, ungrounded, 0.051 cm dia.) were incorporated in the assembly of a quench mold, and metal was drawn into the quench mold with a pressure drop of 400 $torr$. The thermocouples were placed near the bottom entrance of the quench mold, and spaced 2 cm apart. Figure 4-3(a) is a photographs of the thermocouples, graphite felt spacers, and interior surface of an open quench mold before assembly. Just the tips of the thermocouples were allowed to extend past the graphite felt spacers, slightly protruding into the channel, with the lower thermocouple protruding less than the upper one.

The thermocouples were sandwiched between the two copper blocks and pressed into the soft graphite felt spacers. This adequately sealed the mold to sustain the desired pressure drop of 400 *torr*. The thermocouples were connected to the data acquisition module programmed to acquire temperature measurements at 1000 Hz. After the mold was assembled, the bottom entrance was sealed with Saran^{TM} wrap and the pressure drop of 400 *torr* was established. The mold was plunged into an Al-4.5wt%Cu melt at 653°C (roughly 4°C above the measured liquidus temperature) and metal was drawn into the channel as temperature was acquired. The experimental parameters for this experiment can be found in Appendix C, experiment #1.

Figure 4-3(b) shows the temperature data acquired during the experiment. A time interval of 0.007 seconds separated the temperature spikes recorded by the two thermocouples separated 2 *cm*, yielding an average flow velocity, v, of 286 cm/s. With this velocity measurement, the Reynold's number for the experiment could be estimated according to the definition:

$$\mathrm{Re} = \frac{\rho v \delta}{\eta} \tag{4.1}$$

where ρ is the fluid density, v is the average fluid velocity, δ is the half-thickness of the channel (0.04 *cm*), and η is the fluid viscosity (viscosity estimated to be that of pure liquid aluminum just above its melting point [69]) . Using the values for Al-4.5wt%Cu alloy in Appendix B, the Reynold's number was calculated to be 2670, slightly larger than the laminar-to-turbulent transition (2100).

4.1.4 Coatings

Both the immersed portion of the copper rod and the interior of the quench molds were spray-coated with Slip Plate® graphite dry film lubricant spray (Superior Graphite Co.) to avoid dissolution of the copper in the molten alloy. The quench molds were coated at the same time to ensure uniformity in the coating thickness. After being coated, both the rods and the molds were heated to 330°C for 15 minutes to burn off organic solvents, then allowed to cool to room temperature before use in experiments. This procedure was done to reduce the amount of gas which could evolve from the coated copper surfaces when contacted by the molten metal.

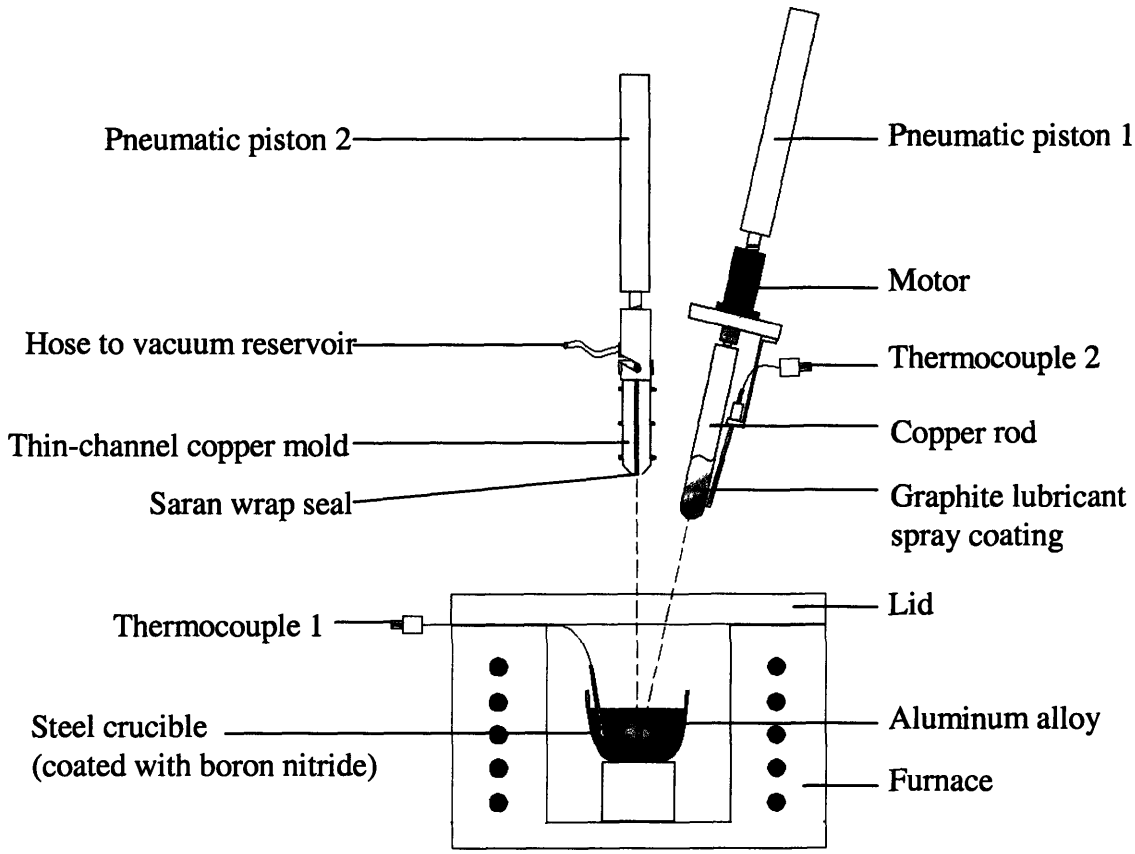

Figure 4-1: Schematic of equipment designed and built for this study.

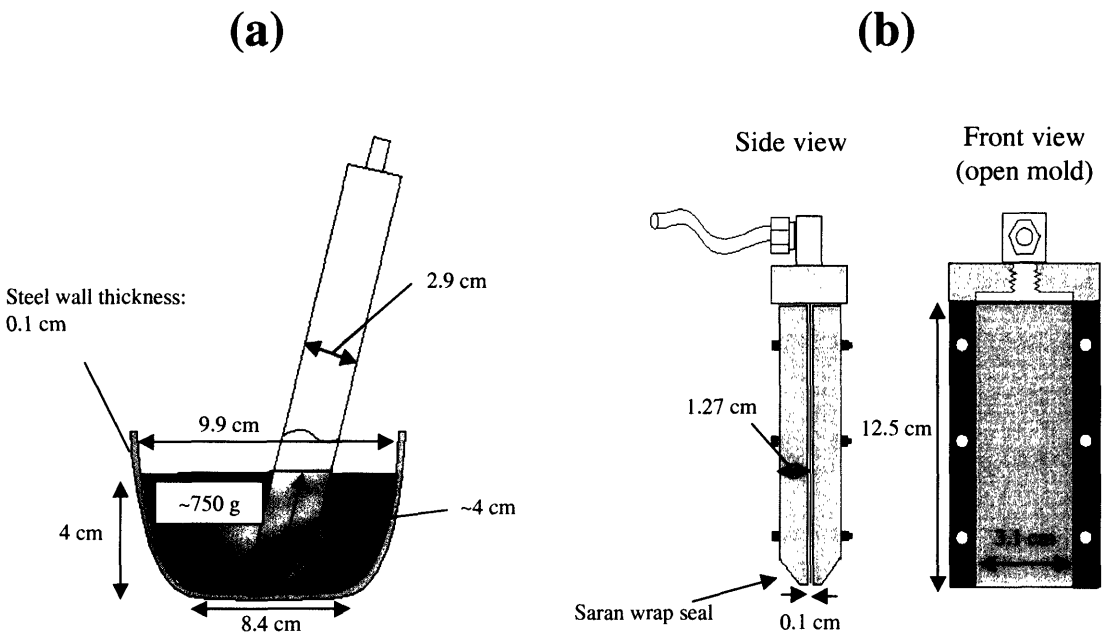

Figure 4-2: (a) Schematic of the crucible, melt, and copper rod. (b) Schematic of the quench molds.

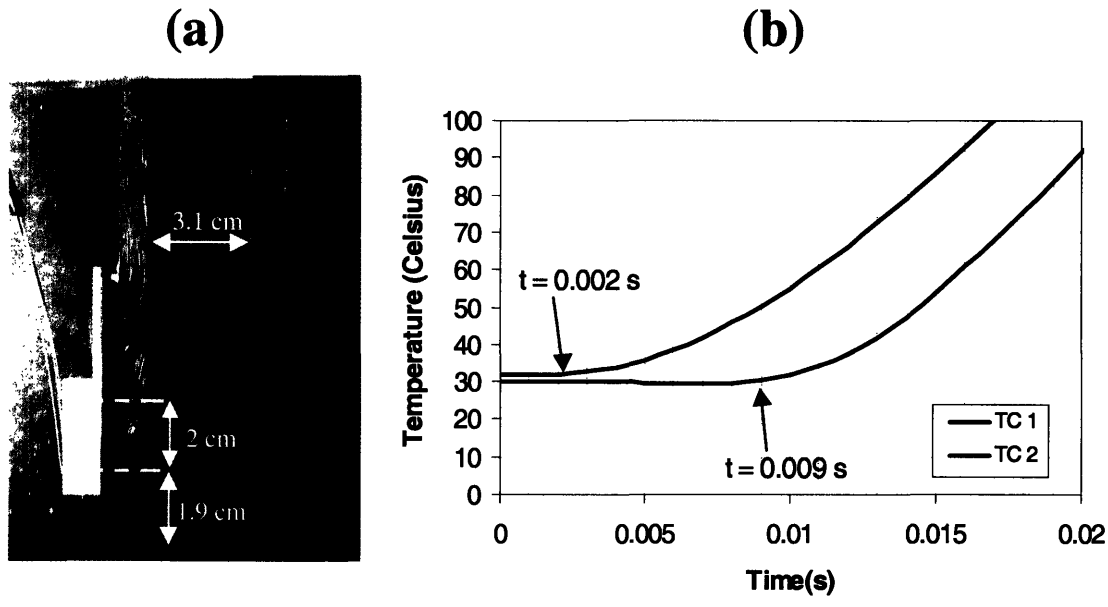

Figure 4-3: (a) Photograph showing the placement of thermocouples inside the quench mold for measurement of the flow velocity of the alloy as it entered the mold. The thermocouples were separated 2 *cm* apart inside the quench mold. (b) Temperature readings obtained from the two thermocouples inside the quench mold as slightly superheated liquid was drawn into the quench mold with a ΔP of 200 *torr*.

4.2 Types of Experiments

The experimental setup shown in Figure 4-1 gave the flexibility to perform a variety of solidification experiments:

- A very fine equiaxed dendritic structure was created by drawing fully liquid metal into the quench mold. This dendritic microstructure was reheated above the eutectic temperature for various times and quenched.
- Rheocast structures were obtained by stirring and cooling a melt with the copper rod. Microstructures were captured at early times of solidification by drawing metal into the quench mold.
- The stability of particle-liquid interfaces in the rheocast alloy was analyzed as a function of cooling rate and solid fraction.
- The fluidity of fully liquid and of the partially solidified rheocast alloy was evaluated by measuring the average length of metal drawn into the quench mold.

The procedures used in each type of experiment varied significantly. For clarity, the description of the procedure for each type of experiment is included in the next section, preceding the corresponding set of experimental results.

Chapter 5

Experimental Procedures & Results

5.1 Defining Rheocast and Conventional-Cast Microstructures

5.1.1 Procedures

Two preliminary experiments were performed to show the microstructural difference between rheocast and conventional-cast Al-4.5wt%Cu alloy. The conventional-cast microstructure was obtained by holding the alloy in the furnace a few degrees above the liquidus temperature, turning off the furnace and removing the furnace lid. The time it took the alloy to cool from the liquidus temperature, $649°C$, to the eutectic temperature, $550°C$, was roughly 9 minutes. The rheocast material was created by holding the alloy in the furnace a few degrees above the liquidus temperature, turning off the furnace, immersing the copper rod (rotating at 409 *rpm*) into the melt for 10 seconds which cooled the melt a few degrees below the liquidus (rheocasting), removing the rod, and allowing the slurry to cool in the furnace with the lid removed. The solidification time for the rheocast metal was also approximately 9 minutes. Parameters for both experiments described are in Appendix C, experiment # 2, 3.

Samples from both the conventional-cast and rheocast ingots were cut from an identical location: half-way between the top and bottom of the ingot, half the distance between the center and edge. The samples were polished and etched with Keller's reagent.

5.1.2 Microstructures

Figure 5-1(a) shows the microstructure of conventional-cast alloy, with large dendrites and coarsely spaced secondary arms. The dendrites are surrounded by eutectic composition which appears darker in the micrograph. Figure 5-1(b) shows the rheocast microstructure consisting of large, spheroidal particles surrounded by the eutectic located at particle boundaries. The Keller's etch darkened the regions within the particles with higher copper content. Most of the particles shown in Figure 5-1(b) have a spheroidal central region that is lightly shaded, surrounded by a ring of darker shading.

5.1.3 Microprobe

The copper distribution within a rheocast particle was measured with a microprobe (model JEOL Superprobe 733) which had a minimum copper detection limit of 0.08 $wt\%Cu$. The error in copper concentration measurements was $3-4\%$ of the measured value. Figure 5-2(a) and (b) show the back-scattered electron image of a rheocast particle and the copper content along the particle diameter, respectively. A relatively constant copper concentration of about 1 $wt\%Cu$ spans ± 25 μm from the center of the particle. The copper content then increases moving further away from the particle center. The microprobe analysis confirmed that the darkened regions in etched micrographs, the periphery of the particles, did correspond to regions of higher copper content.

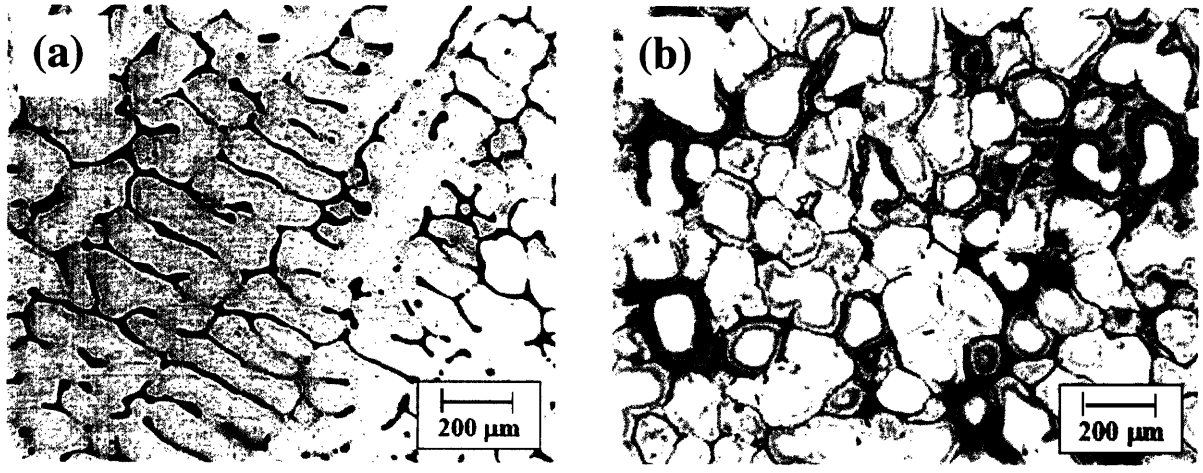

Figure 5-1: (a) Conventional-cast structure of Al-4.5wt%Cu alloy cooled without immersing the copper rod. (b) Rheocast structure obtained by immersing the copper rod into a slightly superheated melt, allowing it to stir and cool the melt a few degrees below the liquidus temperature, removing the rod, then allowing the alloy to cool.

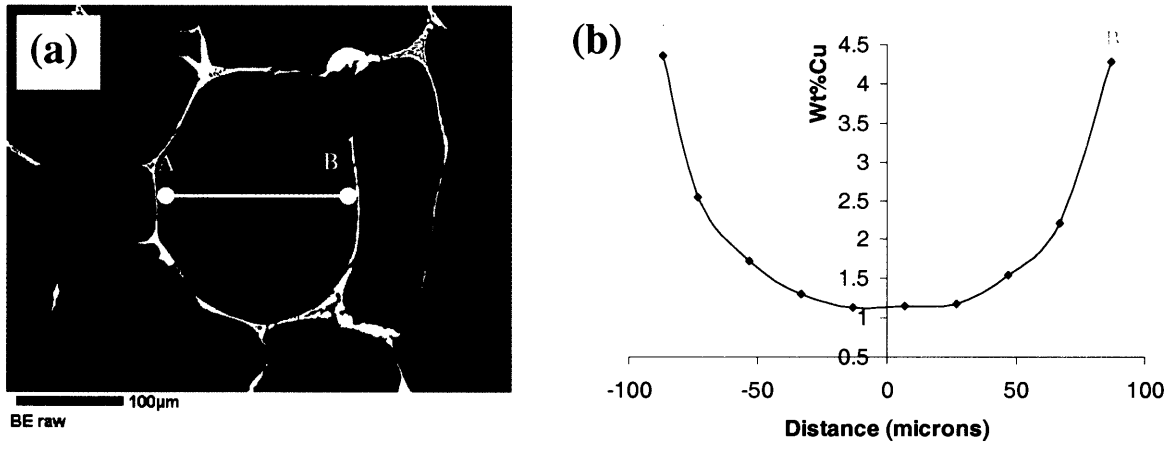

Figure 5-2: (a) Back-scattered electron image of a rheocast particle in Al-4.5wt%Cu alloy (b) Copper content within the particle measured by a microprobe line-scan.

5.2 Formation of Spheroidal Microstructure by Reheating of Equiaxed Dendrites

5.2.1 Procedures

A fine dendritic Al-4.5wt%Cu material was made by drawing slightly superheated liquid alloy into the quench mold, which formed a 0.08 cm thick plate. Samples with dimensions 1 cm X 1 cm X 0.08 cm were cut from the plate. Each sample was wrapped in a thin steel foil along with the tip of a thin K-type thermocouple that had a 0.25 second response time. The tip of the thermocouple was held in contact with the surface of the samples by steel alligator clips located on the outside of the steel foil. Each assembly was plunged into a tin bath at a temperature between 620 and 630°C, well above the Al-Cu eutectic temperature (550°C), and temperature was recorded. Five experiments were performed in which the temperature of a sample remained above the eutectic temperature for 5, 15, 60, 120, and 480 seconds, respectively. Each sample was water quenched immediately after being removed from the tin bath. Each reheated sample was polished using standard metallographic techniques, and etched with Keller's reagent. The conditions for each experiment can be found in Appendix C, experiments #'s 4-9.

5.2.2 Microstructures

Figure 5-3(a) shows the initial dendritic microstructure used in the reheating experiments. The grain size and dendrite arm spacing are approximately 20 μm and 5 μm, respectively. Based on this estimate of dendrite arm spacing, the cooling rate for the metal in the quench mold was estimated to be about 375°C/s (Appendix D). Figures 5-3(b)-(f) show the microstructural changes which occurred after reheating this material above the eutectic temperature for 5, 15, 60, 120, and 480 seconds, respectively. For reheating times as short as 5 seconds, the equiaxed dendrites evolved into spheroidal grains. The spheroids grew larger in samples reheated for longer times. In all of the reheated dendritic microstructures there is entrapped eutectic within the spheroidal grains.

Figure 5-4 is a high magnification image of a somewhat over-etched region of the sample reheated above the eutectic temperature for 5 seconds. It is possible to see the "cross-shaped" outlines of the original equiaxed dendrite in the darker grain in the center of the micrograph.

Entrapped eutectic pockets are visible in regions which were originally between the initial dendrite arms.

5.2.3 Grain Size Evolution

The growth of the average spheroid size in the reheated dendritic material was determined as a function of the total time it remained above the eutectic temperature: the "solidification time" for these samples. Three micrographs were taken from random locations in each reheated dendritic sample. The average grain size in each sample was measured using the line-intercept method. A grid of 10 random lines was placed over each micrograph and the number of grains intercepted per unit length of test line, N, was determined for each line. The linear grain size, L, obtained from the measured N value for each line is:

$$L_{line} = 1/N \tag{5.1}$$

The ten L_{line} values obtained from each micrograph were averaged, giving L_{micro}. The three L_{micro} values were averaged over the three micrographs taken from each reheated sample and defined as L_{sample}.

A standard procedure (derived from a simple statistical analysis) to improve estimates of three-dimensional particle diameters using the two-dimensional L_{sample} measurements is:

$$D_{3D} = 1.5 L_{sample} \tag{5.2}$$

where D_{3D} is the three-dimension grain diameter estimate. The average grain radius, R_d, was obtained by dividing D_{3D} dividing by two. The subscript "d" was used to indicate that the spheroidal grains were obtained from reheating dendritic alloy. Between 170 and 380 grains were analyzed for each reheated sample. Relevant data for the quantitative metallography described can be found in Appendix C, experiments #'s 5a-9a.

The average grain radius for each reheated dendritic sample, R_d, is plotted in Figure 5-5. Also included in the plot is the classic ripening curve for the dendrite arm spacing in Al-4.5wt%Cu alloy. For a given solidification time, the grain size in reheated dendritic material follows the ripening curve closely.

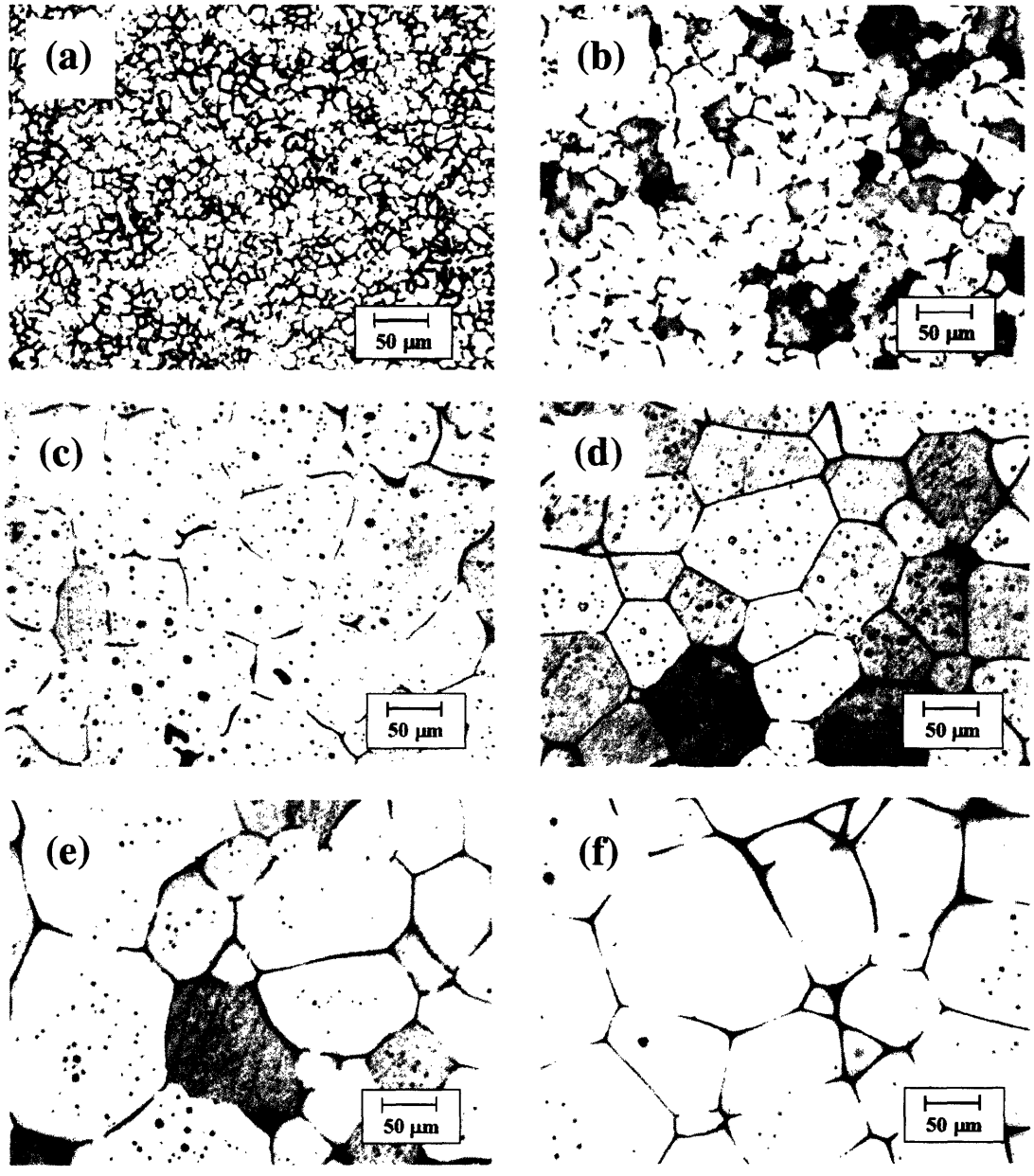

Figure 5-3: (a) Microstructure of an Al-4.5wt%Cu sample cast by drawing slightly superheated liquid alloy in the quench mold with a ΔP of 400 *torr*. Microstructures after reheating structure shown in (a) above the eutectic temperature for (b) 5 (c) 15 (d) 60 (e) 120 (f) 480 seconds.

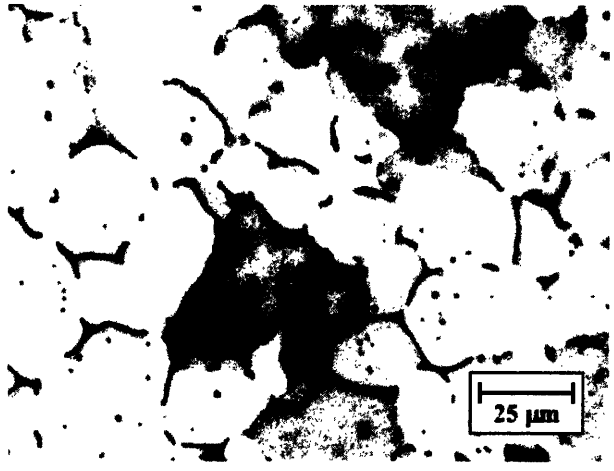

Figure 5-4: A spheroidizing grain in the dendrititc sample after reheating it above the eutectic temperature for 5 seconds. The cross-shaped outline of the initial dendrite which has ripened is evident.

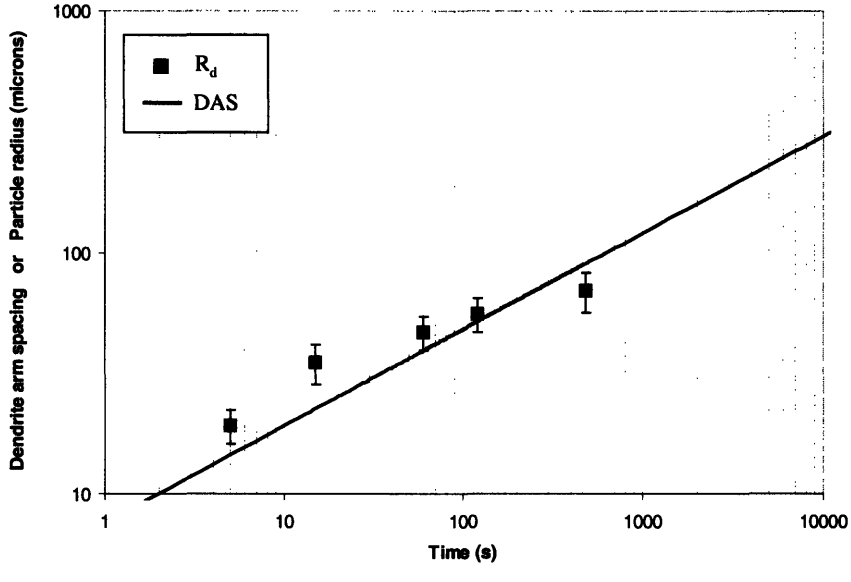

Figure 5-5: The grain size evolution in reheated dendritic Al-4.5wt%Cu alloy compared with the classic ripening curve for the dendrite arm spacing evolution in dendritic alloy.

5.3 Growth of Spheroidal Particles in Rheocast Alloy

5.3.1 Procedures

In order to study the microstructure of rheocast Al-4.5wt%Cu alloy during the initial stages of solidification, a set of experiments was performed in which the quench mold was plunged into the melt after the copper rod had stirred and cooled it below the liquidus temperature for various times. The Al-4.5wt%Cu alloy was first melted and held in the furnace at $653°C$, roughly $4°C$ above the measured liquidus temperature. The copper stirring rod (at room temperature) was then immersed into the melt, removing the $4°C$ of superheat almost instantly. Once the liquidus temperature was reached, the cooling rate was approximately $0.28°C/s$. Using the measured cooling rate and the physical properties of the melt and copper rod, the heat transfer coefficient for rod-melt interface was estimated to be roughly 2500 $\frac{W}{m^2 s}$ (Appendix E).

Two experiments were conducted in which the coated copper rod (rotating at 409 rpm) stirred the melt below the liquidus temperature for 5 and 20 seconds before metal was drawn into the quench mold. An additional two experiments were conducted in which the copper rod stirred the melt below the liquidus temperature for 20 seconds, was removed, and metal was drawn into the quench mold after it had been below the liquidus temperature for a total of 60 and 200 seconds. Using the Scheil relation in Equation 3.9, and alloy data in Appendix B, the percent solid in the rheocast slurries at the time of quench was estimated to be 5% for the 5 second sample, 18% for the 20 second sample, 30% for the 60 second sample, and 41% for the 200 second sample. All experimental parameters are tabulated in Appendix C, experiment #'s 10-13.

The metal drawn into quench mold produced specimens in the shape of a thin plates. The plates were cross-sectioned vertically, exposing the interior microstructure at the top and bottom of the samples. The samples were polished using standard metallographic techniques and etched with Keller's reagent.

5.3.2 Microstructures

Figure 5-6(a)-(d) show the typical rheocast microstructure found in each of samples quenched after being below the liquidus temperature for 5, 20, 60, and 200 seconds. In all of the

micrographs, spheroidal primary solid particles are surrounded by an equiaxed dendritic region. The size of the spheroidal particles increases with increasing time before quench. The rheocast particles in all of the micrographs are essentially free of any entrapped eutectic compositions. The secondary dendrite arm spacing in the dendritic region surrounding spheroidal particles is about 5 μm, again indicating a cooling rate of roughly $375°C/s$ (Appendix D).

It is possible to identify a lighter shaded spherical region in the center of several spheroidal particles in Figure 5-6(a)-(d). The lighter shaded particle centers indicate that there is a lower copper content in this region than the darker periphery surrounding the particle centers. These lighter particle centers are clearly spheroidal in shape and identifiable even within some particles in the sample that was quenched after being below the liquidus for just 5 seconds.

5.3.3 Microprobe

The JEOL Superprobe 733 was used to measure the composition within two spheroidal particles in the sample quenched after 20 seconds of rheocasting. Figure 5-7(a) and (b) show the back-scattered electron images of the two particles, and Figure 5-7(c) shows the measured copper content along the particle diameters. In both particles, the central region of ± 20 μm has about 1 $wt\%Cu$ copper. Closer to the center of the particles the copper content is slightly higher, about 1.1 $wt\%Cu$. At radial distances greater than 20 μm away from the particle centers, the copper content in both particles increases abruptly.

The composition profiles shown in Figure 5-7(c) suggest that the particles grew to roughly 20 μm in radius during the 20 second period of slow cooling before the alloy was quenched. The particle size when the alloy was drawn into the quench mold is marked by the sharp increase in solute concentration at the 20 μm radius. Based on the microprobe profiles shown in Figure 5-7(c), it is concluded that the lightly shaded spherical particle centers seen in etched micrographs delineate the solid phase that was present at the time of quench, and that the darker shaded surrounding periphery comprises solidification which occurred during quench. This interpretation of the etched micrographs was used in the particle size measurements described in the next section.

5.3.4 Particle Size Evolution

About ten micrographs were taken from random locations in each of the rheocast samples quenched after being below the liquidus temperature for 5, 20, 60, and 200 seconds. Average sized particles in which the etching revealed the lightly shaded central region were identified in each of the micrographs. The diameter of the lightly-shaded central region, considered to be the particle size just before the quench, will be referred to as the "initial particle diameter". The "final particle diameter", which considered the spheroidal growth which had occurred during the quench, included the darker shaded spheroidal ring surrounding the lighter center.

Measurements of both initial and final particle diameters were taken by hand. For each particle, two sets of measurements were taken in roughly orthogonal directions, then averaged. The initial diameters of approximately 30 particles from each sample were estimated, except for the sample quenched after 200 seconds in which lightly shaded centers were observable in only 10 particles. The final particle diameter of at least 79 particles was estimated for each sample.

As before, the standard method to improve estimates of three-dimensional particle diameters using the two-dimensional diameter measurements was used:

$$D_{3D} = 1.5 D_{2D} \tag{5.3}$$

where D_{3D} is the estimated three-dimensional particle diameter and D_{2D} is the average two-dimensional diameter measurements. The D_{3D} values obtained from Equation 5.3 were converted to particle radii by dividing by two. Relevant data for the quantitative metallography described can be found in Appendix C, experiment #10a-13a.

The initial particle radius before quench was defined as R_i, and the final particle radius after quench was defined as R_f. Figure 5-8 shows a logarithmic plot with the average R_i and R_f calculated for each of the samples quenched after 5, 20, 60, and 200 seconds of rheocasting. Again, the classic ripening curve for the dendrite arm spacing in Al-4.5wt%Cu alloy is included. The plot shows that in rheocast alloy, the measured R_i values follow the ripening curve closely, with all values slightly above the curve and the deviation being greater at the shorter solidification times.

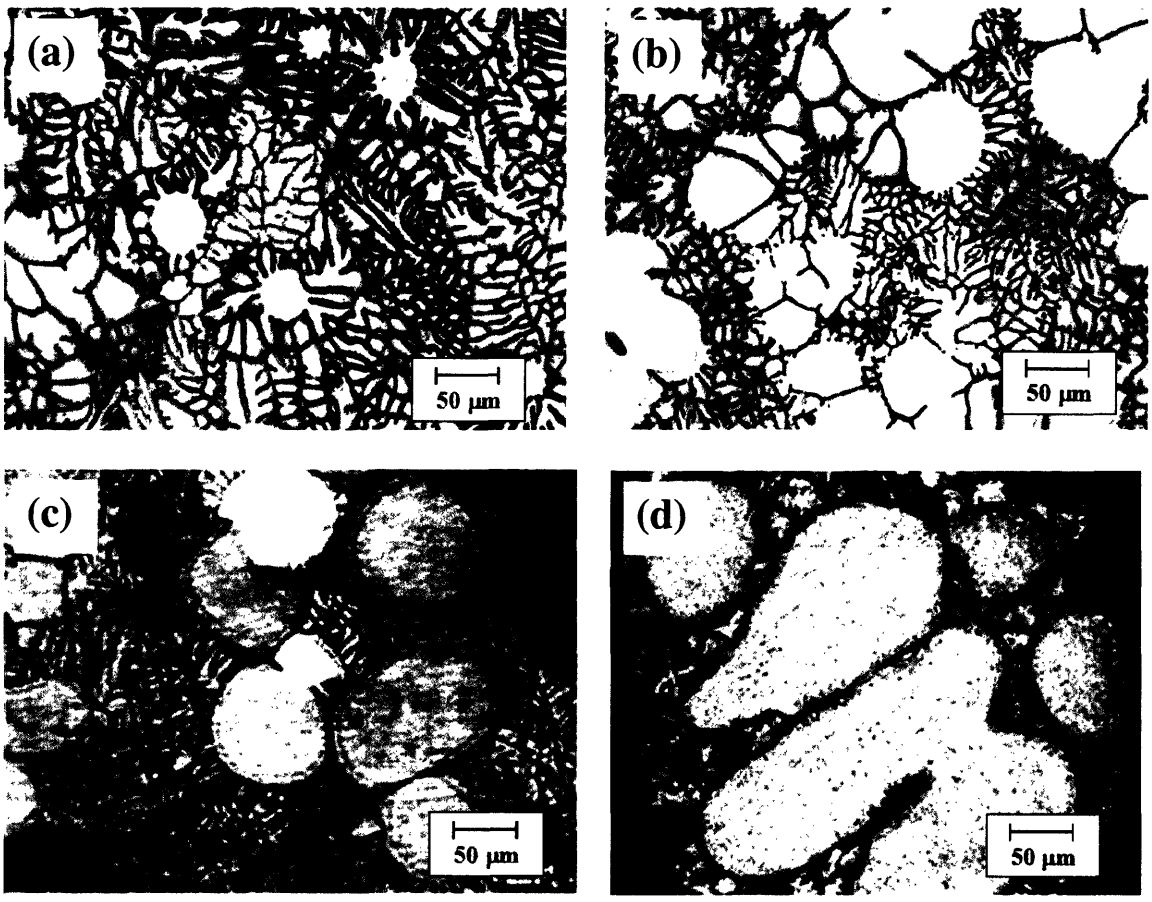

Figure 5-6: Microstructure of rheocast Al-4.5wt%Cu alloy quenched after being stirred by the rod, remaining below the liquidus temperature for (a) 5 (b) 20 (c) 60 and (d) 200 seconds.

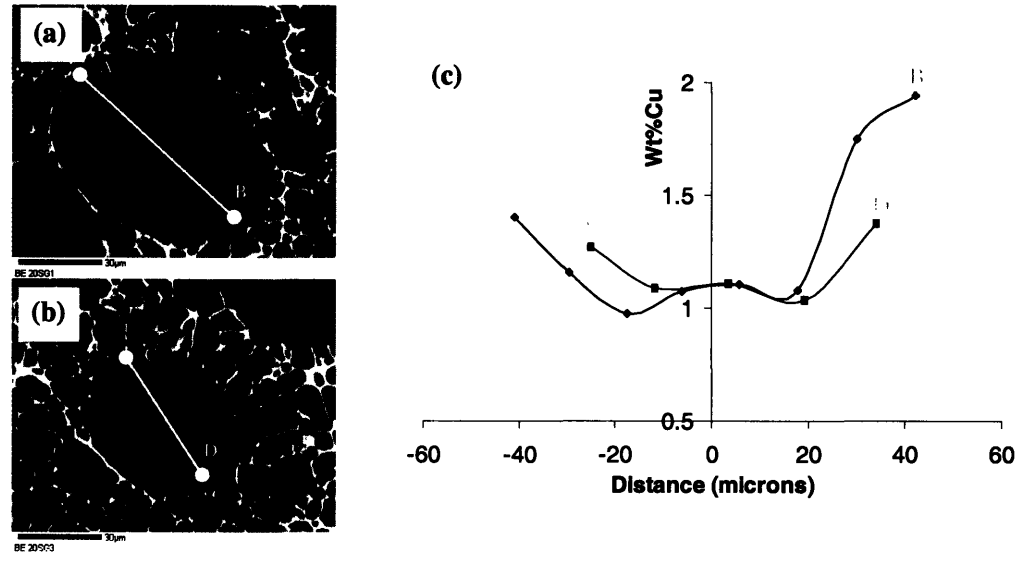

Figure 5-7: (a), (b) Back-scattered electron images of rheocast particles in the Al-4.5wt%Cu alloy sample quenched after being rheocast for 20 seconds (c) copper content measured within the particles.

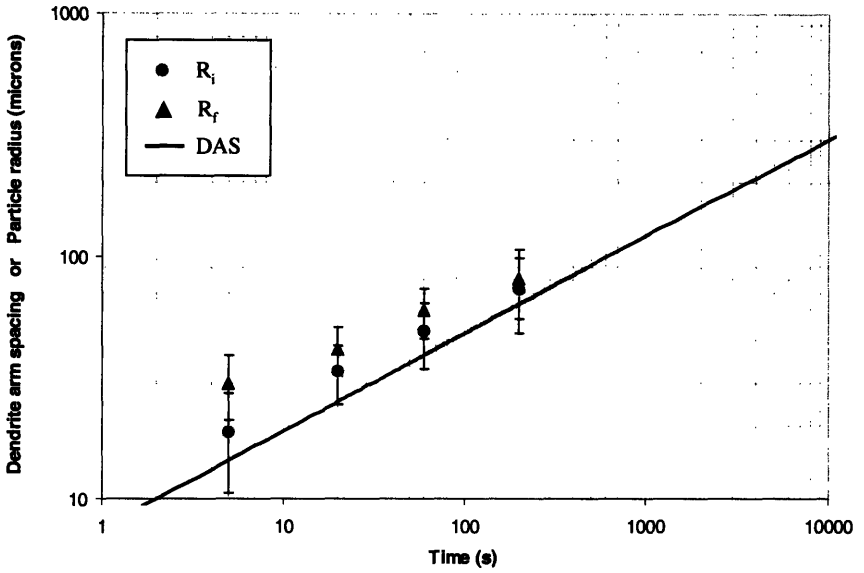

Figure 5-8: Particle size measurements of rheocast and quenched Al-4.5wt%Cu alloy compared with the classic ripening curve for the dendrite arm spacing in dendritic alloy. The points labeled "R_i" are the average particle radius at the time of quench, and "R_f" is the average particle radius including the growth which occurred during the quench.

5.3.5 Data Comparison with Models

Particle size evolution

To compare the experimental data for rheocast particle sizes as a function of solidification time with model predictions, the models required an appropriate estimate for R_T. The average distance separating particle centers in the rheocast microstructures shown in Figures 5-6(a)-(d) was estimated to be 100 μm. Dividing by two gave an R_T of 50 μm. Using this value for R_T, Figure 5-9 compares the three particle growth models with the experimental data for growth during the slow cooling period before quench ($0.28°C/s$). The equilibrium and Scheil models are essentially equivalent for slow cooling, and fit the experimental data slightly better than the LDC model for the first 20 seconds of solidification.

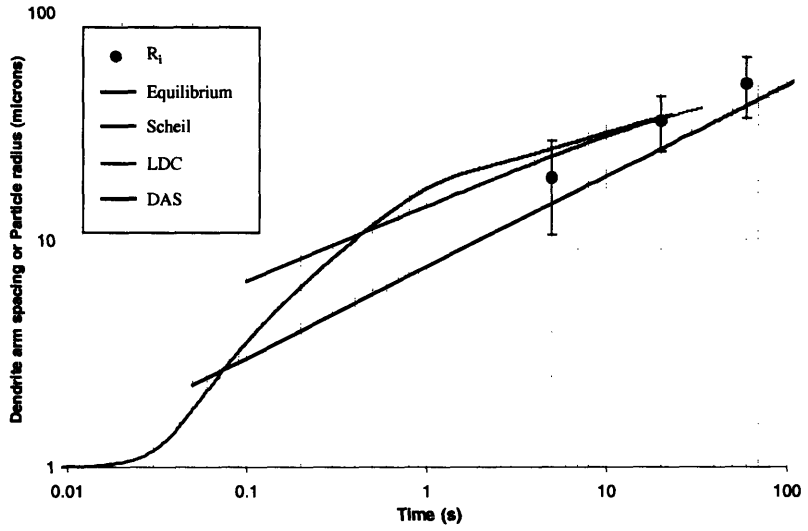

Figure 5-9: Comparison of experimental measurements of particle size in rheocast Al-4.5wt%Cu with the predicted size evolution given by the three particle growth models for the case of slow cooling ($0.28°C/s$).

Solute content within a spheroidal particle

For the case of alloy cooled slowly at $0.28°C/s$ then quenched at $375°C/s$ when the particle radius is 20 μm, Figure 5-10 compares the solute content predicted by the three growth models with microprobe measurements. All models predict the copper concentration within the particle to be about 1 $wt\%Cu$ for radial distance less than 20 μm. At this particle size, the cooling rate in the experiment and in the models was increased to $\backsim 375°C/s$ and only the LDC model continues to follow the experimental trend in particle solute content. For the case of fast cooling, the LDC model is appropriate and the equilibrium and Scheil models are not.

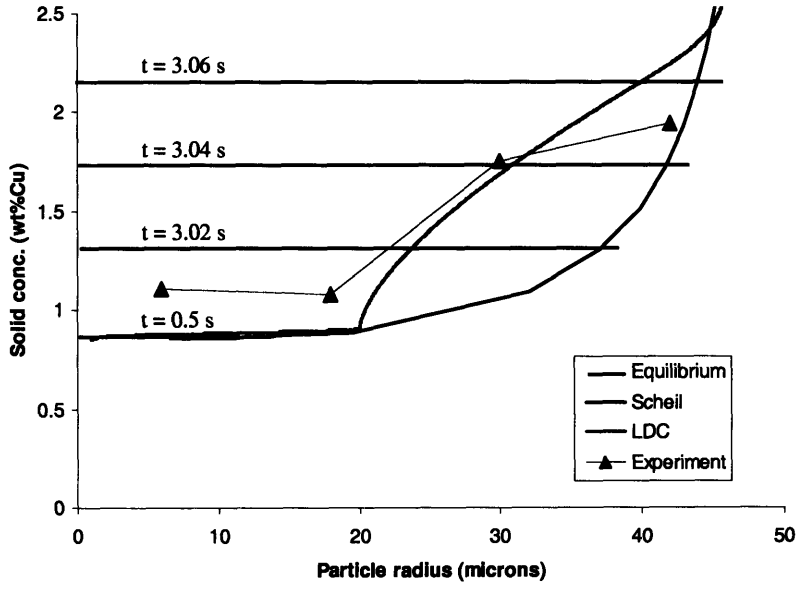

Figure 5-10: Comparison of microprobe measurements of particle solute content with predicted values given by the three particle growth models for the case of slow cooling ($0.28°C/s$) followed by fast cooling ($375°C/s$).

Particle Stability

Recall that the measured radius R_i in the rheocast alloy characterized the particle growth prior to quench, and R_f was the final particle radius including the growth which occurred during the quench. The average particle growth velocity, V_{avg}, for growth up to the measured R_i radii was estimated by dividing R_i by the total time the alloy was below the liquidus temperature before quench, t_s:

$$V_{avg} = \frac{R_i}{t_s} \tag{5.4}$$

Using Equation 5.4, the measured particle radii and estimated growth velocities were plotted on the standard stability criterion curve, shown in Figure 5-11. All points are close to the curve which separates the stable and unstable growth regions.

In order to estimate the amount of time it took for a particle to grow from its initial radius R_i to its final radius R_f (when it became unstable) the microprobe data was used in the expression:

$$\Delta t_u = \frac{m_S \Delta C_d}{\dot{T}} \tag{5.5}$$

where ΔC_d is the difference in solute content at radii R_f and R_i as determined by the microprobe, Δt_u is the duration of stable particle growth, m_s is the slope of the solidus, and $\dot{T}$ is the quench rate. Using Figure 5-7, ΔC_d is taken to be approximately 0.5 $wt\%Cu$. Assuming that the cooling rate for the alloy in the quench mold was about $375°C/s$ (Appendix D) and the alloy's solidus slope is $17.9°C/wt\%Cu$, the time it took for the particle to grow from radius R_i to radius R_f was calculated to be 0.024 seconds. Assuming Δt_u was roughly the same for all samples, the average growth velocity during the quench, V_{quench}, was approximated by

$$V_{quench} = \frac{(R_f - R_i)}{\Delta t_u} \tag{5.6}$$

The measured particle radii and estimated growth velocities during quench are plotted in Figure 5-11. All points are clearly in the unstable growth regime as defined by the criterion.

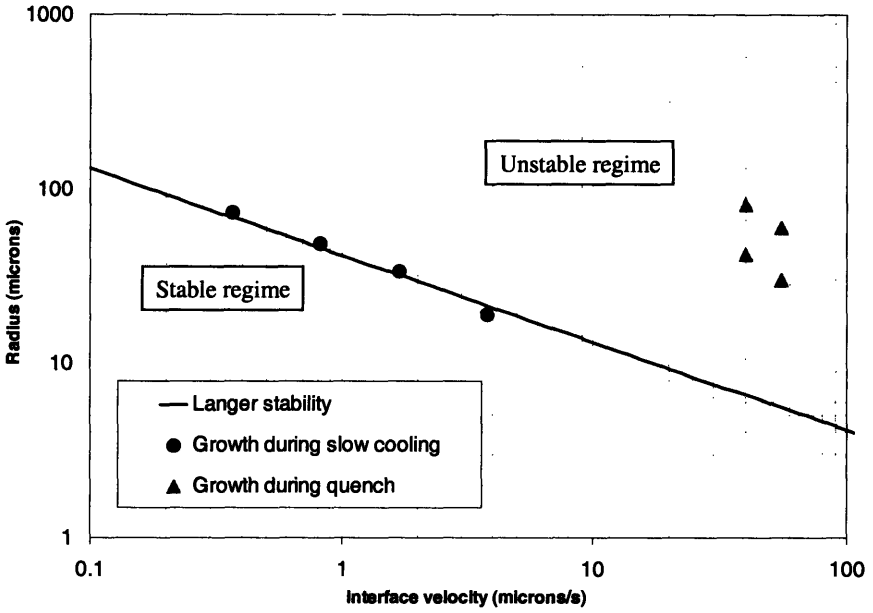

Figure 5-11: Comparison of experimental data for particle growth in Al-4.5wt%Cu during the "rheocast and quench" experiments with the interface stability criterion developed following the analysis of Langer.[53] The treatement assumed a single particle solidifying in an infinite amount of liquid.

5.4 Particle Interface Stability Experiments

5.4.1 Procedures

Experiments were performed to determine the effect of cooling rate on the interface stability of spheroidal particles in rheocast Al-4.5wt%Cu alloy. Small samples of fully-solidified rheocast Al-4.5wt%Cu alloy were cut from an ingot. The microstructure of these samples was identical to the one shown in Figure 5-1(b). Each cylinder was roughly 1 *cm* in diameter, and 1.5 *cm* in height. A small hole, slightly larger than 1 *cm* in diameter and 1 *cm* deep was drilled in the top of each sample, along the cylinder's axis. A K-type thermocouple (0.1 *cm* dia.) was inserted in the hole to measure sample temperature. Samples were placed on a holder and inserted into a preheated furnace. They were reheated to three temperatures which corresponded to solid fractions of 0.25, 0.45, and 0.63 (approximated using the Scheil relation in Equation 3.9 and alloy data in Appendix B). For samples reheated to a solid fraction of 0.25, the metal was too fluid to hold its shape. These samples were held together during reheating by a thin-walled steel sleeve coated with boron nitride spray. The time to heat and equilibrate each samples at one of the three temperatures was always between 9 and 12 minutes.

After equilibrating at one of the three temperatures, the samples were cooled at various rates, ranging between 1 and 50 $°C/s$. Due to the small sample size, it was reasonable to expect that the entire sample was cooled at or near the measured cooling rate (see Appendix F). After each sample had solidified completely, it was polished and etched with Keller's reagent. The conditions for each of the interface stability experiment can be found in Appendix C, experiment #'s 14-27.

5.4.2 Microstructures

Between 5 and 10 micrographs were taken from each sample. The stability of the particles in samples cooled at the various rates was assessed qualitatively by looking at the final morphology of what had been the solid-liquid interface. Figure 5-12(a)-(d) shows the microstructure of samples reheated to a fraction solid of 0.61 and cooled at 3.5, 5.6, 11, and 50$°C/s$. The samples cooled at 3.5 and 5.6$°C/s$ show particle with stable interfaces. The microstructures in Figures 5-12(c) and (d) show unstable particle interfaces which resulted from cooling the

samples at 11 and 50°C/s.

Figures 5-13(a)-(e) show the microstructure of samples reheated to a fraction solid of 0.45 and cooled at 1.7, 2.9, 3.8, 10.5, and 40°C/s. Samples cooled at 1.7 and 2.9°C/s show mostly stable particle interfaces, and the higher cooling rates produced a majority of unstable particles.

Figures 5-14(a)-(e) show the microstructure of samples reheated to a fraction solid of 0.25 and cooled at 1.1, 2.8, 4.2, and 9.3°C/s. Only the sample cooled at the slowest speed of 1.1°C/s contains a majority of particles with stable interfaces.

Figure 5-15 is a summary of all the interface stability experiments conducted. The y-axis of the graph is solid fraction, and the x-axis is cooling rate, plotted on a logarithmic scale. Solid fraction-cooling rate combinations which produced samples with mostly stable or unstable particle interfaces are labeled. Figure 5-15 shows that samples with higher solid fraction were able to maintain stable particle interfaces at higher cooling rates than samples with lower solid fractions.

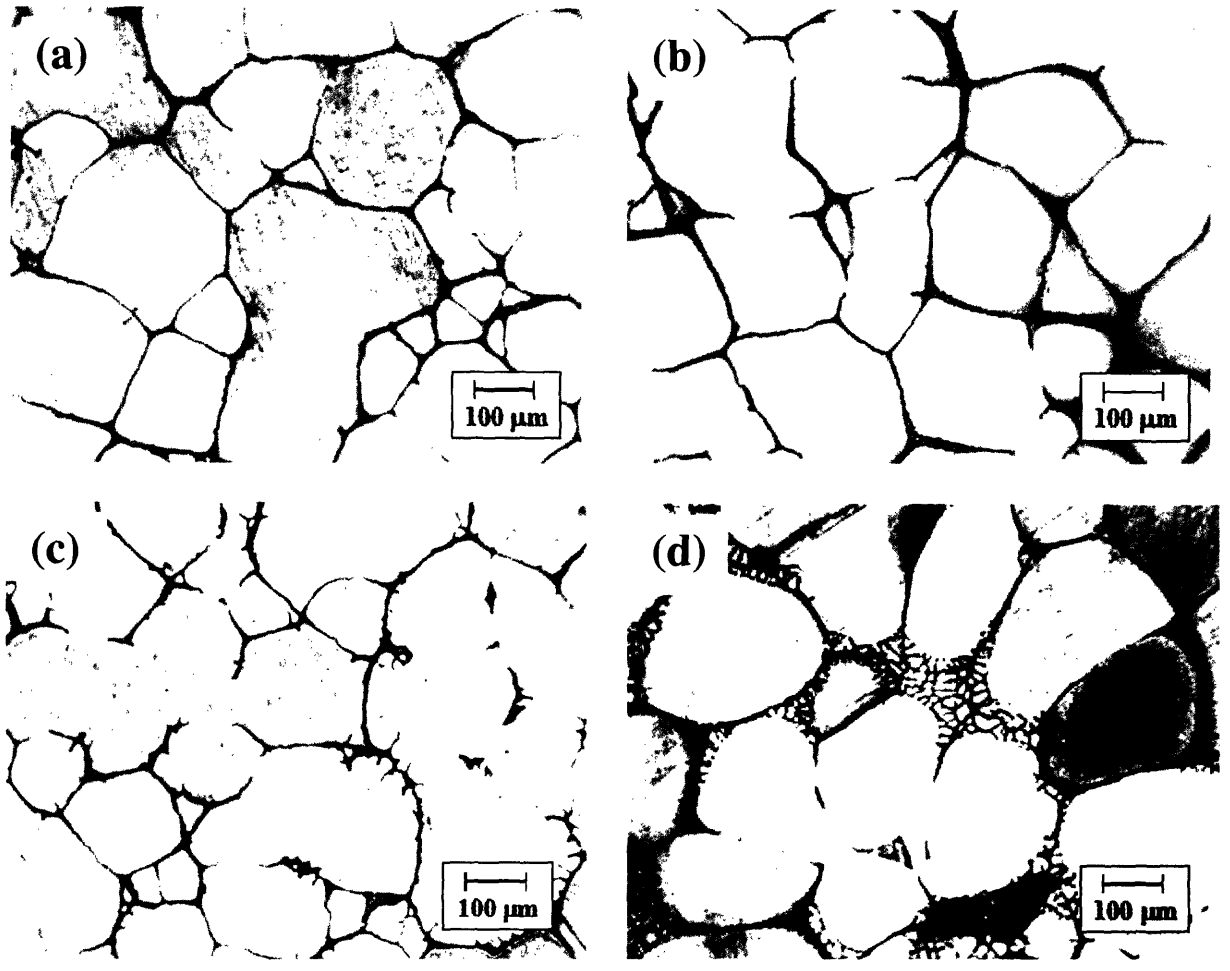

Figure 5-12: Microstructures of rheocast Al-4.5wt%Cu alloy reheated to a solid fraction of 0.61 and then cooled at (a) 3.5 (b) 5.6 (c) 11 (d) $50°C/s$.

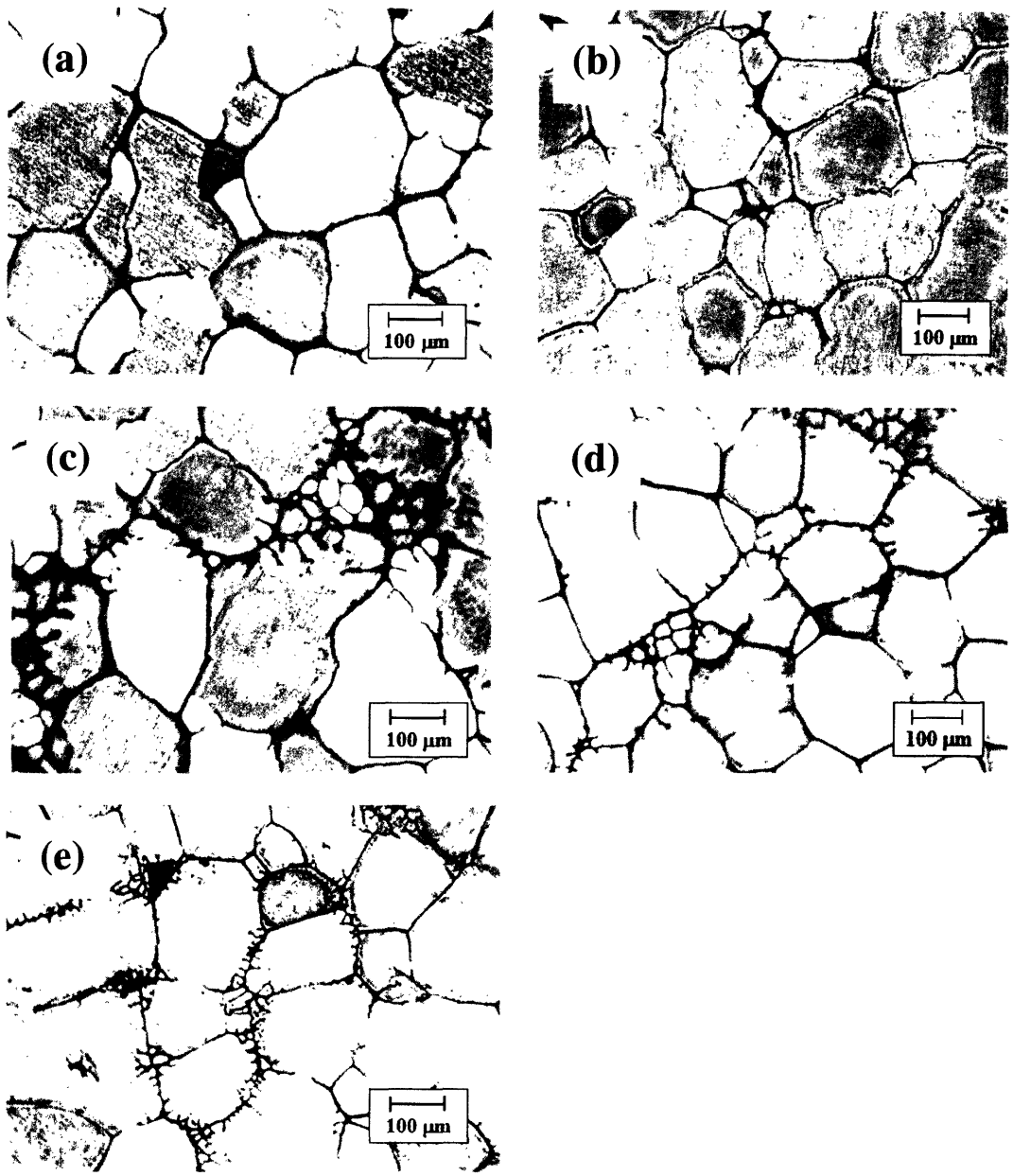

Figure 5-13: Microstructures of rheocast Al-4.5wt%Cu alloy reheated to a solid fraction of 0.45 and then cooled at (a) 1.7 (b) 2.9 (c) 3.8 (d) 10.5 (e) $40°C/s$.

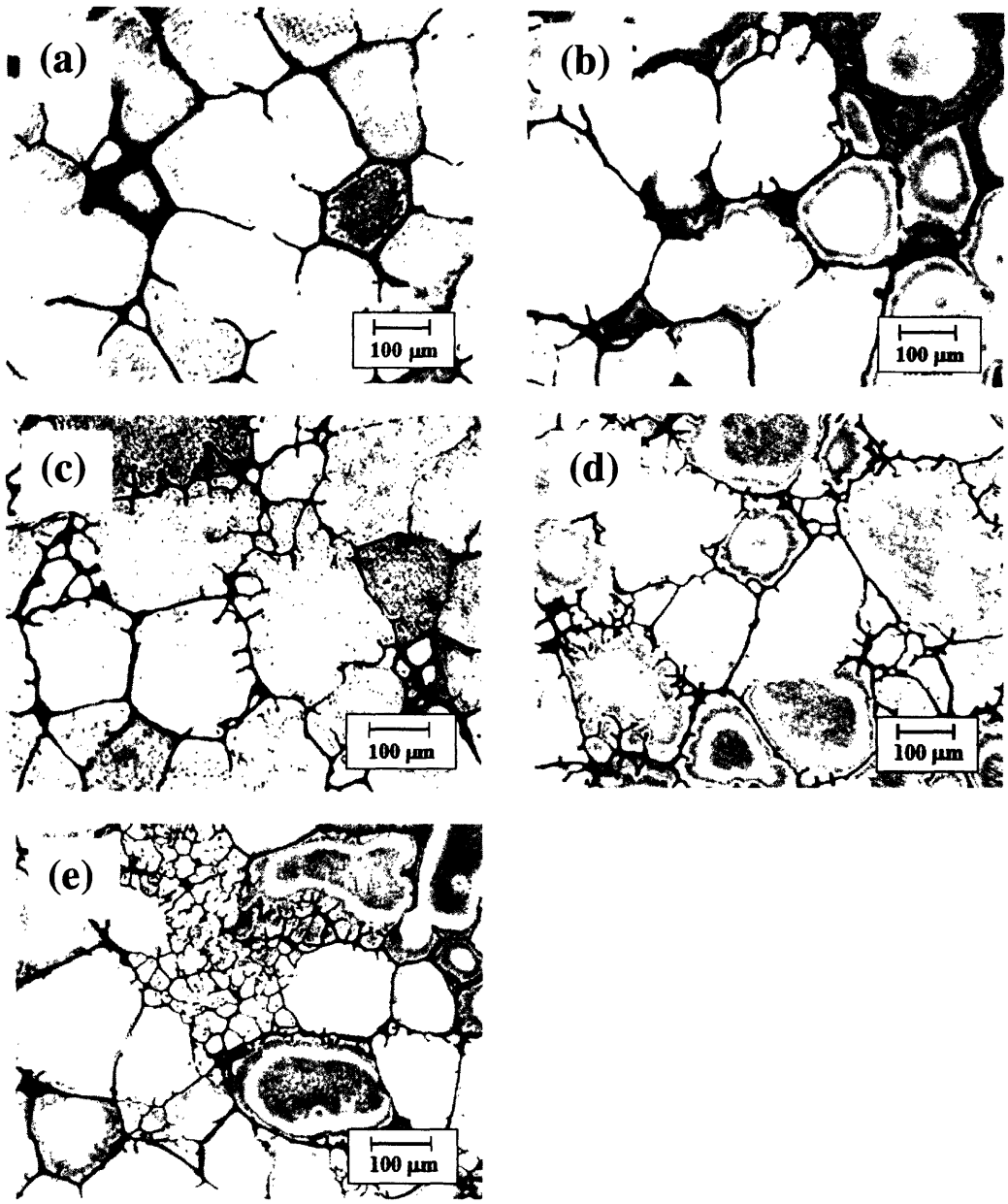

Figure 5-14: Microstructures of rheocast Al-4.5wt%Cu alloy reheated to a solid fraction of 0.25 and then cooled at (a) 1.1 (b) 2.8 (c) 4.2 (d) 9 (e) $38°C/s$.

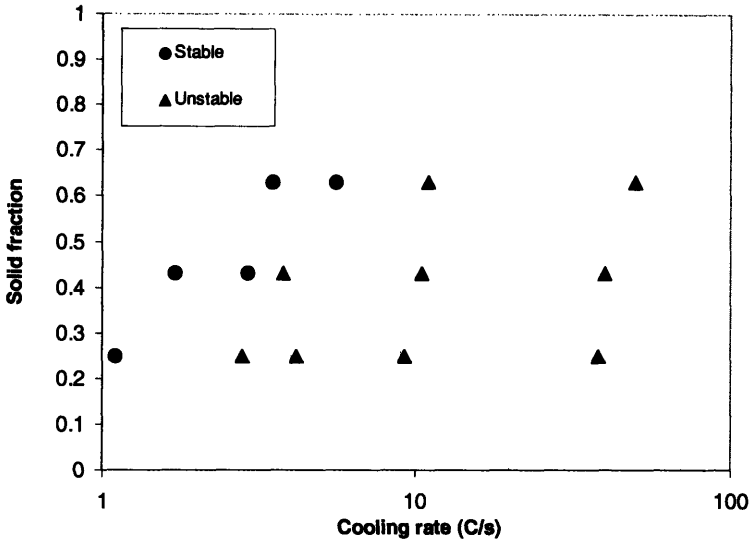

Figure 5-15: Summary of interface stability experiments with rheocast Al-4.5wt%Cu alloy showing which combinations of solid fraction and cooling rate allowed stable particle growth.

5.4.3 Data Comparison with Models

In the modeling section, Equation 3.29 was derived as a modified stability criterion for rheocast alloy providing a relationship between solid fraction and the maximum cooling rate which would maintain stable particle growth. In order to compare predicted and experimental data, an appropriate particle density estimate for the slurries used in the experiments was required. This was achieved by estimating the R_T for the experiments: approximating the average distance separating particle centers in the micrographs shown in Figures 5-12, 5-13, and 5-14, then dividing by two. An R_T of 150 μm was thus estimated. This R_T value was put into Equation 3.28 and a particle density of 70 particles/mm^3 was calculated. Note that the R_T of 150 μm measured for the interface stability experiments is noticeably larger than the R_T of 50 μm used to compare the particle growth models with experimental data. This is due to the significant ripening which occurred during the relatively long reheating time (about 9 minutes) required to reach the temperatures specified in the interface stability experiments.

Figure 5-16 compares the experimental interface stability data with the prediction given by Equation 3.29 using a pre-factor $C = 1.2$ and the estimated particle density of 70 particles/ mm^3. The modified interface stability theory described by Equation 3.29 fits the experimental data for reheated rheocast Al-4.5wt%Cu alloy very well.

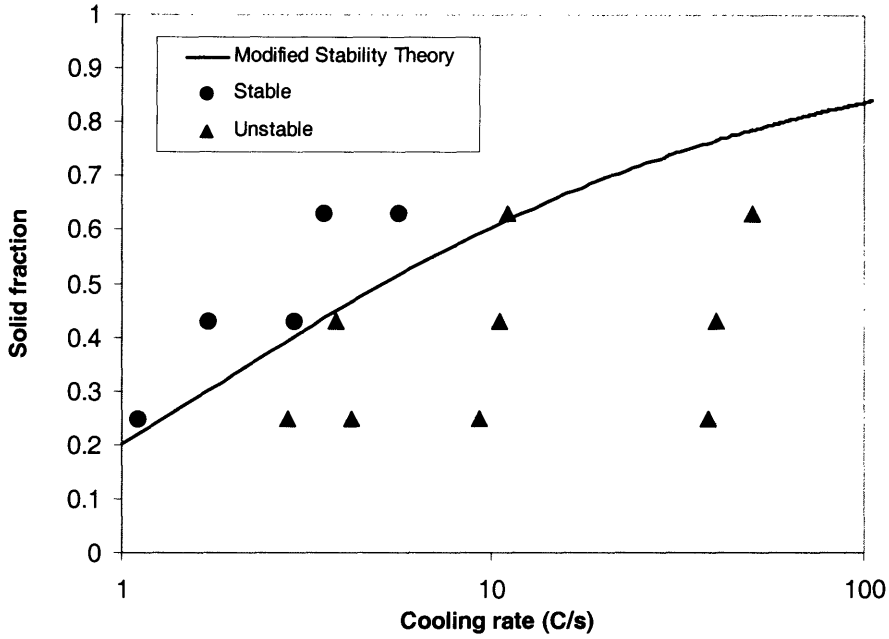

Figure 5-16: Comparison of modified interface stability theory with experimental data for rheocast Al-4.5wt%Cu alloy. A particle density of about 70 particles/mm^3 was obtained from the experimental data and used in the modified stability theory.

5.5 Fluidity of A357 Alloy

5.5.1 Procedures

A series of experiments using $A357$ alloy was conducted to compare the flow behavior of rheocast semi-solid alloy with that of liquid metal. For each experiment requiring a rheocast slurry, the $A357$ alloy was held at $622°C$, roughly $5°C$ above the liquidus temperature. The rotating copper rod (409 *rpm*) was immersed into the melt, stirring and cooling the alloy below the liquidus temperature. When the rod cooled the alloy to temperatures corresponding to 15% and 37% solid (estimated using a Scheil relationship), the rheocast alloy was drawn into the quench mold with a ΔP of 200 *torr*. Using the same ΔP, liquid alloy, superheated 5 and $21°C$ above the liquidus temperature, was drawn into the quench mold. The weight of the metal that solidified in the quench mold, M_{Ch}, was measured. This weight was converted into an effective fluidity length, L_f, using the expression

$$L_f = \frac{M_{Ch}}{\rho W \delta} \tag{5.7}$$

where ρ is the alloy density, W is the sample width, and δ is the sample thickness.

The effect of ΔP on the fluidity length of rheocast alloy was also studied. Rheocast alloy with a solid content of 37% was drawn into the channel with a ΔP of 400, and 560 *torr*. All relevant experimental parameters can be found in Appendix C, experiment #'s 28-39.

The amount of metal that could be drawn into the quench molds was dependent on the cooling rate in the quench molds. Assuming interface-controlled heat transfer, the cooling rate of the metal in the mold would be heavily influenced by the characteristics of the thin graphite coating applied to the interior of each mold. Hence, extreme care was taken to coat the quench molds used in the fluidity study as uniformly as possible. Two identical tests for each experiment described were performed to verify that unintentional variations in the graphite coating did not cause major differences in the measured fluidity lengths.

5.5.2 Fluidity Plots

Figure 5-17 shows the fluidity data for the $A357$ alloy drawn into the quench molds at temperatures both above and below the liquidus. The data points for the rheocast alloy are labeled

with the estimated solid content at the time of quench. The fluidity of superheated liquid values are slightly higher than that of the rheocast alloy with 15% solid particles, and about twice that of the alloy with 37% solid particles. Recall that Flemings *et al.* calculated that if Al-4.5wt%Cu alloy solidified dendritically, the metal would cease to flow when the flow tip reached 35% solid.[61] Therefore, the fluidity of the slurry with 37% solid phase is significant, and proof of the unique rheological properties that arise from a non-dendritic microstructure.

Another important feature of Figure 5-17 is that it shows there is no discontinuity in fluidity as temperatures go from above to below the liquidus. The slope of the trend line becomes slightly steeper after the temperature drops below the liquidus. This finding is consistent with results reported by Nafisi *et al.* in their study using rheocast A356 alloy.[64]

Figure 5-18 shows how the fluidity of rheocast alloy with 37% solid particles increases with an increasing ΔP to drive the flow. A linear trend line adequately describes the relationship between fluidity length and ΔP for the metal slurry.

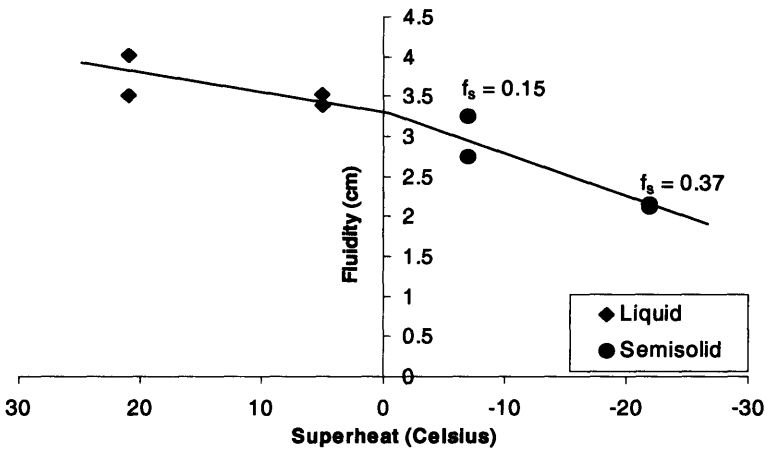

Figure 5-17: Effective fluidity of A357 alloy slurries compared with superheated liquid. Temperatures above the liquidus temperature ($617°C$) are considered positive.

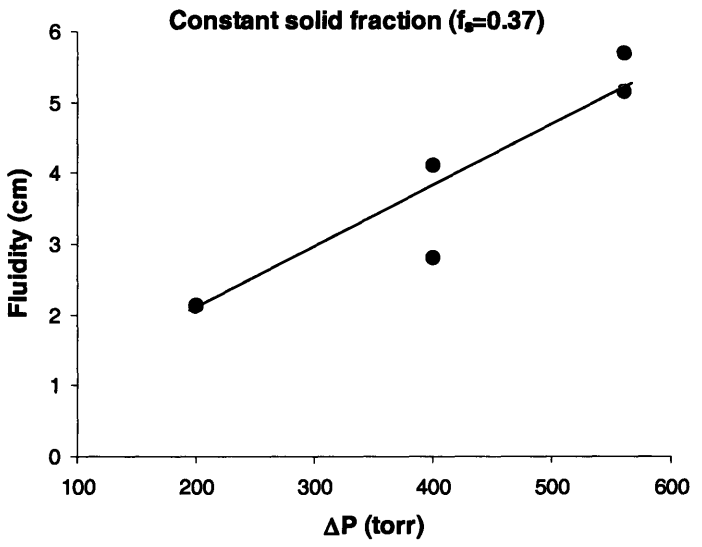

Figure 5-18: Effective fluidity of semi-solid A357 alloy with a solid content 37% as a function of the driving force for flow ΔP.

Chapter 6

Discussion

6.1 Obtaining a Spheroidal Structure by Ripening of Dendrites

In this work, the rapidly solidified fine equiaxed structure (Figure 5-3(a)) promptly ripened to one possessing spheroids when it was re-heated into the solid-liquid temperature range. The dependence of spheroid size on solidification time was shown in Figure 5-5 to follow closely the classic ripening plot for dendritic Al-4.5wt%Cu. The measured spheroid radii actually lie slightly above the ripening curve, which might be expected as a result of the additional curvature of these spheroids when compared with dendrite arms.

In commercial semi-solid forming practice today, the initial number of grain "nuclei" is insufficient for direct spheroidal growth. The initial grains continue to grow dendritically, with the desired spheroidal structure obtained by subsequent ripening. This sequence is shown schematically in Figure 6-1 by the paths (a)-(e) . Each tiny equiaxed particle grows into a larger equiaxed dendrite, then ripens into a "rosette", and later into a larger spheroid. Liquid is entrapped in the regions between the rosette arms during the ripening process, resulting in the final spheroid containing entrapped eutectic. If the equiaxed dendrites in Figure 6-1(b) grow to be very large, ripening proceeds along the path (b)-(b_2), and the final structure is one of deformed dendrites. The grain structure retains something of a dendritic outline with large pockets of entrapped eutectic.

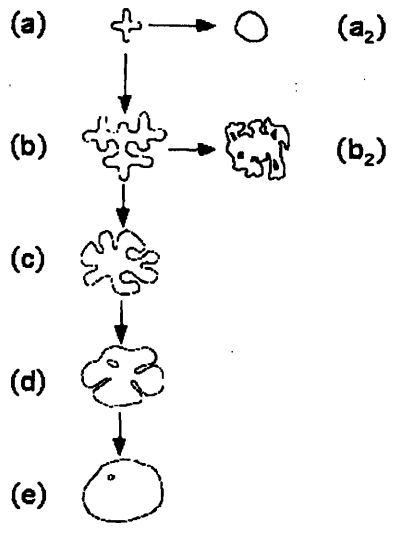

Figure 6-1: Paths by which solid particles can develop into rosettes or spheroids.[3]

The reheating experiments performed in this study point to what should perhaps be intuitive: to obtain spheroidal particles by reheating equiaxed dendrites of given initial size, one must hold the alloy in the solid-liquid temperature range for approximately the time it takes for dendrite arm spacing to reach a length scale equal to the initial grain size. For example, it was shown in Figure 5-3(a) and (b) that spheroidal particles of about 10 μm radius were obtained from initially equiaxed dendrites of 10 μm radius by reheating above the eutectic for 5 seconds, the same time given by the classic ripening curve for dendrite arms in dendritic alloy to space themselves 10 μm apart. Using the ripening curve in this manner provides a way for foundries to estimate the time it would take for non-dendritic structures to form by reheating of equiaxed dendrites of given size. However, the finest grain size obtained in usual grain refined aluminum castings is about 100 μm, typically around 200 μm.[70],[71] The time required to fully spheroidize such a grain size would be about 1.5 hours - a time too long to be industrially practical.

Achieving spheroidal structures by ripening of equiaxed dendrites usually results in some entrapped eutectic. Even in the case of the very fine dendrites used in this study, some entrapped eutectic is present in the ripened structures, and substantially greater amounts of

eutectic is typically seen when coarse grains are ripened.

6.2 Direct Formation of the Spheroidal Structure

In the experimental work presented in this study, the rheocast structure obtained by processing liquid alloy was "trapped" by rapid quench at the earliest time possible in the solidification process: approximately 5 seconds. Events occurring somewhat earlier than this time could be inferred from the traces of microsegregation found in the quenched spheroids (lighter shaded spheroidal centers), but the experiments shed no direct light at all on the earliest stages of morphological changes during the solidification process in rheocast alloy. This section comprises conjecture about those initial stages, based on available analyses and experimental results.

Solidification begins with a small particle, as sketched in Figure 6-1(a). This "pre-dendrite" might have come from a nucleation event (i.e. heterogeneous nucleation on a grain refining agent) or from "breaking off" of arms from a "mother dendrite".

The fragility of the mother dendrite produced in the rheocast experiments may be estimated in several ways. Assuming (1) heat flow into the copper chill to be interface controlled, (2) the mother dendrites are growing radially from the chill, and (3) the full volumetric heat of fusion of aluminum is removed for each increment of growth of the dendrite tip, the rate of solidification, R_s, is:

$$R_s = \frac{h\Delta T}{\rho \Delta H} \tag{6.1}$$

where h is the heat transfer coefficient for the rod-melt interface, ΔT is the temperature difference between the rod and melt, ρ is the alloy density, and ΔH is the heat of fusion of pure aluminum. Using the h, ΔT , and ΔH values given in Appendix D for the rod-melt interface, the rate of solidification in the rheocasting experiments is estimated by Equation 6.1 to be slightly greater than 1 mm/s. This estimate is a conservative dendrite tip velocity for the aluminum alloy due to assumption (3) above. Taking 1 mm/s as the dendrite tip velocity, and using the estimate of Kurz for the relationship between dendrite growth velocity and tip radius [72], Figure 6-2 shows that the corresponding tip radius would be approximately 1 μm.

Of course, during the rheocasting experiments, one might imagine that the "mother den-

drites" do not grow radially from the chill, but rather nucleate in the supercooled liquid adjacent to the rotating chill. In this case, an initial supercooling of about $5°C$ (a reasonable amount for aluminum alloy) would result in a similar dendrite tip radius of 1 μm, as shown by Figure 6-3. An undercooling of about this amount may be suggested by the somewhat elevated copper concentrations at the center of particles in quenched rheocast alloy, shown in the microprobe data plotted in Figure 5-7. These elevated copper concentration may be the remnants of what was a substantial solute concentration difference at the time the solid comprising the particle center was forming in the undercooled liquid. It is expected that solid diffusion would significantly reduce these concentration differences during subsequent solidification, leaving only the slightly elevated copper concentrations to be measured by the microprobe.

Starting with "mother dendrites" growing with initial tip velocity of 1 mm/s, one can envision two possibilities. In quiescent liquid, solidification of these mother-dendrites would proceed without dendrite breakup, while ripening of the initial dendrite arms proceeds. Final structure would be columnar or equiaxed dendrites. Vigorous stirring, on the other hand, combined with the rapid dendritic growth results in grain multiplication and enhanced arm "melt off" through thermal and/or mechanical influences on the mother dendrite, and then carrying arms and fragments that detach from the mother dendrite into the bulk melt. The small time required for fine dendrite arms (1 μm dendrite tip radius) to melt off is illustrated using the ripening calculation given by Kattamis [44]:

$$t_{crit} \backsim 0.0085 \frac{\rho \Delta H C_0 m_L (1-k) d^3}{\sigma D_L T} \tag{6.2}$$

where t_{crit} is the time required for a dendrite arm to "melt off", ΔH is the latent heat of fusion, σ is the solid-liquid interfacial energy, and d is the dendrite arm spacing. The temperature in the solid-liquid temperature range, T, is given in degrees Celsius. Assuming that the dendrite arm spacing is about twice the tip radius, in this case 2 μm, and that the temperature is just below the liquidus ($649°C$), the critical time for the arms to detach is approximately 0.01 seconds. Regardless of the particle generation mechanism, it is clear that when the generation of pre-dendrites from the mother dendrite is sufficiently large, particles grow spheroidally following the path (a)-(a_2) in Figure 6-1. Particle stability during growth is discussed in a later section.

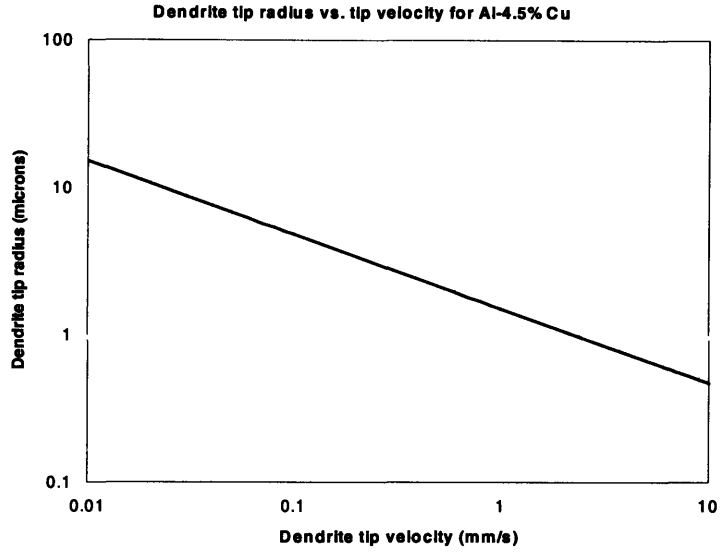

Figure 6-2: Relationship between dendrite tip radius and tip velocity for Al-4.5wt%Cu. Estimated using approximation given by Kurz and Fisher.[71]

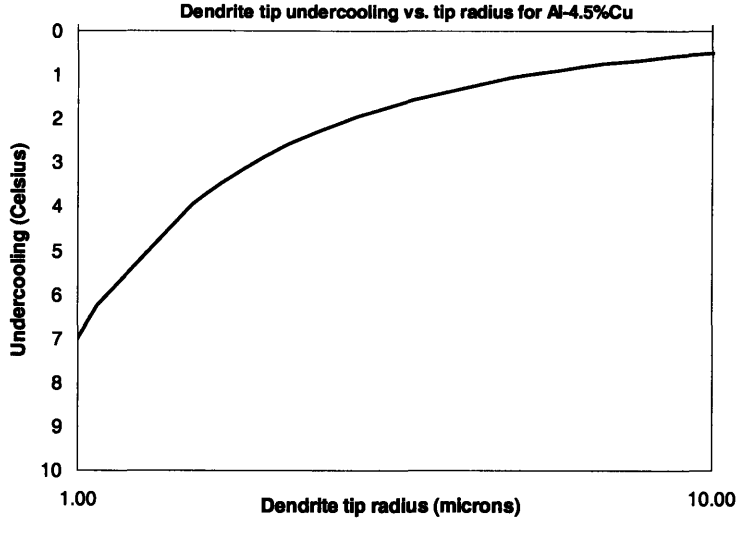

Figure 6-3: Relationship between undercooling and dendrite tip radius and tip velocity for Al-4.5wt%Cu. Estimated using approximation given by Kurz and Fisher.[71]

6.3 Particle Evolution

6.3.1 Particle Growth Models

The predicted relationship between average particle radius and time for the three growth models was compared with the average particle radius measurements taken from rheocasting experiments in Figure 5-9. For slow cooling ($0.28°C/s$), the equilibrium or Scheil solidification models have a slightly better fit to the experimental results for growth up to about 20 μm radius.

When a developed particle of roughly 20 μm radius was quenched at an approximated rate of $375°C/s$, only the LDC model follows the experimental measurements of particle solute content, Figure 5-10. Thus, the LDC model is found to be the best description of particle growth for the case of a well developed particle (some tens of micrometers in radius) exposed to a sudden increase in cooling rate. This scenario is analogous to a semi-solid forming operation, where a metal slurry with well developed spheroids is either cooled quickly to a desired fraction solid before injection into a die or is cast directly into a die.

6.3.2 Ripening

In the particle growth models, a constant particle spacing of 100 μm was assumed. The R_T value was assumed to be half of the particle spacing: 50 μm. This R_T value was assumed constant in each particle growth model. Ripening effects are inherently ignored by assuming a constant R_T value, since ripening ensures that smaller particles will melt and an equal amount of solid will redeposit on larger particles. The decreasing particle density due to ripening implies a changing inter-particle spacing R_T over time. Therefore, all three particle growth models presented did not consider the effects of ripening. For periods of fast cooling of relatively large spheres, ignoring ripening is easily justified. The solidification rate is sufficiently fast that the ripening rate of the existing spheroids is low in comparison. However, to model the slow cooling (or heating) of spheroids, ripening must be significant. This work has shown that the particles size in both the rheocasting and reheating experiments closely follow a classical ripening curve, Figures 5-5 and 5-9.

The issue of why the particle growth models, which ignore ripening, and the classic ripening curve work to estimate particle size evolution was addressed in the analysis of Ratke and

Beckermann.[73] Their analysis treated concurrent growth and ripening of spheres for three cases: pure growth of a spherical particle due to heat extraction, pure ripening, and then a combination growth and ripening. In all cases, the particles were found to increase in size with the cube root of time.

Ripening also affects solute distribution, a topic analyzed by Mortensen and others.[74]–[76] Because equilibrium at the solid-liquid interface is always maintained, as the temperature decreases during cooling the solid which is melting due to ripening will redeposit will with slightly richer solute concentration. Comparing solute content measured by the microprobe with model predictions which ignored any effect of ripening, Figure 5-10, the slightly higher solute concentrations measured within the particles may be due in part to this effect of ripening.

6.4 Particle Stability

In a semi-solid forming operation, once a slurry with a low solid fraction of spheroidal particles is obtained, it is usually cooled to increase the solid fraction to the desired level for forming. The cooling must be slow enough to retain the spheroidal particle morphology. During the forming step, the slurry is injected into a die and flows through gates and runners into the mold. If the cooling rate during either of these steps is rapid enough to destabilize the spheroidal solid-liquid interface of the particles, dendritic growth can occur; the flow properties of the slurry will deteriorate, and improper or erratic die filling can result.

A modified stability theory for particles in rheocast alloy was given in Equation 3.29, predicting the relationship between solid fraction and the maximum cooling rate which maintains particle stability. Using $C = 1.2$ and a particle density of 70 particles/mm^3 (a number obtained from measuring experimental microstructures), Figure 5-16 showed that Equation 3.29 had very good agreement with the experimental results obtained in this study using rheocast Al-4.5wt%Cu alloy.

The analysis that led to Equation 3.29 was based on determining the time it takes for solute fields surrounding particle neighbors to overlap. Since solute field overlap is a function of the interparticle spacing, the modified stability criterion given in Equation 3.29 is sensitive to the particle density in a metal slurry. Figure 3-19 showed the effect of particle density on the solid

fraction-maximum cooling rate relationship given by the model. At a given solid fraction, a slurry with a higher particle density will maintain particle stability at a higher cooling rate than a slurry with a lower particle density. At fixed particle density, a slurry with a higher solid fraction maintains particle stability at higher cooling rates than a slurry with a lower solid fraction. This indicates that the most robust rheocasting process are those that can create the highest particle densities, and that there is a potential benefit to make parts from slurries with high solid fractions.

Figure 3-19 is particularly powerful when used in tandem with the ripening curve to estimate average particle radius. The foundryman can easily measure slurry temperature and, using a Scheil approximation, estimate solid content, f_s. If the total time the metal slurry remains in the solid-liquid temperature range is known, the ripening curve shown in Figure 5-5 allows estimation of the average particle size, R. With f_s and R known, the particle density, N, can be estimated using the following two equations:

$$R_T = \frac{R}{\sqrt[3]{f_s}} \tag{6.3}$$

and

$$N = \frac{1}{\frac{4}{3}\pi \left(R_T\right)^3} \tag{6.4}$$

With a particle density estimate, the foundryman can then refer to the corresponding curve in Figure 3-19 to determine the maximum cooling rate for the slurry of given solid fraction to retain the spheroidal particle morphology during forming. If the cooling rate of the slurry is always below the critical value, the particles will always be spheroidal, and the flow behavior during forming is expected to be more predictable and consistent.

To apply this method, consider experiment #11 and 11a performed in this study (see Appendix C). An Al-4.5wt%Cu alloy with 0.18 solid fraction and average particle radius 35 μm was formed by rheocasting for 20 seconds. Using this data, Equations 6.3 and 6.4 give a particle density of roughly 1000 particles/mm^3. Solid fraction, particle density, and the appropriate parameters for the Al-4.5wt%Cu alloy (Appendix B) were put into the modified stability theory of Equation 3.29. Solving for cooling rate indicated that the slurry could have been cooled

about $8°C/s$ while still retaining the spheroidal structure. This surprisingly fast cooling rate is a result of the rheocasting process being effective at creating a high particle density. In a forming operation, cooling a slurry quickly to the desired forming temperature at a rate just below the $8°C/s$ limit could help reduce cycle time, resulting in increased productivity.

6.5 Fluidity

Figure 5-17 shows that there is no discontinuity in the fluidity of $A357$ alloy at the liquidus temperature when metal slurries are created by rheocasting. The slope of the fluidity trend line becomes slightly steeper after the temperature drops below the liquidus. Figure 5-17 also shows that the fluidity of rheocast $A357$ alloy with about 40% solid phase retains about half of the fluidity of liquid alloy which is superheated $20°C$ above the liquidus temperature. Starting with superheated liquid, Flemings *et al.* estimated that the flow of Al-4.5wt%Cu drawn into a tube would stop when 35% solid phase had formed at the flow tip. The $A357$ metal slurries in this study *started* with a solid content which exceeded this estimated limit, were drawn into a channel that was only 1 mm thick, and flowed about half the distance of liquid alloy superheated $20°C$. The influence of the spheroidal particle morphology on the alloy's ability to flow is clearly demonstrated by these experimental results.

Previous fluidity studies using liquid alloy have considered flow to be fully turbulent, and the fluidity length was shown to be proportional to the square root of ΔP.[57] In this fluidity study, the fluidity of $A357$ alloy slurry with 37% solid was shown to have a linear dependence on ΔP, Figure 5-18. The Reynolds number for the flow of liquid alloy with ΔP of 400 $torr$ was 2670 (Equation 4.1), indicating quasi-turbulent flow. However, a metal slurry with about 40% solid phase would have a much higher viscosity than liquid alloy, thereby making laminar flow more reasonable. Additionally, the metal slurries were drawn with a lower ΔP of 200 $torr$, so flow is expected to have been slower than when measured using a ΔP of 400 $torr$. Due to these factors, the Reynold's number for the flow of the rheocast slurry may have been significantly lower than 2670, perhaps even lower than 2100, making laminar flow conceivable. The linear dependence of fluidity on ΔP observed in this study of metal slurries may be a result of laminar slurry flow instead of turbulent liquid flow.

Chapter 7

Conclusions

7.1 Preface

This research shed important new light on the formation of rheocast structures. It shows qualitatively how much time is required for an initially equiaxed grain to ripen sufficiently into a spheroid. It shows that vigorous agitation, combined with rapid cooling, can avoid dendrite formation all together, and lead directly to spheroidal grains during just the first small amount of solidification (certainly less than 5% solidified). Agitation thereafter is unnecessary. The criticality of the region of localized rapid solidification supports the belief that dendrite break up is the source of the large number of particles that form and grow spheroidally, the size of the initial fragments being probably less than one micrometer.

7.2 Summary of Findings

- A unique experimental setup comprising a furnace, copper stirring rod, and thin-channel quench mold was designed, built, and employed to study the evolution of rheocast Al-4.5wt%Cu alloy microstructures and the fluidity of *A*357 alloy rheocast slurries and superheated liquid.

- Equiaxed dendrites, roughly 10 μm in radius and with a dendrite arm spacing of about 5 μm, were reheated above the eutectic temperature for various times. The equiaxed dendrites ripened into spheroids with entrapped eutectic within 5 seconds. Etching

showed traces of the original dendritic structure.

- A rheocasting process, combining rapid cooling in a localized region and vigorous convection to induce solidification, generated spheroidal particles in very short times. Rheocast Al-4.5wt%Cu alloy was quenched after it had been below the liquidus temperature for as little as 5 seconds. The micrographs showed that spheroidal particles free of entrapped eutectic had formed in this short time. Etching showed spheroidal particle centers. No trace of a previous dendritic structure was evident.

- It was not possible in this work to determine the mechanism of particle generation during rheocasting due to the very short times necessary for the particles to spheroidize (less than 5 seconds). It is speculated that the rapid cooling creates extremely fine and fragile "mother dendrites" which possess finely spaced secondary arms. A simple ripening model for detachment of finely spaced dendrite arms was used to show how a very small time is needed to generate particles that can then be swept into the bulk liquid if stirring is vigorous.

- Due to the morphological differences in spheroidal particles formed by rheocasting compared with those formed by reheating equiaxed dendrites of 10 μm radius - the lack of entrapped eutectic and dendritic traces revealed by etching - it is clear that the rheocasting process used created dendrite fragments or tiny equiaxed dendrites that must have been smaller than 10 μm in radius.

- There appear to be two processing routes to create spheroidal particles in semi-solid alloy, and the path taken depends on the particle density. If the initial particle density in a metal slurry is large, the particles, if not originally spheroidal, will ripen rapidly into spheroids. The remainder of growth is in the spheroidal morphology and the final structure will be without entrapped eutectic. If the particle density is low, equiaxed dendrites form, and become spheroidal after ripening (this time to become spheroidal is dependent on how large they have grown). If equiaxed dendrites form, the spheroidal structure from which it evolves will apparently always having entrapped eutectic in the final structure.

- For experiments conducted with Al-4.5wt%Cu alloy, the average radius of the spheroidal particles formed by either reheated dendritic alloy or rheocasting grew is size with increasing solidification time at a rate that closely follows the classical ripening curve for dendrite arm spacing. Whether coming down through the liquidus temperature during rheocasting, or coming up through the eutectic temperature during reheating, the time an alloy remains in the solid-liquid temperature range is the most important variable in determining spheroidal particle size. This finding provides an easy way for aluminum foundrymen to estimate the particle size in a metal slurry.

- Experimental evidence suggests that to obtain a spheroidal structure from an initially equiaxed dendritic structure of a given grain size, one must hold the alloy in the solid-liquid temperature range for the time required for dendrite arms to reach the initial equiaxed grain size, as given by the classic dendrite ripening curve.

- When slow cooling ($0.28°C/s$) was followed by fast cooling ($375°C/s$), only the LDC model followed the measured trend in solute content within particles for growth during the quench. The LDC model was considered to be the most applicable to particle growth during fast cooling because it considered the pile up of solute near the solid-liquid interface during rapid solidification.

- For Al-4.5wt%Cu alloy, a standard model for the interface stability of a single particle growing in an infinite liquid phase surrounding was presented. Experimental estimates of growth velocity combined with measured particle radii for slow cooling ($0.28°C/s$) produced points that were in the stable region defined by the standard stability model, which was consistent with experimental observation of particle growth during slow cooling. Estimates for growth during fast cooling ($375°C/s$) produced points in the unstable region defined by standard stability model, which was also consistent with experimental observations.

- A modified particle stability theory for rheocast Al-4.5wt%Cu alloy was developed to predict the relationship between solid fraction and the maximum cooling rate for particle stability. The theory considered solute field interaction between neighboring particles

and the influence it had on interface stability. The modified stability theory required knowledge of the particle density.

- Rheocast Al-4.5wt%Cu alloy was reheated slowly to three different temperatures and solid fractions and then cooling at various rates. Microstructures were analyzed to assess particle stability at each solid fraction-cooling rate combination. Using a particle density estimate obtained from the experimental data, the modified stability theory prediction of maximum cooling rate as a function of solid fraction had excellent agreement with the experimental results. Both experiment and theory showed that metal slurries with higher solid fraction were able to maintain stability at higher cooling rates than particles in slurries with lower solid fraction.

- The modified stability theory for rheocast alloy showed that the relationship between solid fraction and maximum cooling rate is sensitive to particle density. At a given solid fraction, a slurry with a higher particle density will maintain particle stability at higher cooling rates than a slurry with a lower particle density.

- A foundry method to ensure that particles in a rheocast metal slurry do not become unstable during a forming operation was proposed. The classic ripening curve is used to estimate particle size in rheocast alloy, provided that the time the rheocast alloy has remained in the solid-liquid temperature range is known. Slurry temperature is used to estimate solid fraction (Scheil relationship). Using the particle radius and solid fraction estimates, the particle density in a slurry can be approximated. The modified stability theory for rheocast alloy is then used to predict the maximum cooling rate allowable for a metal slurry of given solid fraction and particle density.

- If a high particle density is obtained by an effective rheocasting process, the modified stability theory indicates that subsequent cooling rates can be quite fast without the risk of particles in the slurry re-developing a dendritic morphology. For example, starting with a slurry with 0.2 solid fraction and particles of radius 35 μm, subsequent cooling rate can be in excess of $8°C/s$ while retaining the spheroidal structure. This indication has great practical relevance: semi-solid casting cycle times may be reduced by cooling a slurry to the forming temperature at a rate just below this limit.

- It was shown that rheocast $A357$ alloy with 37% solid content would flow into a thin, 1 mm channel roughly half as far as liquid alloy superheated $20°C$ above the liquidus. The influence of the spheroidal particle morphology on the flow of partially solidified alloy was clearly demonstrated by these experimental results.

- There is no discontinuity in fluidity at the liquidus temperature when comparing superheated liquid and rheocast alloy $A357$ alloy. Instead, it was found that the slope of the fluidity trend line becomes slightly steeper at temperatures below the alloy's liquidus temperature.

- The fluidity length of $A357$ alloy with 37% solid was shown to have a linear dependence on the pressure drop driving the flow, ΔP. It was speculated that this linear relationship is an indication that the flow of slurry in the quench mold was laminar.

Chapter 8

Suggested Future Work

This study has investigated the generation, growth, stability, and fluidity of rheocast aluminum alloy. The following is a list of ways to continue this investigation:

- Repeating the rheocasting and quenching experiments with an alloy that will solidify with a smaller amount of primary solid may make it easier to identify particles generated at earlier times in the solidification process. Attempting to quench microstructures at even shorter solidification times during rheocasting may lead to more information about structural development and particle generation.

- A potentially insightful experimental study would be to determine the necessary ratio of grain size to dendrite arm spacing to form spheroidal particles with no entrapped eutectic from reheated equiaxed dendrites. Studying the time it takes for this spheroidization processes to complete with relatively large grain size-dendrite arm spacing ratios may show trends that can be extrapolated back to the earliest stages of solidification.

- Understanding the role of convection during rheocasting, and the intensity required, would aid in process control and development. Simple solidification experiments using "thermally invisible" grids or DC fields to control convection may be useful in determining the role of convection on the generation and/or escape of particles from the mushy zone of an alloy.

- Due to the difficulties in obtaining evidence regarding the mechanism of particle gen-

eration during rheocasting of liquid metal, experimental evidence might be obtained by performing rheocasting experiments with transparent analog systems under a microscope equipped with high-speed imaging capability.

- Computer modeling can be a powerful tool for understanding the rheocasting process. Growth models which consider mechanical, solutal, and thermal fields surrounding a particle solidifying in a vigorously stirred liquid may be a powerful way to observe very short times during the solidification process and expose dendrite fragmentation mechanisms that complete too rapidly for experimental study.

- The modified stability model, a potentially valuable tool for the semi-solid foundry, needs further experimental verification. A series of experiments designed to vary particle density, particle size, solid fraction, and cooling rate is necessary to further validate the model. It is recommended that this study be conducted using an alloy system where solid fraction is not as sensitive to temperature as in the Al-4.5wt%Cu system used in this study.

- Understanding the flow properties of non-dendritic metal slurries is basic to the success of semi-solid metal forming in industry. Fluidity is one of the simplest ways to study metal flow, yet only a handful of experimental fluidity studies using metal slurries have been performed. A comprehensive experimental study of the effects of solid fraction, particle size, and flow type on the fluidity of metal slurries would contribute a great deal to a practical understanding of their flow properties. This type of experimental study, could help validate and improve semi-solid metal flow models which attempt to incorporate the thixotropic nature of metal slurries.

Bibliography

[1] D.B. Spencer. Rheology of Liquid-Solid Mixtures of Lead Tin, Ph.D. Thesis, Professor M.C. Flemings advisor, Massachusetts Institute of Technology, Cambridge, MA, June 1971.

[2] Science and Technology of Semi-Solid Metal Processing, A. de Figueredo, ed., North American Die Casting Association, Rosemont, IL, 2001.

[3] M.C. Flemings, W.L. Johnson. High Viscosity Liquid and Semi-Solid Metal Casting: Processes and Products, plenary lecture, World Foundry Conference, KynogJu, Korea, Oct. 20-24, 2002.

[4] C. Vives. Elaboration of Semisolid Alloys by Means of New Electromagnetic Rheocasting Processes, Metallurgical Transactions B, (23b), April 1992, pgs 189-206.

[5] P. Kapranos *et al.* Near net shaping by semi-solid metal processing, Materials and Design, (21), 2000, pgs 387-394.

[6] Personal communication, Dr. Jim Yurko, Staff Metallurgist, IdraPrince, Inc., 670 Windcrest Dr., Holland, MI, Feb. 2004.

[7] R.A. Martinez. A New Technique for the Formation of Semisolid Structures, MS Thesis, Professor M.C. Flemings advisor, Massachusetts Institute of Technology, Cambridge, MA, June 2001.

[8] Proceedings of the 1st Int. Conf. on Semi-Solid Processing, Sophia-Antipolis, France, April 4-6, 1990.

[9] Proceedings of the 2nd Int. Conf. on the Processing of Semi-Solid Alloys and Composites, Cambridge, Massachusetts, June 10-12, 1992.

[10] Proceedings of the 3rd Int. Conf. on Processing of Semi-Solid Alloys and Composites, Tokyo, Japan, June 13-15, 1994.

[11] Proceedings of the 4th Int. Conf. on Semi-Solid Processing of Alloys and Composites, Sheffield, United Kingdom, June 19-21, 1996.

[12] Proceedings of the 5th Int. Conf. on Semi-Solid Processing of Alloys and Composites, Golden, Colorado, June 23-25, 1998.

[13] Proceedings of the 6th Int. Conf. on Semi-Solid Processing of Alloys and Composites, Turin, Italy, Sept. 27-29, 2000.

[14] Proceedings of the 7th Int. Conf. on Semi-Solid Processing of Alloys and Composites, Tsukuba, Japan, Sept. 25-27, 2002.

[15] P. Kapranos. Semi-Solid Metal Processing: an environmentally friendly process, Materials World, Sept. 2004, pgs. 465-467.

[16] S.P. Midson, K. Brissing. Semi-Solid Casting of Aluminum Alloys: A Status Report, Modern Casting, Feb. 1997, pgs. 41-43.

[17] M. Yamazaki *et al.* Development of a High-Strength Aluminum Cylinder Block for Diesel Engine Employing a New Production Process, SAE International, Publication 2004-01-1447.

[18] R. Decker *et al.* Advances in Semi-Solid Molding, Advanced Materials and Processes, ASM International, April 2004, pgs. 41-42.

[19] A. Rassili *et al.* Numerical Simulations and Experimental Investigations of the Semi-Solid Metal Processing of Steels, Proceedings of the 7th Int. Conf. on Semi-Solid Processing of Alloys and Composites, Tsukuba, Japan, Sept. 25-27, 2002, pgs 367-372.

[20] E. Lugscheider *et al.* Development, Investigation and Characterisation of New Surface Technologies for the use of Semi Solid Metal Forming of Steel, Proceedings of the 7th Int. Conf. on Semi-Solid Processing of Alloys and Composites, Tsukuba, Japan, Sept. 25-27, 2002, pgs 385-390.

[21] C.S. Rice, P.F. Mendez, S.B. Brown. Journal of Metals, (12), 2000, pgs 31.

[22] J. Valer *et al.* Microstructural and Mechanical Characterisation of an Al-21.8wt%Ge Brazing Alloy with a Globular Morphology of the Primary Al-rich Phase, Materials Science and Engineering A, (272), 1999, pgs 342-350.

[23] J. Valer *et al.* Microstructure and Semisolid Behavior of Al-Ge Alloys, Proceedings of the 5th Int. Conf. on Semi-Solid Processing of Alloys and Composites, Golden, Colorado, June 23-25, 1998, pgs 3-10.

[24] S. Ji, Z. Fan, M.J. Bevis. Semi-solid processing of engineering alloys by a twin-screw rheomoulding process, Materials Science and Engineering A, (299A), 2001, pgs 210-217.

[25] US Patent No. 5,555,926. Process for the Production of Semi-Solidified Metal Composition, Rheo-Technology, Ltd., Sept. 17, 1996.

[26] US Patent No. 5,983,978. Thermal Shock Reistant Apparatus for Molding Thixotropic Materials, Thixomat, Inc., Nov. 16, 1999.

[27] US Patent No. 5,887,640. Apparatus and Method for Semi-Solid Material Production, Semi-Solid Technologies Inc., Mar. 30, 1999.

[28] M. Kiuchi, S. Sugiyama. A New Process to Manufacture Semi-solid Alloys, ISIJ International, (35), No. 6, 1995, pgs 790-797.

[29] M. Findon, A.M. de Figueredo, D. Apelian, M.M. Makhlouf. Melt Mixing Approaches for the Formation of Thixotropic Semisolid Metal Structures, Proceedings of the 7th Int. Conf. on Semi-Solid Processing of Alloys and Composites, Tsukuba, Japan, Sept. 25-27, 2002, pgs 557-562.

[30] P. Mathur, D. Apelian, A. Lawley. Acta Metallurgica, (37), 1989, pgs 429-443.

[31] US Patent No. 6,165,411. Apparatus for Producing Metal to be Semimolten-Molded, UBE Industries, Ltd., Dec. 26, 2000.

[32] J.L. Jorstad, M. Thieman, R.Kamm. SLC, The Newest and Most Economical Approach to Semi-Solid Metal (SSM) Casting, Proceedings of the 7th Int. Conf. on Semi-Solid Processing of Alloys and Composites, Tsukuba, Japan, Sept. 25-27, 2002, pgs 701-706.

[33] R. Shibata *et al.* Formation of Spherical Solid Phase in Die Casting Shot Sleeve Without Any Agitation, Proceedings of the 5th Int. Conf. on Semi-Solid Processing of Alloys and Composites, Golden, Colorado, June 23-25, 1998, pgs 465-470.

[34] T. Haga, P. Kapranos. Simple Rheocasting Process, Journal of Materials Processing Technology, 130-131, 2002, pgs 594-598.

[35] SB Park, I. Stone, B. Cantor. Rheocasting of Aluminum Alloys, Proceedings of the Solidification of Aluminum Alloys Symposium, TMS Annual Meeting, Charlotte, NC, March 14-18, 2004, pgs 257-266.

[36] J.A. Yurko, R.A. Martinez, M.C. Flemings. Commercial Development of the Semi-Solid Rheocasting (SSR) Process, NADCA Transactions, 2003, Indianapolis, IN, Sept. 2003, Paper No. T03-062.

[37] M.C. Flemings. Behavior of Metal Alloys in the Semisolid State, Metallurgical Transactions B, (22b), June 1991, pgs 269-293.

[38] T.F. Bower, M.C. Flemings. Formation of the Chill Zone in Ingot Solidification, Transactions of the Metallurgical Society of AIME, (239), February, 1967, pgs 216-219.

[39] K.A. Jackson *et al.* On the Origin of the Equiaxed Zone in Castings, Transactions of the Metallurgical Society of AIME, (236), Feb. 1966, pgs 216-219.

[40] G.S. Cole, G.F. Bolling, the Importance of Natural Convection in Casting, Transactions of the Metallurgical Society of AIME, (233), 1965, pgs 1568-1572.

[41] H. Esaka *et al.* Origin of Equiaxed Grains and their Motion in the Liquid Phase, ISIJ International, (43), No. 9, 2003, pgs 1415-1420.

[42] A. Vogel, R.D. Doherty, B. Cantor. Proc. Conf. on Solidification and Casting of Metals, Sheffield, July 1977, metals Society, London, UK 1979.

[43] R.D. Doherty, H. Lee, E.A. Feest. Microstructure of Stir-cast Metals, Materials Science and Engineering, (65), 1984, pgs 181-189.

[44] T.Z. Kattamis, J.C. Coughlin, M.C. Flemings. Influence of Coarsening on Dendrite Arm Spacing of Aluminum-Copper alloys, Transactions of the Metallurgical Society of AIME, (239), Oct. 1967, pgs 1504-1511.

[45] H.K. Moon. Rheological Behavior and Microstructure of Ceramic Particulate/Aluminum Alloy Composites, Professor M.C. Flemings advisor, Massachusetts Institute of Technology, Cambridge, MA, Sept. 1990, pgs 24, 55-56.

[46] W.R. Loue, M. Suery. Microstructural evvolution during partial remelting of Al-Si7Mg alloys, Materials Science and Engineering A, (A203), 1995, pgs 1-13.

[47] J.W.K. van Boggelen, D.G. Eskin, L. Katgerman. First stages of grain coarsening in semi-solid Al-Cu alloys, Scripta Materialia, (49), 2003, pgs 717-722.

[48] T.Z. Kattamis, U.T. Holmberg, M.C. Flemings. Influence of Coarsening on Dendrite Arm Spacing and Grain Size of Magnesium-Zinc Alloy, Journal of the Institute of Metals, (95), 1967, pgs 343-347.

[49] M.E. Glicksman, KG. Wang, S.P. Marsh. Diffusional interactions among crystallites, (230), 2001, 318-327.

[50] K. Ichikawa *et al.* Grain Refinement in Al-Cu Binary Alloys by Rheocasting. Transactions of the Japan Institute of Metals, (26), No. 7, 1985, pgs 513-522.

[51] W.W. Mullins, R.F. Sekerka. Morphological Stability of a Particle Growing by Diffusion or Heat Flow, Journal of Applied Physics, (34), No. 2, 1963, pgs 323-329.

[52] W.W. Mullins, R.F. Sekerka. Stabillity of a Planar Interface During Solidification of a Dilute Binary Alloy, Journal of Applied Physics, (35), No. 2, 1964, pgs 444-451.

[53] J.S. Langer. Instabilities and pattern formation in crystal growth, Reviews of Modern Physics, (52), No. 1, 1980, pgs 1-27.

[54] R.D. Doherty. Met. Sci. (16), 1982, pgs 1-8.

[55] J. Koke, M. Modigell. Flow behaviour of semi-solid metal alloys, Journal of Non-Newtonian Fluid Mechanics, (11), 2003, pgs 141-160.

[56] J.A. Yurko. Fluid Flow Behavior of Semi-solid aluminum at high Shear Rates, Ph.D. Thesis, Professor M.C. Flemings advisor, Massachusetts Institute of Technology, Cambridge, MA, June 2001.

[57] D.V. Ragone, C.M. Adams, H.F. Taylor. Some Factors Affecting Fluidity of Metals, AFS Transactions, (64), 1956, pgs 640-652.

[58] J.E. Niesse. Analysis of Fluidity of Metals, Ph.D. Thesis, Professor M.C. Flemings advisor, Massachusetts Institute of Technology, Cambridge, MA, Sept. 1958.

[59] M.C. Flemings, Fluidity of metals - techniques for producing ultra-thin section castings, The British Foundryman, July 1964.

[60] Y.D. Kwon, Z.H. Lee. The effect of grain refining and oxide inclusion on the fluidity of Al-4.5Cu-0.6Mn and A356 alloys, Materials Science and Engineering A, (A360), 2003, pgs 372-376.

[61] M.C. Flemings, E. Niiyama, H.F. Taylor, Fluidity of Aluminum Alloys: an experimental and quantitative evaluation, AFS Transactions, (69), 1961, pgs 625-635.

[62] B.C. Pai, H. Jones, Proc. Int. Conf. on Solidification Technique in the Foundry and Cast House, The Metals Society, London, UK, 1980.

[63] Y. Sumartha. Fluidity of Rheocast A356 Alloy, MS Thesis, Professor M.C. Flemings advisor, Massachusetts Institute of Technology, Cambridge, MA, Sept. 1997.

[64] Sh. Nafisi *et al.* Effects of Different Solids on the Fluidity of Rheocast 356 Al-Si Alloy, Symposium on Advanced Processes, TMS Annual Meeting, Charlotte, NC, March 14-18 2004.

[65] A. Karma, Physics Department, Northeastern University, Boston, MA, various meetings, August-December 2004.

[66] A. Karma, Physics Department, Northeastern University, Boston, MA, unpublished work, December 2004.

[67] A. Karma, Physics Department, Northeastern University, Boston, MA, March 15, 2004.

[68] T.Z. Kattamis. Experimental Observations on the Growth Stability of Spherical Crystals During Freezing, Journal of Crystal Growth, (18), 1973, pgs 45-53.

[69] D.R. Poirier, G.H. Geiger. Transport Phenomena in Materials Processing, TMS Publications, Warrendale, PA, 1994, pg 18.

[70] A.A. Greer. Grain Refinement of Aluminum Alloys, Proceedings of the Solidification of Aluminum Alloys Symposium, TMS Annual Meeting, Charlotte, NC, March 14-18 2004, pgs 131-145.

[71] M. Easton, D. StJohn. Factors Affecting the Development of a Fine Grained Solidification Microstructure in Aluminum Alloys, Proceedings of the Solidification of Aluminum Alloys Symposium, TMS Annual Meeting, Charlotte, NC, March 14-18 2004, pgs 147-156.

[72] W. Kurz, D.J. Fisher. Fundamentals of Solidification, third ed., Trans Tech Publications, Switzerland, Germany, UK, USA, 1989, pgs 69-80.

[73] L. Ratke, C. Beckerman. Concurrent Growth and Coarsening of Spheres, Acta Materialia, (49), 2001, pgs 4041-4045.

[74] A. Mortensen, On the Influence of Coarsening on Microsegregation, Metallurgical Transactions A, (20A), Feb. 1989, pgs 247-253.

[75] V.R. Voller, C. Beckermann, Approximate Models of Microsegregation with Coarsening, Metallurgical Transactions A, (30A), Nov. 1999, pgs 3016-3019.

[76] V.R. Voller, A semi-analytical model of microsegregation and coarsening in a binary alloy, Journal of Crystal Growth, (197), 1999, pgs 333-340.

Appendix A

Particle Growth Velocity

The following unpublished work gives the deriiation of an expression for the growth velocity of a solidifying spherical particle in an alloy subjected to a sudden increase in cooling rate.[66] After the sudden increase, the cooling rate is assumed constant. It is also assumed that the cooling rate is fast enough so that the thickness of the solutal diffusion boundary layer created by the particle acceleration is much smaller than the particle radius. Therefore, the interface can be treated locally as a planar interface.

The basic equations that we wish to solve are the one-dimensional diffusion equation for the solute

$$\frac{\partial C}{\partial t} = D_L \frac{\partial^2 C}{\partial r^2} \tag{A.1}$$

and

$$C_L^* - C_0 = \frac{\dot{T}t}{|m_L|} \tag{A.2}$$

subject to the boundary conditions at the interface ($r = R$)

$$C_0(1-k)V = -D_L \frac{\partial C}{\partial r} \tag{A.3}$$

as well as the condition far from the interface

$$C(\infty) = C_0 \tag{A.4}$$

First, the dimensionless concentration, u, is defined as:

$$u = \frac{C(r) - C_0}{C_0(1-k)} \tag{A.5}$$

Additionally, the time rate of change of dimensionless supersaturation, $\dot{\Omega}$, is defined:

$$\dot{\Omega} = \frac{\dot{T}}{|m_L| C_0(1-k)} \tag{A.6}$$

In terms of these new variables, Equations. A.1 through A.4 become, respectively

$$\frac{\partial u}{\partial t} = D_L \frac{\partial^2 u}{\partial r^2} \tag{A.7}$$

$$V = -D_L \frac{\partial u}{\partial r} \tag{A.8}$$

$$u(R) = \dot{\Omega} t \tag{A.9}$$

$$u(\infty) = 0 \tag{A.10}$$

A major simplification in solving this problem is that the particle radius turns out to change very little during the rapid increase of velocity of the particle. This is because the particle velocity increases will be shown to increase as the square root of time, and hence the particle radius increases initially slower as the 3/2 power of time. Therefore, it is reasonable to assume that the particle radius is constant during the initial rapid increase of the velocity ($R(t) = R$). After the time-dependent diffusion field around the stationary particle is calculated, the particle growth velocity can then be obtained from Equation A.8.

A self-similar solution of Equation A.7 of the form

$$u(r,t) = \dot{\Omega} t f\left(\frac{r-R}{(D_L t)^{1/2}}\right) \tag{A.11}$$

is sought to calculate the time-dependent diffusion field around the particle of radius R. Next, Equation A.11 is substituted into Equation A.7 and the variable y is defined as $y = \frac{r-R}{(D_L t)^{1/2}}$ which transforms Equation A.7 into the form

$$f - \frac{y}{2}\frac{df}{dy} = \frac{d^2 f}{dy^2} \tag{A.12}$$

Equation A.12 must be solved subject to the boundary conditions

$$f(0) = 1 \text{ and } f(\infty) = 0 \tag{A.13}$$

which follow directly from Equations A.9 and A.10 together with the definition of Equation A.11.

The particle velocity is now obtained from Equation A.8 which becomes

$$V = -D_L\left(\frac{\partial u}{\partial r}\right)_{r=R} = -\dot{\Omega}\,(D_L t)^{1/2}\left(\frac{df}{dy}\right)_{y=0} \tag{A.14}$$

Equation A.12 is a second order differential equation that has a unique solution subject to the boundary conditions in A.13. Solving this equation numerically yields

$$-\left(\frac{df}{dy}\right)_{y=0} = 1.12 \equiv A \tag{A.15}$$

The constant A is in reasonably good quantitative agreement with the one obtained from a empirical fit of the numerical solution of the full free-boundary problem ($A = 1.28$) where the particle radius is not assumed to be constant.

An approximate analytical expression for A can also be obtained by noting that for small y Equation A.12 simplifies to

$$f = \frac{d^2 f}{dy^2} \tag{A.16}$$

which has the trivial solution $f = \exp(-y)$. This solution yields the approximate prediction $A = 1$, which is about 10% smaller than the exact numerical value quoted above.

Appendix B

Alloy Properties

The following is list of relevant property data for the two alloys used in this study.

Al-4.5wt%Cu

Variable	Description	Units	Value
ρ	density	g / cm^3	2.8
η	liquid viscosity (pure liquid Al at Tp)	poise (g / cm s)	$1.2*10^{-2}$
m_L	liquidus slope	C / wt%	-3.4
m_S	solidus slope	C / wt%	-17.9
k	partition coefficient	-	0.19
C_0	bulk alloy solute content	wt%Cu	4.5
D_L	solute diffusivity in liquid	cm^2 / s	$3*10^{-5}$
Γ	Gibbs-Thompson coefficient	C cm	$2.4*10^{-5}$
T_L	liquidus temperature	C	645 (649 measured)
T_{eut}	eutectic temperature	C	550
T_p	melting point of pure Al	C	660
ΔH	heat of fusion (pure Al)	J / g	-398
σ	solid-liquid interfacial energy	J / cm^2	$5*10^{-6}$
K	thermal conductivity	J / s m C	211

A357

Variable	Description	Units	Value
ρ	density	g / cm^3	2.65
T_L	liquidus temperature	C	617
T_{eutec}	eutectic temperature	C	577

Appendix C

Experimental Data Tables

Flow Velocity Measurement/Flow Characterization : Al-4.5wt%Cu

Exper. #	T initial (C)	Superheat (C)	f_s initial	ΔP (torr)	Estimated Velocity (cm/s)	Reynolds number
1	654	5	0	400	286	1335

Defining Rheocast and Conventional-Cast Structures : Al-4.5wt%Cu

Exper. #	Mass (g)	T initial (C)	Stir time (s)	(dT/dt) initial (C/s)	Solidification time (min)	Microprobe
2	750	653	-	0.15	9	-
3	750	653	10	0.15	9	1 particle

Formation of Spheroidal Microstructure by Reheating of Equiaxed Dendrites: Al-4.5wt%Cu

Exper. #	Sample size (g)	Reheat time above eutectic temp. (s)	T max (C)
5	0.5	5	606
6	0.5	15	621
7	0.5	60	635
8	0.5	120	625
9	0.5	480	620

Formation of Spheroidal Microstructure by Reheating of Equiaxed Dendrites: Quantitative Metallography

Exper. #	R_d (μm)	Measurement Technique	Approx. # Grains Meas.	Error % = (StdDev/Avg)*100
5a	19.15	line intercept	380	16
6a	34.94	line intercept	380	19
7a	46.87	line intercept	340	16
8a	55.87	line intercept	270	16
9a	69.74	line intercept	170	19

Growth of Spheroidal Particles in Rheocast Alloy: Al-4.5wt%Cu

Exper. #	T initial (C)	Stir time (s)	Wait time (s)	T_quench (C)	f_s at quench	ΔP (torr)	Microprobe
10	653	5	0	648.5	0.05	200	-
11	653	20	0	647	0.18	200	2 particles
12	653	20	60	645	0.31	200	-
13	653	20	180	643	0.45	200	-

Growth of Spheroidal Particles in Rheocast Alloy: Quantitative Metallography

Exper. #	R_i (μm)	R_f (μm)	Measurement Technique	# Grains Meas.	Error % = (StdDev/Avg)*100
10a	18.95	30.09	direct meas. of select grains	Ri: 36 , Rf: 89	Ri: 44, Rf: 30
11a	33.74	41.57	direct meas. of select grains	Ri: 31 , Rf: 205	Ri: 27, Rf: 23
12a	49.13	59.63	direct meas. of select grains	Ri: 30 , Rf: 120	Ri: 30, Rf: 23
13a	73.08	81.08	direct meas. of select grains	Ri: 10 , Rf: 72	Ri: 34, Rf: 32

Particle Interface Stability : Al-4.5wt%Cu

Exper. #	Sample size (g)	T quench (C)	f_s at quench	(dT/dt) quench (C/s)
14	4.3	646	0.25	1.1
15	4.3	646	0.25	2.8
16	4.3	646	0.25	4.2
17	4.3	646	0.25	9.3
18	4.3	646	0.25	38
19	4.3	642	0.45	1.7
20	4.3	642	0.45	2.9
21	4.3	642	0.45	3.8
22	4.3	642	0.45	10.5
23	4.3	642	0.45	40
24	4.3	636	0.63	3.5
25	4.3	636	0.63	5.6
26	4.3	636	0.63	11
27	4.3	636	0.63	50

Fluidity of A357 Alloy

Exper. #	T initial (C)	Superheat (C)	f_s initial	ΔP (torr)	Effective Fluidity (cm)
28	638	22	0	200	4.00
29	638	22	0	200	3.51
30	622	5	0	200	3.38
31	622	5	0	200	3.53
32	610	-7	0.15	200	3.25
33	610	-7	0.15	200	2.75
34	595	-22	0.37	200	2.15
35	595	-22	0.37	200	2.13
36	595	-22	0.37	400	2.81
37	595	-22	0.37	400	4.13
38	595	-22	0.37	560	5.70
39	595	-22	0.37	560	5.15

Appendix D

Estimated Cooling Rate of Alloy Drawn in Quench Mold

In order to approximate the cooling rate of alloy drawn into the quench mold, $\left(\frac{dT}{dt}\right)_{qm}$, the solidification temperature range will be divided by an estimate of the solidification time, t_s. Using Figure 5-3(a), the secondary dendrite arm spacing (DAS) of grains in metal solidified in the mold is estimated to be between 4 and 5 μm. The DAS of 4.5 μm is inputted into the empirical equation used to produce the classical dendrite arm ripening curve:

$$DAS = 7.59 * (t_s)^{0.4} \tag{D.1}$$

and the corresponding solidification time, t_s, is found to be approximately 0.265 seconds. The solidification range is taken to be the difference between the Al-4.5wt%Cu liquidus temperature and the Al-Cu eutectic temperature:

$$(649 - 550)°C = 99°C \tag{D.2}$$

Dividing the solidification temperature range by estimated solidification time yields:

$$\left(\frac{dT}{dt}\right)_{qm} \backsim 375°C/s \tag{D.3}$$

Appendix E

Heat Transfer Coefficient: Rod-Melt Interface

In order to estimate the heat transfer coefficient for the stirring rod- melt interface, h_{rod}, it is assumed that the heat flow out of the melt, $\dot{Q}_{out}$, equals the heat going into the stirring rod, $\dot{Q}_{in}$. The rate of heat flow out of the melt during stirring for time Δt is approximated by the expression:

$$\dot{Q}_{out} \backsim \frac{(M)\, f_s \Delta H}{(\Delta t)} \tag{E.1}$$

where M is the mass of the melt, f_s is the solid fraction formed during stirring, and ΔH is the heat of fusion per unit mass of pure aluminum. The heat flow into the copper stirring rod is approximated by

$$\dot{Q}_{in} \backsim A h_{rod} (\Delta T_r) \tag{E.2}$$

where A is the total rod-melt contact area and ΔT_r is the temperature difference between the rod and the melt. Setting Equation E.1 and E.2 equal and solving for h_{rod} yields:

$$h_{rod} \backsim \frac{(M)\, f_s \Delta H}{A \Delta T_r\, (\Delta t)} \tag{E.3}$$

In Appendix C, Experiment#11, a melt of 750 *grams* was stirred for 20 seconds and approximately 0.2 solid fraction formed. The heat of fusion of pure aluminum is given in Appendix

B. Using the geometry of the rod and estimated immersion length shown in Figure 4-2(a), the contact area between the rod and the melt was estimated to be 40 cm^2. The average temperature difference between the rod and melt over the 20 seconds of stirring is taken to be $300°C$ (roughly half to the initial temperature difference between the melt and the rod). Inputting this data in Equation E.3 gives:

$$h_{rod} \backsim 2488 \frac{J}{s\ m^2\ °C} \tag{E.4}$$

Appendix F

Biot Number For Interface Stability Samples

The dimensionless Biot number is an index of the uniformity of a material being heated or cooled. It is defined as

$$Bi = \frac{hL}{K} \tag{F.1}$$

where h is the heat transfer coefficient, L is a characteristic length for the heat flow, and K is the thermal conductivity of the material being heated or cooled. When the Biot number is estimated to be less than 0.1, it is reasonable to assume that the body being heated or cooled is isothermal at all times. In the interface stability experiments, it was essential that the samples were cooled uniformly at the measured rate. The size of the Al-4.5wt%Cu samples used in the interface stability experiments was selected such that the Biot number for the samples was less than 0.1. The samples were chosen to be cylindrical, roughly 10 mm in diameter, and 15 mm in height. The characteristic length for heat flow is the cylinder radius, 5 mm. To show that the Biot number during the experiments was always less than 0.1, the Biot number was calculated using the heat transfer coefficient, h, for metal quenched in water. This was the largest heat transfer coefficient for any sample in the series of experiments, estimated to be about $2500 \frac{J}{s\ m^2\ ^\circ C}$.[69] Using this value for h, the characteristic length of 5 mm, and the average of the thermal conductivity of solid and liquid aluminum at the melting point (Appendix B),

the maximum Biot number in the experiments is shown to be less than 0.1:

$$Bi_{\max} = \frac{2500 * 0.005}{151} = 0.083 \tag{F.2}$$